Modelling dust growth in acetylene plasmas under low pressure conditions

Senders, Mischa J.

Award date:
2022

– Modelling dust growth in acetylene plasmas under low pressure conditions –

Eindhoven, November 7, 2022

M.J. Senders 0945467

Program:	Applied physics
Group:	EPG
ECTS:	45
Date of defence:	November 18, 2022
Track:	Plasmas and beams

Supervisors:
dr.ir. J. Beckers
ir. T.J.M. Donders

Commitee members:
dr.ir. J. Beckers
prof.dr. F. Toschi
dr.ir. J. van Dijk
ir. T.J.M. Donders

Abstract

Dusty plasmas contain solid particles from several nanometers to several micrometers in diameter. These plasmas are found in large-scale astrophysical objects, as well as in the semiconductor industry and material processing. Dust particles tend to form spontaneously in low-pressure radiofrequency acetylene (C_2H_2) plasmas. In this thesis, a global model was built using PLASIMO in order to simulate the first two phases (nucleation and coagulation) of dust growth in acetylene. Nucleation was simulated using polymerisation reactions up to species containing 12 carbon atoms. Coagulation was simulated using a hard-sphere coagulation frequency in the general dynamic equation for aerosols. Charging of nanoparticles was taken into account using OML-theory. The results of the simulation of the nucleation phase were found to be in good agreement with literature. It was shown that coagulation can be simulated in PLASIMO by discretising the volume space using exact sections, which increase linearly in size. Furthermore, we have seen that the charging of nanoparticles and the repulsive force between negatively charged nanoparticles can already have a significant effect on the speed of dust growth for species with a radius up to 1.4 nm. Since the current model was not able to simulate coagulation up to nanoparticles with several tens of nanometers in radius due to high computational costs, improvements to the model are proposed to make this possible in future studies. Finally, a simple one-dimensional model of the nucleation phase was built and compared to the results of the global model. It has been shown that the global model can be an accurate model for dust growth, but spatial dependencies have to be taken into account to describe charged particles more accurately.

Contents

1 Introduction

Up to about 150 years ago, scientists thought there were only three states of matter: solids, liquids and gasses. This however, is just as wrong as assuming that that there is only one chemical element, since both assumptions miss out on 99% of what is really out there in the visible universe. In reality, way over 99% of all matter in the visible universe is in the plasma state, often called the fourth state of matter [1] [2]. The overwhelming amount of matter being in the plasma state is easily understood from the realisation that all stars and the majority of interstellar matter are plasma [3]. It is therefore remarkable that the first laboratory plasma was only identified by Sir William Crookes in 1879 [4]. It took almost 50 years longer until systematic studies on plasmas were performed by Irving Langmuir in 1928 [5]. We are lucky to live in a time in which humanity is familiar with plasma physics, since it is a fascinating branch of physics which leads to stunning natural phenomena such as the northern light [6] and metamorphic technological opportunities such as the production of transistors [7].

A plasma is an ionised gas, which means that charged particles, electrons and ions, are present inside the gas. The presence of charged particles allows for very interesting physical phenomena which are not frequently encountered under non-plasma conditions. The Sun [8], lightning [9] and the rings of Saturn [1] are examples of famous forms of plasma in nature, but we have also learned to use plasma in medical treatment [10] and material processing [7]. The fact that a plasma contains free charge carriers means that we can influence or even control it by applying electric and magnetic fields. Furthermore, it is quite common for plasma to not be in thermal equilibrium, making it possible for the electrons to have a temperature of the order 10^4K, whilst the gas species are at or around room temperature. This is useful since the hot electrons can trigger complex and highly energetic chemistry, with low risks of burning down the wall material of an experimental reaction vessel for example, since the heavy species that are the most potent to do damage are less energetic. Plasma enhanced chemical vapour deposition (PECVD) is a common application in the semiconductor industry that combines both the electromagnetic control and temperature difference between electrons and heavy particles to form nanometer-sized layers on a substrate [11].

Sometimes particles with a size of a few nanometers up to a few micrometers are suspended in the plasma. We call these dusty plasmas. This size range covers everything from the diameter of a hemoglobine molecule ($\approx$5 nm) [12] to that of a typical bacterium ($\approx 5\,\mu$m) [13]. It should be noted that the dust particles we encounter in our plasma are significantly smaller than the typical dust you would find in your house, such as skin cells and pollen, which are both typically in the order of tens of micrometres and therefore at least an order magnitude larger than plasma dust [14]. The definition of dust for the purposes of this thesis will be refined further in section 2.6. It has been observed that dust can spontaneously grow under certain plasma conditions [1]. Such dust particles are also encountered in various fields in industry such as the semiconductor industry, where they tend to deteriorate manufacturing processes [15]. Dust particles can, for example, lead to a yield loss of 100% if they land on the reticle of extreme ultra-violet (EUV) lithography systems [16] [17].

Dust grows in reactive gasses that contain contaminations which can polymerise, including silicon containing gasses like silane (SiH_4) [18], and hydrocarbons like methane (CH_4) [19] and acetylene (C_2H_2) [20]. Generally, the process of dust growth in plasma can be broken down into three distinct phases: nucleation, coagulation and accretion. A lot of research has been done on the initial stage of dust growth called the nucleation phase, in which nanoparticles of several nanometers in diameter are formed from a precursor material due to polymerisation [20] [21] [22]. This phase is dominated by the plasma chemistry. Once the local density of particles of a few nanometers in diameter is sufficiently high, the second stage of dust growth called coagulation starts [23]. In this phase, the charged nanoparticles rapidly grow by means of clustering. As the nanoparticles get larger, they charge more and more negatively. This happens due to the higher mobility of the electrons which are negatively charged, compared to the mobility of positively charged ions. Once the nanoparticles are sufficiently large, they will have a permanent negative charge. Consequently, clustering will no longer occur due to the repelling Coulomb force between dust particles and further growth happens only at the surface by binding positive ions and radicals. This last growth stage in which surface growth takes place is called accretion. In this phase, dust particles grow towards the micrometer size range. At this size range, dust particles are typically pulled out of the discharge by the increasing ion drag force [24].

We have discussed that the formation of dust in plasmas can have significant hazards for industrial applications. It is therefore interesting to purposefully create a plasma environment, in which a lot of dust will be grown. This

allows us to study the fundamental growth behaviour in order to eventually avoid or minimise industrial hazards in the future. De Bleecker et al. made a self consistent dust-particle growth model which describes both the nucleation and coagulation stages in silane [25]. We have also seen that hydrocarbons are a common form of contamination, which is why the aim of this thesis is to make a growth model describing growth in a hydrocarbon: acetylene (C_2H_2). Numerical simulations are used, with the ultimate goal to compare the outcomes to experimental data. The challenge in constructing a full growth model starting with the precursor all the way up to the micrometer range lies in the various different physical processes leading to growth, which are dependent on the size of the particle. For example, the transition from the chemical polymerisation phase towards the solid dust phase and the charging of dust particles are not yet fully understood, since it is challenging to do experiments on the corresponding nanometer and nanosecond length-scale and timescale simultaneously [1]. In this thesis, simulations are performed on nucleation, coagulation and charging separately as well as jointly to study the influence of the various mechanisms and stages of growth. Future possibilities for model extensions are presented which can be used to also take the accretion phase into account.

The numerical plasma simulations software package PLASIMO will be used for the numerical simulations of the plasma chemistry and coagulation. PLASIMO is designed in order to optimise the simulation of complex types of chemistry containing many different reactions and species as well as interactions with the boundaries. Some processes such as accretion cannot be fully modelled in PLASIMO yet, hence extensions to the model will be proposed to make this possible in the future. In this thesis we will answer the following research question:

Is it possible to simulate the nucleation and coagulation phases of dust growth in low-pressure acetylene plasmas in PLASIMO?

The outline of this thesis is as follows:

Section 2 explains the physical concepts and processes used in the model. It starts with the fundamental equations and principles of plasma physics and builds towards more complex processes such as particle charging and the force balance on nanoparticles.

Section 3 discusses the plasma chemistry in acetylene (C_2H_2), which is the precursor for dust growth in our model. The most important species and polymerisation reactions will be presented using existing acetylene models from literature.

Section 4 describes numerical techniques that will be used to run the model. It will also go into numerical challenges and how they have been tackled as well as some of the approximations that were required to do the analysis.

Section 5 presents and discusses the results of the numerical simulations of the space-averaged model.

Section 6 presents and discusses the results of numerical simulations of the one-dimensional model.

Finally, in section 7, a conclusion will be drawn based on the simulations of sections 5 and 6 and ideas for extensions to the model will be presented.

2 Theory

One of the reasons why plasmas physics is so interesting is that many fields of physics come together. We are dealing with charged particles so we need Maxwell's theory of electromagnetism. The vast amount of particles requires modellers to use distribution functions from statistical physics using the laws of thermodynamics. Quantum descriptions are useful for several atomic and molecular transitions, while classical mechanics and Newton's equations are applicable to the larger dust particles. In this section we will review the most important concepts and refer the reader to other sources containing more detailed descriptions. The key equations and principles of the above mentioned topics required to understand dust growth in plasmas will be revised explicitly. First we briefly review the fundamental equations for plasma physics including Maxwell's equations, the Boltzmann equation, as well as plasma properties such as the Debye length and the concept of plasma sheaths. A sidestep will be made explaining the types particles present in a plasma environment as well as the chemical interactions they can undergo which will be used to describe the transport of these particles within a plasma. Finally, the above mentioned tools will help us to understand the three stages of dust growth: nucleation, coagulation and accretion which will be explained succeeded by the transport of these dust particles.

2.1 Fundamental equations for plasma physics

In essence, a plasma is a cloud of ionised gas, which can contain a vast amount of different species. The presence of charges implies that we need Maxwell's description of electromagnetism (section 2.1.1), whilst the presence of a large number of particles means that we need statistical physics, the Boltzmann equation in particular (section 2.1.2).

2.1.1 Electromagnetism

Maxwell's equations are the four fundamental equations which cover, in principle, electromagnetism fully. Since the influence of magnetic fields is typically neglected in the plasma relevant for this thesis, we will focus our attention on Maxwell's equations involving only the electric field:

$$\boldsymbol{\nabla} \cdot \vec{\mathbf{E}} = \frac{\rho}{\epsilon_0} \tag{2.1}$$

and

$$\boldsymbol{\nabla} \times \vec{\mathbf{E}} = 0, \tag{2.2}$$

with $\vec{\mathbf{E}}$ the electric field, ρ the charge density and ϵ_0 the permittivity of free space [26]. Since the electric field is irrotational (the curl vanishes in equation (2.2)), it follows from the Helmholtz decomposition theorem that it can without loss of generality be written as the gradient of a potential:

$$\boldsymbol{\nabla} \cdot \vec{\mathbf{E}} = \boldsymbol{\nabla} \cdot (-\boldsymbol{\nabla}\phi) = -\nabla^2\phi = \frac{\rho}{\epsilon_0}, \tag{2.3}$$

which is the well-known Poisson equation. Furthermore, the charge density $\rho = \sum n_s q_s$ has a positive ion, negative ion and electron contribution, since these are the charged species present[1]. In plasma physics, it is very common to talk about the potential rather than the electric field. We will come back to the Poisson equation in discussing various topics such as quasi-neutrality and sheaths 2.2.2.

[1] As we will see later, dust particles can also carry charge but these charged particles can be categorised as ions.

2.1.2 Boltzmann's equation

The second key equation to describe plasma physics is the Boltzmann equation. Before diving into the Boltzmann equation itself, lets briefly try to understand why a statistical description is required. In this thesis, we will model a plasma in a cylinder with a radius and length of 3 cm, a temperature of 400 K and a low pressure of 40 Pa. Using the ideal gas law $p = nk_BT$, we find that the number of particles present in this plasma is in the order of 10^{17}. In a kinetic model, it is required to store the three position and velocity components for every particle. Storing this data would require thousands of the most powerful commercial hard drives at the moment of writing. Kinetic methods are therefore clearly unfeasible, without even taking into account the computation time. Clearly, we need a more efficient approach using the tools from statistics to describe these particles. A common approach is to define a distribution function $f(\vec{\mathbf{r}}, \vec{\mathbf{v}}, t)$ such that $N = \int f(\vec{\mathbf{r}}, \vec{\mathbf{v}}, t) d^3r d^3v$ the total number of particles [27]. The Boltzmann equation is then given by:

$$\frac{\partial f}{\partial t} + \vec{\mathbf{v}} \cdot \boldsymbol{\nabla}_r f + \frac{\vec{\mathbf{F}}}{m} \cdot \boldsymbol{\nabla}_v f = \left.\frac{\partial f}{\partial t}\right|_c , \tag{2.4}$$

with $\vec{\mathbf{v}}$ the particle velocity, $\boldsymbol{\nabla}_r$ the spatial gradient operator, $\vec{\mathbf{F}}$ the force vector, m the mass, $\boldsymbol{\nabla}_v$ the velocity gradient operator and the right hand side the gain or loss due to collisions. Equation 2.4 states that the change of the number of particles at a certain point in space with a certain velocity (first term), plus particles moving to and away from this space (second term), plus particles accelerating to and away from this velocity (third term) is equal to particles appearing or disappearing due to collisions (final term). The zeroth, first and second moments of the Boltzmann equation lead to particle conservation, flux conservation and energy conservation respectively. The zeroth moment is calculated by integrating the Boltzmann equation over velocity space. The first term of the integration gives $\frac{dn}{dt}$, the integration over the second term gives $\boldsymbol{\nabla}_r \cdot (n\vec{\mathbf{v}})$, whilst the integration over the force term vanishes since no particles have $v = \pm\infty$ m/s. The equation that follows is called the continuity equation and is given below:

$$\frac{\partial n}{\partial t} + \boldsymbol{\nabla} \cdot \vec{\boldsymbol{\Gamma}} = S, \tag{2.5}$$

with n the particle density, $\vec{\boldsymbol{\Gamma}} = n\vec{\mathbf{v}}$ the particle flux density and S the net source which contains the gains and losses due to chemical reactions. We will come back to the continuity equation in section 2.3.2.

2.2 Fundamental properties of plasmas

The fundamental plasma equations can be used to derive a number of key properties which are helpful for understanding and describing typical plasma conditions. In this section we will review why plasmas are quasi-neutral for length scales larger than the Debye length (section 2.2.1), why sheaths form at the boundaries, what the implications are and finally what this means for the potential of the plasma bulk (section 2.2.2).

2.2.1 Debye length and quasi-neutrality

As mentioned in section 2.1, the presence of a large number of charged particles is what sets plasmas apart from regular gasses. In a regular gas, the interactions between gas molecules are short-range, which means that any gas molecule can only influence its nearest neighbours [28]. The charged particles in a plasma interact according to Coulomb's law, which is a long-range force. This leads to interesting collective behaviour, because a single particle can influence a very large amount of other particles. To understand this collective behaviour, imagine that a relatively large net positive charge suddenly arises somewhere within the plasma bulk. This net positive charge attracts all negative charges in the vicinity, and not just the nearest neighbours, whilst it repulses all positive charges in the neighbourhood. As a consequence, all the nearby negative charges will move slightly closer to this net charge while the positive charges will move slightly away from this positive charge such that the net charge will be cancelled

out [2]. The distance at which net charges can effectively be shielded is called the electron Debye length and given by:

$$\lambda_{D,e} = \sqrt{\frac{\epsilon_0 k_B T_e}{e^2 n_e}} = \sqrt{\frac{\epsilon_0 \hat{T}_e}{e n_e}}, \tag{2.6}$$

with k_B the Boltzmann constant, T_e and $\hat{T}_e$ the electron temperature in Kelvin and electronvolt, e the elementary charge and n_e the electron density. The Debye length increases with increasing electron temperature, because highly energetic electrons are not influenced as much by net charges as cold electrons. In other words, it is a lot harder to change direction at high speed compared to lower speeds and this change in direction is required for shielding. Furthermore, the Debye length decreases with an increasing electron density. This is easy to understand: many electrons can shield a charge more effectively than just a few. The fact that charge fluctuations will be mitigated for volumes with dimensions larger than the Debye length leads to the concept of quasi-neutrality. The plasma contains many charged particles but is neutral as a whole. In fact, it is neutral for any region in the bulk of the plasma with dimensions larger than the Debye length.

2.2.2 The plasma potential and sheaths

The Debye length and the concept of quasi-neutrality are properties in the bulk of the plasma. In this section we will see what happens near the plasma walls. To understand what happens near the walls, we need the difference in the thermal velocities of electrons and positive ions:

$$v_{e,i} = \sqrt{\frac{8 k_B T_{e,i}}{m_{e,i} \pi}}, \tag{2.7}$$

with v_e and v_i respectively the average electron and ion speeds, T_e and T_i the electron and ion temperatures and m_e and m_i the electron and ionic species mass. In the next section, we will see that $T_e \geq T_i$ for low-pressure RF plasmas and $m_e \ll m_i$. It is therefore easy to see that $v_e \gg v_i$, which means that electrons will leave the discharge at a much higher rate yielding a positive potential in the plasma bulk relative to the plasma edge. This process cannot be sustained since it would charge the wall indefinitely. Instead, an ambipolar electric field is created due to the charging of the wall, which counteracts electrons leaving the discharge and stimulates the outflow of ions until these two processes cancel out and steady-state is reached [3].

The potential and electric field are plotted schematically in figure 2.1 and related according to equation (2.3). It can be seen in figure 2.1a that the bulk of the plasma has a positive potential ϕ_{bulk} with respect to the plasma walls. In 1D, the walls consist of a grounded plate at zero potential and a plate at the applied RF potential, which is zero on average. Figure 2.1b shows the electric field in the plasma region and at the walls. It also shows that the electric field in the bulk is close to zero, since shielding will try to cancel any electric fields that form. The electric field at the edges points away from the plasma such that positive ions are pushed outwards and electrons and negative ions are pulled inwards. There are multiple types of approximations for the sheath potential. Using conversation of ion energy and continuity of ion flux, the Bohm velocity can be derived. The Bohm velocity is the velocity of ions near the sheaths [3]:

$$u_B = \sqrt{\frac{k_B T_e}{m_i}}. \tag{2.8}$$

The notion that the plasma cannot charge indefinitely means that the charge density should become a constant [26]:

[2] In practice electrons are far more effective at shielding than ions because electrons are more than a thousand times lighter and therefore far more mobile than ions.

Figure 2.1: Schematical representation of the potential and electric field at the edges and in the bulk of a plasma with $x_{s,l}$ the left sheath position and $x_{s,r}$ the right sheath position.

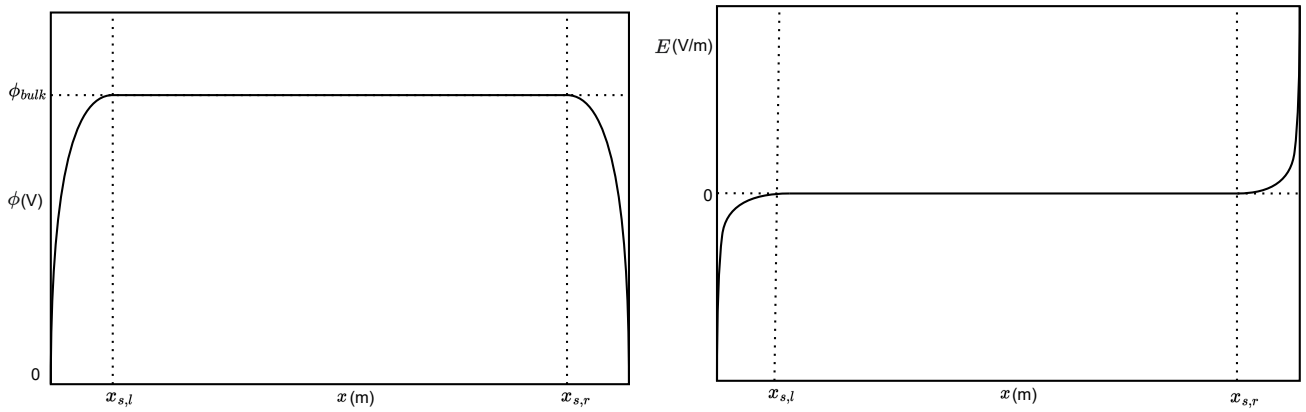

(a) Potential in the sheaths and plasma region. It can be seen that the bulk of the plasma has a positive potential with respect to the plasma edges of ϕ_{bulk}.

(b) Electric field in the sheath and plasma region. It can be seen that the electric field in the bulk is approximately zero due to shielding effects, while the electric field at the edges is directed such that positive charges are pushed outwards and electric charges are pulled inwards.

$$\frac{d\rho}{dt} = 0 = -\boldsymbol{\nabla} \cdot \vec{\mathbf{J}}, \tag{2.9}$$

with $\vec{\mathbf{J}}$ the current density. Equation (2.9) is only valid over many RF cycles. In a 1D parallel plate reactor, this leads to: $\frac{dJ_x}{dx} = 0$, so J_x is a constant. There are no direct currents over many cycles of an RF plasma, which means that the flux density of negative species should eventually be equal to the flux density of positive species:

$$\vec{\mathbf{\Gamma}}_e + \vec{\mathbf{\Gamma}}_{i-} = \vec{\mathbf{\Gamma}}_{i+}, \tag{2.10}$$

with $\vec{\mathbf{\Gamma}}_e$, $\vec{\mathbf{\Gamma}}_{i-}$, and $\vec{\mathbf{\Gamma}}_{i+}$ the electron, negative ion and positive ion flux density to the wall.

2.3 Applications of the Boltzmann equation

The Boltzmann equation was briefly introduced in section 2.1.2. In this section this equation will be studied in a little bit more detail, since it is a crucial ingredient for plasma modelling. In section 2.3.1 various solutions of the Boltzmann equation are presented and in section 2.3.2 it will be demonstrated how Boltzmann equation can be implemented to describe the evolution of certain species in space.

2.3.1 Solving the Boltzmann equation

Solving the Boltzmann equation is generally very cumbersome. In thermal equilibrium it is possible to assume a Maxwellian distribution. It assumes that the particles collide very frequently so that the energy is efficiently exchanged among the species which can be assumed for electrons in pressure plasmas where the pressure is sufficiently high. The Maxwellian distribution is given by:

$$f(v) = \left(\frac{m_s}{2k_B T_s}\right)^{3/2} \exp\left(-\frac{m_s v_s^2}{2k_B T_s}\right), \tag{2.11}$$

with m_s the particle mass, T_s the particle temperature and v_s the speed of species s and it describes how the particles of a certain species are distributed over the energy or velocity space. A Maxwellian distribution has an average velocity given by $\bar{v}_s = \sqrt{\frac{8k_B T_s}{m_s \pi}}$, the thermal velocity. Even though a Maxwellian distribution cannot be assumed for many low-pressure plasmas, it is still useful to keep the shape of the distribution in mind to describe general trends. The shape of the Maxwellian distribution function is given in figure 2.2, where the red curve describes a hotter gas than the red curve, since the distribution is shifted to higher velocities and analogously higher energies.

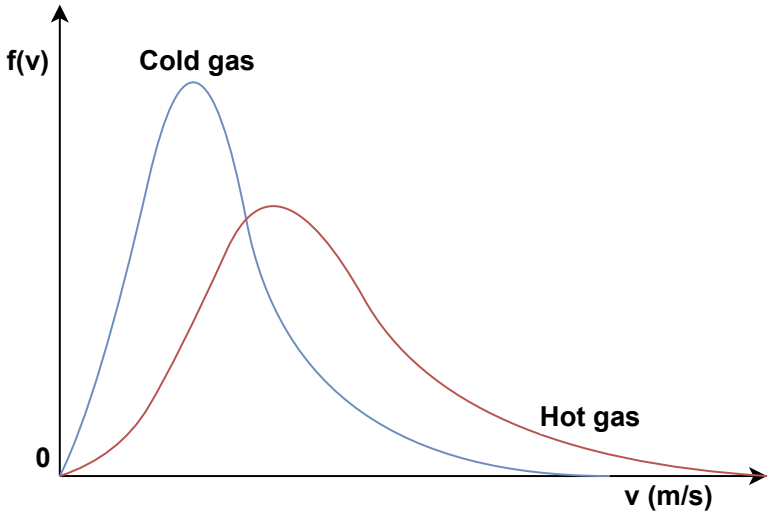

Figure 2.2: Two Maxwellian velocity distributions for a cold gas (blue) and a hot gas (red).

It is in general very hard to solve the Boltzmann equation analytically. This is why Hagelaar et al. implemented a method of solving the Boltzmann equation called BOLSIG+ [29], which uses a two-term approximation meaning that f is expanded using the first two Legendre-polynomials [30]. This approximation will be used in this thesis for electrons, since they cannot accurately be described by a Maxwellian distribution [20]. The gas species are assumed to be at a fixed uniform temperature which is common in literature [31] [32] [33], since a non-uniform gas temperature is very hard to model. More details on modelling the gas temperature can be found in [34] and [35].

2.3.2 Continuity equation

The continuity equation was already derived in section 2.1.2 by integrating the Boltzmann equation over the velocity space. It states that the change in particle density is either due to a net flux or chemical sources and sinks, which are chemical reactions. The flux density term describes the net motion within the plasma, which can be caused by a combination of various forces such as: Coulomb forces, friction forces, gravitational forces, magnetic forces and thermophoretic forces. The flux density of particles in a plasma is often calculated from just the electric force and a density gradient, whilst ignoring the other forces. This approximation is called the drift-diffusion equation [3]:

$$\vec{\mathbf{\Gamma}}_s = \mu_s \vec{\mathbf{E}} n_s - D_s \boldsymbol{\nabla} n_s, \tag{2.12}$$

with μ_s the particle mobility coefficient and D_s the particle diffusion coefficient. The first term describes how particles are affected by the net electric field called drift and the second term describes net motion due to gradients in density called which is called diffusion. Near thermal equilibrium, the diffusion coefficient and mobility coefficient are related by the Einstein equation [3] ([36] page 139):

$$D_s = \mu_s \frac{k_B T_s}{q_s} \tag{2.13}$$

All the other forces are neglected. It should be stressed that this equation applies only to the gaseous species atoms and molecules and not to dust particles. The force balance for dust particles will be derived in section 7.2.2.

2.4 Particles, collisions and interactions

So far, we have discussed the fundamental equations required for plasma physics. Maxwell's equations are defined by the presence of charged particles, whilst the Boltzmann equation is required to describe the incredibly large number of particles present within the plasma itself. Consequently, we derived the continuity equation for each type of species, stating that the change of the number density plus the flow towards and away from this point is equal to the net local production. Depending on the precursor material, plasmas can contain many different types of species which can all interact in different ways. There are neutral particles: atoms and molecules, as well as charged particles: electrons and ions. Radicals are species with an unpaired electron in their valence band causing them to be highly reactive. When two particles collide they can interact in different ways depending on their type and respective energies. The different types of species within the plasma can take part in various types of interactions: neutral-neutral, electron-neutral, ion-neutral and ion-ion. In order to understand these different interactions it is required to have a good understanding of the structure of molecules, which is why this will be discussed first. After that, the different interactions given above will be explained.

2.4.1 Molecules

Molecules consist of multiple atoms sticking together due to covalent chemical bonds. The atoms in covalent bonds share an electron pair amongst them. The number of covalent bonds an atom can form is typically equal to the difference between the total possible number of electrons in the outer valence shell and the actual number of electrons present. Hydrogen $\left(1s^1\right)$ has room for one more electron in the first shell and can therefore form one covalent bond, whilst carbon $\left(1s^2 2s^2 2p^2\right)$ can form four bonds thanks to the fact that carbon has room for four more electrons in the second shell.

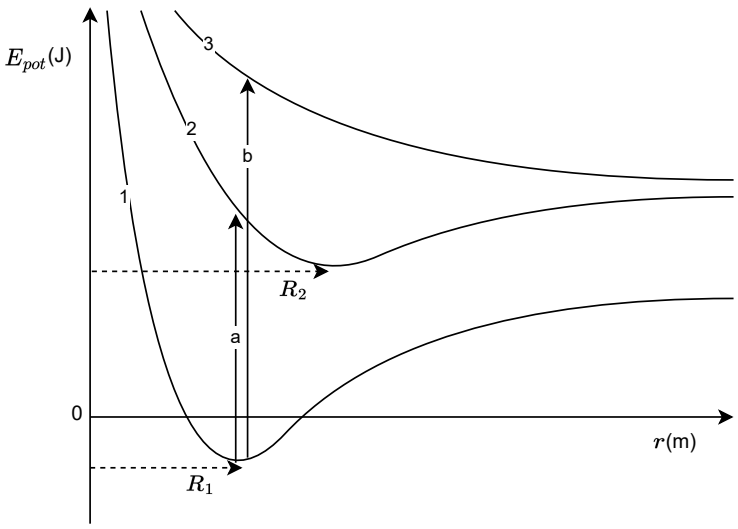

Figure 2.3: Inter-atomic potential as a function of radial distance between atoms for diatomic molecule. Figure based on: [3] (page 236).

The bonding behaviour of two atoms in space can be described using a potential energy diagram, an example for a diatomic molecule is shown in figure 2.3. For symmetry reasons, the potential energy of a diatomic molecule only depends on the distance between the atoms. A minimum in the potential energy diagram corresponds to a stable state, implying that the atoms want to stick together at a specific distance and a molecule is formed. This can be understood from the fact that it costs energy to either bring the atoms closer to each other or to pull them apart. Such minima exist for curve 1 and curve 2 in figure 2.3. The state described by curve 3 does not have a stable state which means that a molecule in this state will spontaneously dissociate. Energy is lost by increasing the distance which will therefore occur spontaneously. All three curves show the same behaviour in the extremes $(r \to 0)$ and $(r \to \infty)$. When the inter-atomic distance tends to zero, the potential energy goes to infinity. This is a direct consequence of the Pauli-exclusion principle: two particles cannot occupy the same state, in this case space, at the same time. When the inter-atomic distance tends to infinity, the potential energy becomes a constant which means that the force vanishes. This makes intuitive sense because an atom in Eindhoven will have no impact on an atom in Mexico City, regardless of their relative changes in position. It becomes nonsensical to speak of a molecule at all. The potential energy for very large inter-atomic distances is therefore simply the sum of the energies of the fragments.

The figure also helps us understand the different types of energies involved in chemical reactions and electronic transitions. Suppose there is a diatomic molecule in the ground state located at the minimum of curve 1. We can bring this molecule to the first excited state by increasing its energy with the associated transition energy indicated by arrow a. We call this energy the threshold energy for this excitation reaction. The diatomic molecule will subsequently increase the inter-atomic distance to find a new stable state, the minimum of curve 2, releasing the excess energy in the process. The energy difference between stable states 1 and 2 is therefore in general not equal to the threshold energy but slightly lower. To fully dissociate the molecule we have to provide the energy associated with transition b. After this transition, the molecule ends up on curve 3, for which no stable state exists. It is energetically favourable for the molecule to increase the inter-atomic distance until the atoms are so far apart that it dissociates completely. Once again the energy required to dissociate the molecule, the threshold energy, is unequal to the energy difference between the molecule and its corresponding fragments after the dissociation reaction. The required energy can be gained due to collisions. Every element has a favourable minimum energy composition, which is the composition in which the atom is most likely to exist in nature (eg H_2 for hydrogen). This will be used as a reference molecule with relative energy zero. The formation enthalpy is the net energy required to form a molecule from the basic constituents and can be used to calculate the change in energy and temperature of the system as a consequence of chemical reactions.

2.4.2 Collisions

When two particles collide, chemical reactions can take place. The rate at which these reactions happen depends on the densities of the reactants and the reaction cross section, which is a measure of the reaction probability. The distance at which the particle and the projectile barely touch each other is the radius of the cross section also called the critical impact parameter b_c. The impact parameter is defined as the perpendicular distance between the path of the projectile and the path of the centre of mass of the approaching particle. The cross section is therefore a disk around the particle such that any particles for which their travelling direction is orthogonal to this disk will cause a collision. This concept is illustrated in figure 2.4. In the case of billiards, the cross section of a ball is simply the disk with a radius equal to the physical radius of the ball. When the path of another billiard ball crosses this disk the particles collide. This however is not generally true for collisions involving charged or nano-scopic particles, since they might exert attractive or repulsive forces. If the force is attractive, the collision disk is larger than the physical radius of the particle, as shown in figure 2.4 and vice versa if the force is repulsive. If the collision particle is larger than the critical parameter $b > b_c$ the particles will not collide (P1 and P4), if $b = b_c$ the particles will just collide (P2 and P4), whilst the particles will collide head on for $b < b_c$. The trajectories of the particles are given schematically in blue and the collision disk of particle 4 is illustrated in green.

We can distinguish interactions between two neutral species, electrons and neutral particles, ions and neutral particles and finally interactions between two charged species, since collisions between these particle types are the most common and important in low ionised plasma conditions. A brief explanation of mentioned interactions will be be

discussed in the following sections.

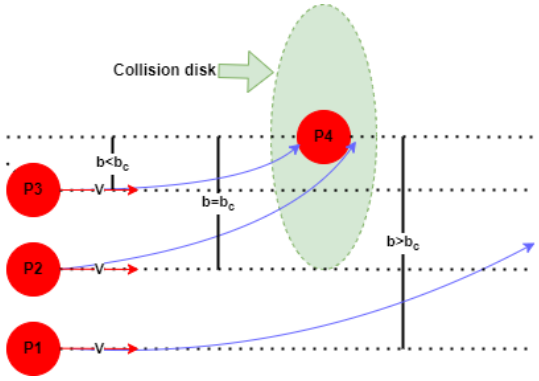

Figure 2.4: Collision parameters for three particles (P1, P2 and P3) approaching a fourth particle (P4) from infinity with velocity v in the reference frame of P4.

Neutral-neutral collisions

An acetylene plasma consists for more than 99% of neutral species, making neutral-neutral collisions the most common in the discharge. This comes with the requirement to describe these collisions accurately. A common empirical model for neutral-neutral reactions is by using the Lennard-Jones model which takes the following form [37]:

$$V = 4\epsilon \left(\left(\frac{\sigma}{r} \right)^{12} - \left(\frac{\sigma}{r} \right)^{6} \right), \tag{2.14}$$

with r the distance between the molecules, ϵ the depth of the well and σ the distance at which the potential is zero. The minimum potential energy occurs at $r_{min} = 2^{1/6}\sigma$. The Lennard-Jones potential describes the general behaviour of a system of two neutral particles. Neutral particles repel at very small distances due to the Pauli-exclusion principle, they attract at medium distances and the interaction vanishes at large distances. This last fact can be seen in figure 2.5, which shows the shape of the Lennard-Jones potential, using $\vec{\mathbf{F}} = -\frac{dE_{pot}}{dr}\hat{\vec{\mathbf{r}}}$.

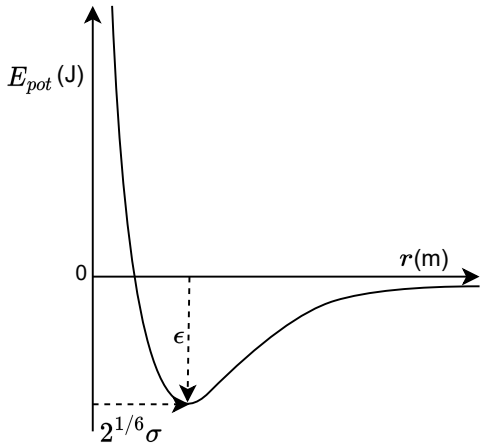

Figure 2.5: Potential energy of the Lennard-Jones model as a function of the intermolecular distance.

Electron-neutral collisions

Collisions between electrons and neutral particles are particularly important because these collisions are either elastic or inelastic and they can therefore determine the electron temperature [29], which as we have seen before, is a critical plasma parameter. Using classical momentum and energy balance, it can be shown that light particles do not transfer energy efficiently to heavy particles [3]. Since atoms and molecules are typically about four orders of magnitude heavier than electrons, the neutral gas species hardly gain any energy from collision with electrons. This is the reason why at low pressure conditions such as in this thesis, the electron temperature is far higher than the neutral particle temperature which is generally approximated to be constant around room temperature.

Despite the fact that electrons cannot efficiently transfer heat towards neutral species, electron-neutral collisions are key drivers of the plasma chemistry, since electrons can deliver the required energy for excitation and ionisation reactions. Charged species play an important role in the polymerisation. Ionisation is therefore a key process, which happens due to electron impact reactions. The reaction rate coefficient for particle impact reactions is found by the following integration [3]:

$$K = \int_{E_t}^{\infty} \sigma\left(E\right) f\left(E\right) v(E) dE, \tag{2.15}$$

with K the reaction rate coefficient, σ the cross section, E_t the threshold energy and $f(E)$ the electron energy distribution function (EEDF), which is calculated by BOLSIG+ for electrons and constant for gas species. The threshold energy is generally a factor of two to ten times higher than the average electron energy so that only the highly energetic electrons in the tail of the distribution can cause ionisation. Excitation can already be performed by less energetic electrons but it will not be taken into account in this thesis.

Ion-neutral collisions

Collisions between ions and neutral particles are described by the generalised Lennard-Jones [38] or Langevin model [39]. These reactions are different from neutral-neutral reactions since the ions can polarise the neutral species leading to stronger ion-dipole interactions. The Langevin potential between a charged particle and a neutral species is given by equation (2.16).

$$V = -\frac{1}{2}\vec{\boldsymbol{\mu}} \cdot \vec{\mathbf{E}} = -\frac{1}{2}\alpha_C \frac{Z^2 e^2}{\left(4\pi\epsilon_0 r^2\right)^2}, \tag{2.16}$$

with $\vec{\mu}$ the dipole moment, Z the number of elementary charges and α_C the polarisibility of the neutral species.

Charged-charged collisions

When two charged particles collide there is a whole range of possible outcomes. A positive and negative ion can exchange charge or bond together to form a neutral molecule in a chemical reaction. Furthermore, positive ions can recombine with electrons and electrons can be detached from negative ions to form a neutral particle. A very important collision type within a plasma is the electron-electron interaction, since these elastic collisions determine the shape of the EEDF, which means, how the electron energy is distributed among electrons. This should not be confused with elastic electron-neutral collisions, which, as we saw earlier in this section, determine the electron temperature and therefore the height of the EEDF. The distribution of energy among electrons is essential because the high energy tail of the distribution determines the rate of endothermic chemical reactions such as ionisation. Energetic processes such as ionisation can only take place due to reactions with high energies located at the high-energy tail of the EEDF.

[3] Imagine trying to propel a truck by throwing tennis balls at it. The tennis balls will bounce off at basically the same speed at which they came in therefore transferring a negligible amount of energy to the far heavier truck.

2.5 Transport in plasmas

As was stated in section 2.3.2, transport of species within a plasma can be described by a diffusion coefficient for neutral particles while both a diffusion and mobility coefficient are required for charged species. These coefficients can be calculated using only collisions with the dominant background gas species since they make up more than 99% of the particles in the plasma. This is done by using collision integrals with the proper collision potential: Lennard-Jones for neutral particles and Langevin for ions. The diffusion coefficient for species i with background gas j is calculated by [37] (page 98):

$$D_{ij} = \frac{3}{16} \frac{k_B^2 T_{gas}^2}{p_i m_{ij} \Omega^{(1.1)}}, \tag{2.17}$$

with p_i the pressure due to particle i, m_{ij} the reduced mass and $\Omega^{(1,1)}$ the appropriate collision integral. The Lennard-Jones diffusion integral for neutral particles will not be given here but has been described by Janssen et al. [37] (page 61). Instead, we will focus on Langevin collisions, for which the collision integral is given by:

$$\Omega^{(1,1)} = \sqrt{\frac{Z^2 e^2 \alpha}{4 m_{ij} \epsilon_0}} A^{(1)} \Gamma\left(5/2\right), \tag{2.18}$$

with Z the charge of the ion, α the polarisability and Γ the gamma function. The total diffusion coefficient is then found from by combining the binary diffusion coefficients D_{ij} weighted by the pressure fraction of the gas species using Blanc's law [40]:

$$\frac{p_{tot}}{D_j} = \sum_i \frac{p_i}{D_{ij}}, \tag{2.19}$$

with p_{tot} the total pressure. The mobilities for charged particles are consequently found using the Einstein relation given by equation (2.13). Finally, the diffusion and mobility coefficients of electrons are calculated using BOLSIG+ [29].

2.5.1 Transport to the wall

For charged species it is common to assume that negative ions are not lost to the walls because they are trapped by the plasma potential. Loss of electrons and positive ions can be described modelled using Bohm velocity derived in section 2.2.2 under the assumption that the electron and positive ion density are approximately equal [41]:

$$\vec{\mathbf{\Gamma}}_e = \vec{\mathbf{\Gamma}}_{i+} = n_{i+} \vec{\mathbf{u}}_B, \tag{2.20}$$

with $\vec{\mathbf{\Gamma}}_e$ and $\vec{\mathbf{\Gamma}}_{i+}$ the electron and positive ion flux to the wall, n_{i+} the positive ion density and $\vec{\mathbf{u}}_B$ the Bohm velocity given in section 2.2.2. Radicals will be lost to the wall with a certain probability given by a so-called sticking coefficient, while neutral particles without unbounded electrons are expected to reflect back into the discharge.

The background gas is typically refreshed using an inlet. Outflow is defined such that the total pressure is kept below the defined pressure of p_0. If the plasma pressure is below this pressure no outflow will take place. If the pressure rises above p_0, the outflow is given by:

$$Q_{out} = \frac{Q_{in}}{\frac{p_0}{p}}, \tag{2.21}$$

with Q_{in} the mass influx of particles and p the current pressure.

2.6 Dust growth in plasmas

In this thesis, all species with more than 12 carbon atoms are qualified as dust. Dust generally forms in plasmas containing chemically active molecules with the tendency to polemerise. Among others, the most common are either carbon-based like methane [19] and acetylene [20], or silicon based like silane [25], or Hexamethyldisiloxaan (HMDSO) [42]. The formation of dust is of particular interest since it can have a significant impact on the plasma itself, as well as in many industrial applications such as material processing. This should not be surprising since carbon and silicon are both convenient elements for substrates and accordingly used routinely in various fields of industry. We have already seen in section 1 that the growth cycle from the precursor gas towards micrometer-sized dust we can distinguish three distinct phases: nucleation, coagulation and accretion. We will now take a closer look at each of these phases separately.

2.6.1 Nucleation phase

The nucleation stage describes the growth from the precursor sub-nanometer sized gas particles to dust particles of typically a few nanometers in size. The nucleation phase is dominated by polymerisation reactions in the plasma chemistry. A typical growth path in the nucleation stage in acetylene (C_2H_2) is called the Winchester mechanism given below [43]:

$$C_2H_2 + e^- \rightarrow C_2H^- + H \tag{2.22}$$

$$C_2H^- + C_2H_2 \rightarrow C_4H^- + H_2 \tag{2.23}$$

$$C_4H^- + C_2H_2 \rightarrow C_6H^- + H_2 \tag{2.24}$$

$$C_6H^- + C_2H_2 \rightarrow C_8H^- + H_2 \tag{2.25}$$

The negative ion gains a carbon pair with every next reaction leading to a net growth of particle by consuming acetylene and ejecting hydrogen gas into the discharge. This is an example of negative ion growth. Similarly there can be positive ion growth, growth due to radicals and ion-ion mutual neutralisation [20]. Hollenstein et al. showed that the density of neutral and positive species decreases rapidly with size, while larger negative ions are very common [44]. We can therefore conclude that negative ion growth is the dominant growth process in most plasmas which can be explained by the fact that negative ions are trapped in the centre of the discharge due to the positive potential (see figure 2.1). Particles in the nucleation stage can be neutral, positively charged or negatively charged. Furthermore, the plasma chemistry is not influenced much by the presence of noble gasses such as argon and helium which is common in dust growth experiments [21]. As the number of dust particles increases, the nucleation phase terminates and coagulation starts.

2.6.2 Coagulation phase

The coagulation stage describes the rapid dust growth from several nanometers in radius up to several tens of nanometers. The density of particles subsequently drops by multiple orders of magnitude [45]. The positive and negative species of several nanometers coagulate together until their size prevents them from carrying a positive charge. Charging of nanoparticles in a plasma can be described by orbital motion limited (OML) originally derived by Langmuir [46]. OML theory assumes that there is a certain impact parameter and therefore cross section at which a nanoparticle collects charges [1], a concept related to what was shown by figure 2.4. The electron and ion currents towards a particle also depend on its floating potential and are given by:

$$I_e = \pi r_d^2 n_e e \sqrt{\frac{8k_B T_e}{\pi m_e}} \exp\left(\frac{e\phi_{fl}}{k_B T_e}\right) \tag{2.26}$$

and

$$I_i = \pi r_d^2 n_i e \sqrt{\frac{8 k_B T_i}{\pi m_i}} \left(1 - \frac{e\phi_{fl}}{k_B T_i}\right), \tag{2.27}$$

with ϕ_{fl} the floating potential, r_d the particle radius and n_e and n_i the electron and ion densities respectively. Assuming that the charge of the nanoparticles is in steady-state, the electron current equals the ion current. Nanoparticles tend to charge negatively due to the higher electron temperature compared to the ion temperature. For example, an electron temperature of 3 eV together with an ion temperature of 0.03 eV, with electron and ion densities of $10^{16}\mathrm{m}^{-3}$ lead to a floating potential of approximately -6 V. The corresponding expected charge on this nanoparticle can be found using the spherical capacitor model:

$$Q_d = 4\pi\epsilon_0 r_d \phi_{fl}, \tag{2.28}$$

with Q_d the expectation of the charge on the dust particle. The charging of nanoparticles can be measured in the lab by the rapid decrease of the electron density. An example of this decrease in electron density in the afterglow of an argon-acetylene discharge is given by figure 2.6.

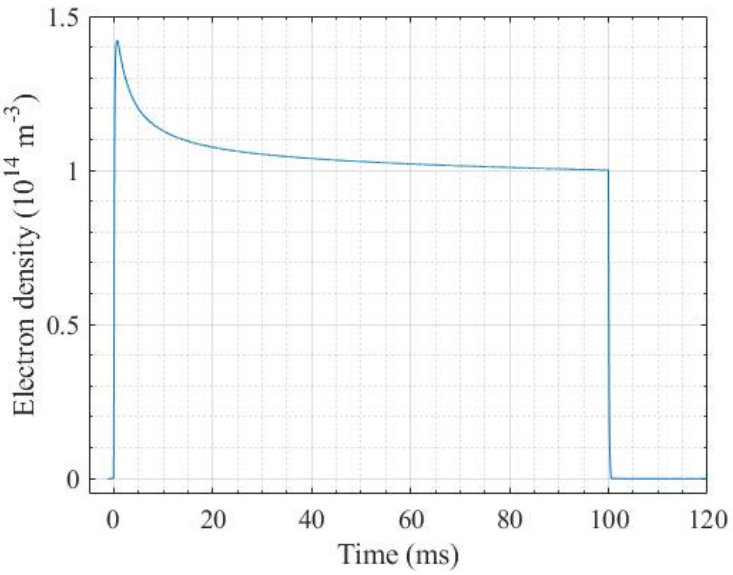

Figure 2.6: Electron density as a function of time in an argon-acetylene discharge. Figure and measurements by Hasani, M.

The growth process of particles in the coagulation phase can be described by the general dynamics equation for aerosols [47]:

$$\frac{dn_d(v_i)}{dt} = \frac{1}{2}\int_0^{v_i} \beta(v_j, v_i - v_j)\, n(v_j)\, n(v_i - v_j)\, dv_j - \int_0^{\infty} \beta(v_j, v_i)\, n(v_i)\, n(v_j)\, dv_j, \tag{2.29}$$

with v_i and v_j the volumes of the coagulating particles and $\beta(v_i, v_j)$ the collision frequency between particle i and particle j. The general dynamic equation states the the change of the density of nanoparticles with volume v_i (left-hand side) is equal to the integrated amount of collisions between nanoparticles with densities v_j and $v_i - v_j$ for $v_i > v_j$ (first term right-hand side), minus the integrated amount of collisions of particles with volume v_i with

any other particle (second term right-hand side). This principle is shown in figure 2.7, where particle i is created from the smaller particles $i-1$ and $i-2$, whilst it is lost due to reactions with any other particle ($i-1$ and $i+1$) creating larger particles. In reality it can be lost due to reactions with any other particles. A nucleation term could be added to create the smallest particles in the coagulation phase.

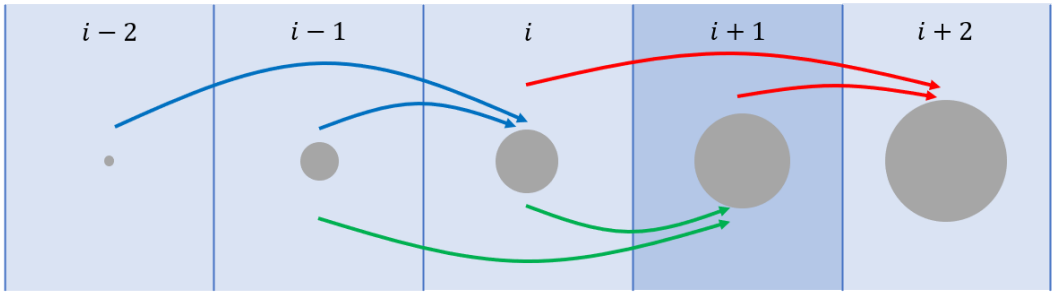

Figure 2.7: Schematic image of coagulation in which particle i is formed out of reactions by smaller particles, but lost due to reactions with any particle.

The general dynamic equation is a fundamental balance equation and should in principle always hold. The challenge for the modeller is to find an appropriate collision frequency β that best describes the physics at play. The simplest choice for $\beta(v_i, v_j)$ is a hard-sphere collision frequency. As long as the particles are much smaller than their mean-free path, which can be reasonably assumed for low pressure conditions, the collision frequency between nanoparticles can be written as a function of their sizes using a hard-sphere collision model [47] [48]:

$$\beta(v_i, v_j) = \left(\frac{3}{4\pi}\right)^{1/6} \left(\frac{6k_BT}{\rho_d}\right)^{1/2} \left(\frac{1}{v_i} + \frac{1}{v_j}\right)^{1/2} \left(v_i^{1/3} + v_j^{1/3}\right)^2, \tag{2.30}$$

with ρ_d the mass density of dust and v_i and v_j the volumes of particles i and j respectively. It is easily verified that the collision frequency is largest for a combination of a very small and a very large particle. Even though equation (2.30) looks rather complex its structure is simply that of a kind of thermal velocity multiplied by a cross section. By realising that $\rho = \frac{m}{v}$, it can be seen that β is of the form of a thermal velocity multiplied by a cross section by writing the volume terms as a cross section: $\left(\frac{1}{v_i} + \frac{1}{v_j}\right)^{1/2} \left(v_i^{1/3} + v_j^{1/3}\right)^2 = V^{2/3} = \left(\frac{4}{3}\pi r^3\right)^{2/3}$. By filling this expression back into equation (2.30) we see that it simply reduces to $v_{thermal}\pi r^2 = v_{thermal}\sigma$, the typical expression for hard-sphere collisions.

Despite the fact that we have concluded that larger dust particles charge more and more negatively, equation (2.30) does not take charging into account, it can therefore only reliably be used up to a certain size where the expected charge is close to zero, after which a charge term should be added which reduces the probability of coagulation between two relatively large dust particles due to their electric repulsion. This charging can be taken into account by adding a charge factor to the coagulation frequency as was proposed by Agarwal et al. [49]: $\beta_{tot} = f_{charging}\beta$ with:

$$f_{charging} = \begin{cases} 1 & \text{if } z_1 = z_2 = 0 \\ 1 - \frac{z_1 z_2 e^2}{4\pi\epsilon_0(r_1+r_2)k_B T_{gas}} & \text{if } z_1 z_2 \leq 0 \\ 0 & \text{if } z_1 z_2 \geq 0 \\ E_{induced} & \text{if } z_1 \neq 0, z_2 = 0, \end{cases} \tag{2.31}$$

Equation (2.31) states that the coagulation frequency is unaltered for interactions between neutral species, it is increased with a charge dependent factor for dust particles of opposite charge, becomes zero for dust particles with similar electric polarity and is a function of an electric dipole for interactions between a charged and neutral dust

particle. At a certain size of several tens of nanometers, all dust particles have an expected charge that is strongly negative such that dust particles can no longer coagulate such that coagulation ends and accretion begins.

2.6.3 Accretion phase

The final growth stage is called the accretion stage, in which dust particles mainly experience surface growth by capturing positive ions and radicals, since they can no longer coagulate with other dust particles. The growth speed is typically far lower than in the coagulation phase, because only much smaller particles can be captured. This does not prevent further growth however, since the dust particles are strongly negatively charged and therefore trapped inside the plasma bulk by the Coulomb force. Depending on the circumstances, this process can continue until eventually the particles reach micrometer dimensions and the particles are pushed out of the discharge by the ion drag force, which grows faster than the Coulomb force [24]. The ion drag force is the force that drifting ions exert on dust particles [1]. This drift force consists of two parts. Firstly, ions can simply bump into dust particles. Secondly, a Coulomb force can be exerted due to scattering of ions on the dust particles.

With all the dust removed from the centre of the discharge, the way is clear for a new growth cycle. Figure 2.8 shows the free electron density as a function of time for dust growth measurements in HMDSO, which is expected to show similar trends compared to dust growth in acetylene [42]. The electron density initially drops, since dust particles start charging negatively after which it becomes nearly constant since the accretion phase started and dust particles stopped draining electrons from the plasma. After about 80 s, the dust particles are pulled out of the discharge, the electron density is partly restored and a new growth cycle starts.

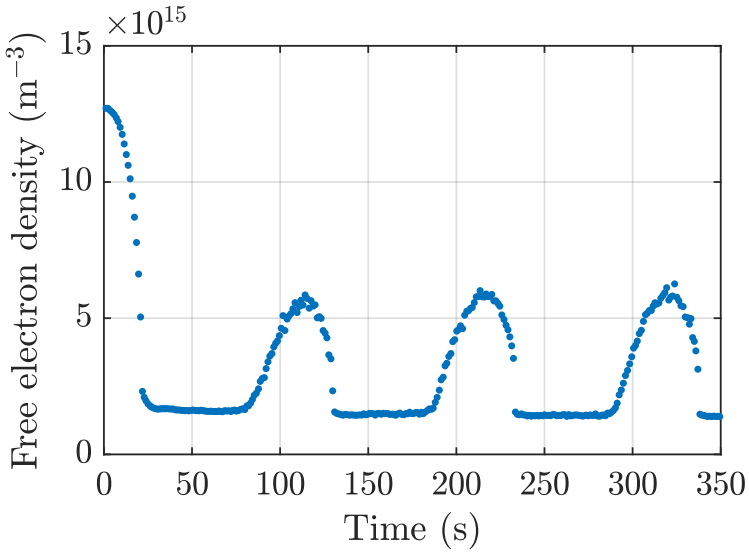

Figure 2.8: The electron density as a function of time. Measurements by Donders, T [42].

3 Plasma chemistry

So far, we have seen plasma theory that is quite general and can therefore be applied to most low-pressure plasmas. The plasma chemistry describes the nucleation phase of dust growth, the phase from the precursor to particles up to a few nanometers, in terms of chemical reactions of which the growth reactions are mainly polymerisation reactions.

It is now time to forsake generality and dive into the particular plasma at hand. This thesis will focus on dust growth in a plasma starting with the precursor ethyn (C_2H_2), more commonly known as acetylene, which is a hydrocarbon containing a triple bond between the carbon atoms. The triple bond is particularly interesting, since it is much stronger than regular single bonds, leading to different plasma dynamics compared to those containing single bonds in methane (CH_4) or double bonds in ethylene (C_2H_4) for example [19]. It was also shown that acetylene production is one of the main processes even in plasmas which initially do not contain acetylene, but methane or ethylene instead. Although C_4H or C_4H_2 plasmas start without acetylene, acetylene turns out to be the precursor for dust growth nonetheless [50]. It is not surprising that both carbon-like as well as silicon-like molecules such as silane (SiH_4) are among the most studied molecules in plasma physics since they are also among common in applications. Both elements carbon and silicon are abundant on earth. Carbon is vital to life being the basis of DNA, while silicon is the most important material for electronics being a semiconductor.

3.1 Literature study

The dust growth models described in this thesis all start with the precursor C_2H_2. In recent years, a lot of research has been done on dust growth in acetylene, either in pure acetylene [20] [51] [31], or admixed to a noble gas such as argon or helium [32] [52]. So far, various experimental and theoretical studies have been performed to describe the chemical reactions in acetylene discharges. Doyle et al. worked on a simple chemistry growth model where C_4H_2 and C_6H_2 called di-acetylene and tri-acetylene are formed [53]:

$$C_2H_2 + e^- \rightarrow C_2H + H + e^- \tag{3.1a}$$

$$C_2H_2 + C_2H \rightarrow C_4H_2 + H \tag{3.1b}$$

$$C_4H_2 + C_2H \rightarrow C_6H_2 + H \tag{3.1c}$$

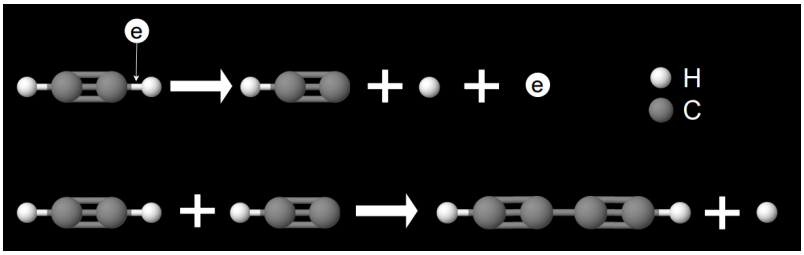

Figure 3.1: Schematic image of the formation of C_4H_2 from C_2H_2 and electrons.

Equations 3.1 show that the larger species C_4H_2 and C_6H_2 are formed by first knocking a hydrogen atom off the acetylene molecule forming the radical C_2H, which can in turn insert into the acetylene molecular structure forming C_4H_2. Furthermore, the alternating single and triple bond structure is illustrated in figure 3.1.

Deschenaux et al. showed using mass spectroscopy that almost all molecules have an even number of carbon atoms, which means that carbon atoms tend to come in pairs suggesting that the triple bond in an acetylene molecule is indeed rarely broken in the nucleation stage [19]. Stoykov et al. modelled the growth chains using positive and

negative ions and showed the presence of aromatic compounds [54]. Mass spectrometry had already shown the importance of growth via positive ions [55]. Herrebout et al. extended the chemistry with larger species (C_8H_2 and C_8H) and positive ions in a one-dimensional model [56]. A full self-consistent model of the plasma chemistry in acetylene was developed by De Bleecker et al. [20]. This model contains both positive and negative ion growth channels and contains species up to 12 carbon atoms, which will be used as the basic chemistry in this thesis. It must be stated that the self-consistent one-dimensional model of De Bleecker as well as most models that followed have not taken the presence of aromatic compounds into account despite the fact that Stoykov et al. as well as De Bleecker herself found that these particles are present in the discharge [57].

The chemistry was later extented by Mao et al. with the addition of larger species, a new negative growth channel containing $C_{2n}H_2^-$ with $1 < n < 6$ via dissociative attachment and a few cyclic rings [51]. Their results do arguably describe experiments better than previous published work but the Winchester mechanism, $C_{2n}H^- + C_2H_2 \rightarrow C_{2n+2}H^- + H_2$ with $1 < n < 5$ remains the dominant growth mechanism. Furthermore, it was shown that the presence of a diluting noble gas such as argon does not significantly change the plasma chemistry. This idea was later questioned by Akhoundi et al [32]. They showed that diluting acetylene with argon or helium increases the electron density and therefore also the rate at which acetylene dissociates which subsequently enhances nucleation.

Jimenez et al., who worked on the plasma chemistry of acetylene in argon and helium, confirmed once more the fact that ions with an even number of carbon atoms are the much more common than the odd carbon species [33]. The mass spectra showed very similar patterns in argon and helium which once again suggests that the presence of noble gases has no large impact overall.

3.2 Particles and reactions

Extensive research has been done on the plasma chemistry of acetylene as discussed in the previous section. The species present in the model can be found in table 1 in appendix A.1, which are the species used by De Bleecker et al. but ignoring vibrational excitations [20]. The electron impact reactions are given in table 2, ion-molecule reactions in table 3 and molecule-molecule reactions in table 4 in appendix A.2.

Furthermore, it is assumed that the gas temperature is constant. This assumption could be relaxed since the change in gas temperature can theoretically be calculated using the the temperature dependent heat of formation, which for $T = 298\,\mathrm{K}$ are given in appendix B for the species in the model [58]. The temperature dependent heat of formation can be calculated using the empirical formula found by Burcat et al. [59], which together with temperature dependent reaction rates, could be used to take changes in gas temperature into account. In this thesis however we stick to the assumption of a constant gas temperature. Furthermore, as can be seen from equation (2.15), the integral $\sigma(E)f(E)v(E)dE$ simplifies to a constant under the constant temperature assumption, leading to the constant reaction rate coefficients in table 3 and table 4.

The electron energy distribution function (EEDF) is calculated from the Boltzmann equation (equation (2.4)) using a two-term approximation [29]. Cross sections are still required in order to determine the reaction rate coefficient for electron impact reactions. The cross section for ionisation is given by:

$$\sigma_{ion} = \frac{10^{-17}\,(\mathrm{m}^2)}{EI_c}\left(A_1 \ln\left(\frac{E}{I_c}\right) + \sum_{j=2}^{N} A_j (1 - \frac{I_c}{E})^{j-1}\right), \tag{3.2}$$

with E the energy in eV, I_c a constant energy close to the threshold energy and A_j fitting parameters given by Janev et al. [60]. The cross section for electron impact dissociation of C_2H_2 is given by:

$$\sigma_{DE}^{tot}\,(C_2H_2) = 10^{-20}\,(\mathrm{m}^2)\,34.6 F_2^{DE}\left(1 - \frac{E_{th}}{E}\right)^3 \frac{1}{E}\ln\,(e + 0.15E), \tag{3.3}$$

with $F_2^{DE} = 1.704$, E and E_{th} the energy and threshold energy in eV, and e the base of the natural logarithm [60]. The cross section for dissociative attachment was measured by Rutkowsky at al. and approximated by two gaussian peaks centered at 2.5 eV and 7.9 eV with maxima of $7 \times 10^{-24}\,\mathrm{m}^2$ and $7.5 \times 10^{-24}\,\mathrm{m}^2$ and widths of 1 eV and 2 eV respectively [61].

It is clear that the particles and reactions present in the model do not tell the whole story. As mentioned before, vibrational excitations as well as cyclic rings have been neglected our model. Furthermore, the largest species present in the model is $C_{12}H_6$, which is clearly much smaller than the required radius for coagulation which was determined to be several nanometers in section 2.6.2. That means that optimally, larger species as well as the corresponding polymerisation reactions should be included in the model. As far as we know however, no detailed chemical reaction schemes nor the rate coefficients have been measured for such reactions for species containing more than 12 carbon atoms in a low pressure plasma environment. We will come back to this in section 7.2.2.

4 Simulation

Up to this point, we have seen the chemical reactions and physical equations that govern dust growth in a low-pressure plasma environment. In this section, we will describe the numerical methods and techniques used in this thesis to solve these equations and generate meaningful results. It was already shown in section 2.1.2 that an exact simulation in which all particles are tracked is technically unfeasible since the number of particles is too large for current storage hardware and the required number of computations to the describe all these particles is not reasonably possible either. This is why every species is described by a number density function as well as an energy density function. The majority of simulations performed in this thesis are done in a zero-dimensional global model which means that all spatial dependencies are averaged over the spatial domain such that $\boldsymbol{\nabla}_r = 0$ for all quantities at each point in time. Under this assumption, the drift diffusion equation (2.5) simplifies drastically, since the drift term vanishes.

In this section, we will see how the continuity equation is solved numerically using a spatial discretisation, taking into account chemical reactions, wall losses and pumping. We will then show how coagulation is simulated by solving the general dynamic equation using a discretised volume space. We will also see how charging of nanoparticles can be taken into account. Finally, we will briefly discuss how the model can be extended and improved by taking into account spatial variances and using multiple time-scales.

4.1 Discretisation

The basis for the numerical simulation is the drift-diffusion equation given by (2.5), which is solved in discrete time-steps Δt which we call an iteration:

$$\mathbf{n}_{new} = \mathbf{n}_{old} + \Delta\mathbf{n} \tag{4.1}$$

and

$$\Delta\mathbf{n} = \mathbf{S}\Delta t, \tag{4.2}$$

with $\mathbf{n}$ the density vector containing the densities of all species present in the model [4], $\Delta\mathbf{n}$ and $\mathbf{S}$ the vectors containing the change of the respective species and source of species during a time Δt, which has to be chosen sufficiently small for a stable and robust simulation. The flux term in the continuity equation vanishes since it was demonstrated by equation 2.12 that it depends on $\vec{\mathbf{E}} = -\boldsymbol{\nabla}V$ and $\boldsymbol{\nabla}n$ which are both zero in the global model. The source term $\mathbf{S}$ contains the different ways in which species can be formed or lost, which is by chemical reactions in the bulk, transport to the wall and due to inflow and outflow due to pumping:

$$\mathbf{S} = \mathbf{S}_{wall} + \mathbf{S}_{pumping} + \mathbf{S}_{chemical}, \tag{4.3}$$

with $\mathbf{S}_{wall}$ the vector containing the wall losses for each species. The elements of $\mathbf{S}_{wall}$ describe the wall losses for the separate species given by:

$$S_{wall} = C_s \Gamma_{wall} A/V, \tag{4.4}$$

where $\Gamma_{wall} = n u_{wall}$ is the flux density towards the wall, u_{wall} is the Bohm velocity (equation (2.8)) for charged particles and the thermal velocity (equation (2.7)) for neutral particles. A and V are the area and volume of the cylindrical vessel with height and radius of 3 cm respectively. C_s is the sticking coefficient, which is equal to one for positive ions and equal to zero for negative ions. The sticking coefficients for neutral particles are given in appendix C. 90% of all hydrogen atoms that stick to the wall flow immediately back into the discharge in the form of hydrogen

[4] Vectors without an arrow such as $\mathbf{n}$ imply column matrices, while vectors with an arrow such as $\vec{\mathbf{E}}$ imply physical vectors with a spatial direction.

gas. Even though the radicals $C_{2n}H$ for $1 < n < 6$ are expected to occasionally pick up a hydrogen atom at the wall according to De Bleecker et al. [20], this process has been neglected since no proper quantification of this process was found.

The pumping term $\mathbf{S}_{pumping}$ describes acetylene inflow and outflow due to pumping. Inflow occurs at 20 sccm and loss due to pumping will reduce the densities of all species if the calculated pressure becomes higher than the set pressure of 40 Pa as was given by equation (2.21).

$\mathbf{S}_{chemistry}$ contains the density gains and losses of each species due to chemical reactions. This vector is easiest calculated using linear algebra by multiplication of a stoichiometric matrix $\mathbf{W}$ and a reaction rate vector $\mathbf{R}$ [62]:

$$\mathbf{S}_{chemical} = \mathbf{WR}, \tag{4.5}$$

and

$$\mathbf{R} = k_r(T)\prod_{\mathbf{i=1}}^{\mathbf{N_p}} n_i^{\nu_{i,r}}, \tag{4.6}$$

with $k_r(T)$ the rate coefficient of reaction r, n_i the density of species i and N_p the number of different species in the model. $\nu_{i,r}$ is the stoichiometric coefficient for construction and destruction of species i in reaction r, which is equal to the number of particles of this species type i that participates in reaction r. This is convenient since $n_i^{\nu_{i,r}} = n_i^0 = 1$ for species i that are not involved in reaction r, so they do not influence the corresponding rate. In our model $\nu_{i,r}$ can only be zero or one. $\mathbf{W}$ contains the stoichiometric coefficients, for every reaction (rows), for every species (columns), with positive values describing particle construction and negative values describing particle destruction. Solving the matrix-vector product using an appropriate Δt together with the wall and flow terms gives the final source term for a particular iteration.

Since the gas temperature is assumed constant, the source term in equation (4.4) only depends on the densities and the rate coefficients for reactions without electrons which, for the reactions present in the model, are all given in table 3 and table 4. The reaction rates for electron impact reactions however are calculated using equation (2.15), where the cross sections $\sigma(E)$ are taken from lookup tables LXCAT of which the values are interpolated to get values for all energies [63]. $f(E)$ is found by solving Boltzmann equation in two-term approximation using BOLSIG+ at every iteration.

4.2 Coagulation

The coagulation phase in the dust growth process has many similarities to aerosol physics and can therefore be simulated using the general dynamic equation (GDE) for aerosols given in equation (2.29). The modelled volume range will be discretised using bins of species, which will represent V_i and V_j in the GDE. The simplest and most robust discretisation technique is based on using integer multiples of a single chemical unit or building block. We will call this linear discretisation. A further advantage of linear binning is that it ensures that any combination of volumes leads to a new volume which is also in the model:

$$V_i + V_j = \alpha V_1 + \beta V_1 = V_k = (\alpha + \beta)V_1. \tag{4.7}$$

It follows from α, $\beta \in \mathbb{N}$ that $\alpha + \beta \in \mathbb{N}$. The drawback of the linear discretisation is that it is unable to cover a large volume range without using a very large number of bins which is computationally expensive. It was discussed in section 2.6.2 that the coagulation phase describes particles from a few nanometers up to several tens of nanometers in diameter, which describes particles of various orders of magnitude in volume requiring thousands of bins.

This is why it can be beneficial to divide the volume space up exponentially into bins such that the first bin contains all particles with volumes $V_i = gV_{i-1}$ with g the growth factor [25] [31] [64]. Instead of covering a volume domain,

these bins are a typical volume and it is implicitly assumed that particles can only have the volume of one of the bins. Choosing a small value for g leads to a more accurate model, since there are more volumes at the cost of becoming more computationally expensive, since more bins are required to cover the entire volume domain. These bins can be used as v_i and v_j in the general dynamic equation (2.29). Since the growth factor g can be any number larger than one, the coagulation of two different bins does in general not lead to a volume which exactly fits inside a new bin like it did in the linear binning case. χ_{ijk} determines the fraction of the volume $v_i + v_j$ that will be distributed to volume k. The splitting parameter is defined such that mass is conserved. The splitting parameter is given for a constant growth factor by equation (4.8) [48]:

$$\chi_{ijk} = \begin{cases} \frac{v_{k+1}-(v_i+v_j)}{v_{k+1}-v_k} & \text{if } v_k \leq v_i + v_j \leq v_{k+1} \\ \frac{(v_i+v_j)-v_{k-1}}{v_k-v_{k-1}} & \text{if } v_{k-1} \leq v_i + v_j \leq v_k \\ 0 & \text{otherwise.} \end{cases} \tag{4.8}$$

The χ matrix is trivial for the linear binning case giving one if $i+j=k$ and zero otherwise. The coagulation analysis performed in the PLASIMO framework, which is designed to model the plasma chemistry and therefore requires predefined species and chemical reactions. Lets see what happens if we assume a growth factor is 1.5, starting from $C_{12}H_2$[5] the next particle has to be $C_{18}H_3$ followed by $C_{27}H_{9/2}$ which is problematic for the PLASIMO software because it cannot deal with fractional particles. In fact, fractional species will appear if $g \notin \mathbb{N}$ as long as the number of bins is sufficiently large. The most obvious choice for the growth factor is therefore 2. We will demonstrate by means of an example how mass is conserved for the case of a growth factor of 2. Lets assume that the particles involved are: $C_{12}H_2$, $C_{24}H_4$ and $C_{48}H_8$, which double in volume with every next particle. Once the species in the model are known, the χ matrix is easily constructed since it only depends on the relative volumes. It is given for this case by figure 4.1. The reactions can be constructed using equation (2.29) and equation (4.8):

$$C_{12}H_2 + C_{24}H_4 \rightarrow 2\chi_{122}C_{24}H_4 \tag{4.9a}$$

and

$$C_{12}H_2 + C_{24}H_4 \rightarrow 2\chi_{123}C_{48}H_8, \tag{4.9b}$$

with $\chi_{122} = 1/2$ and $\chi_{123} = 1/2$ as given in figure 4.1. The factor 2 on the right hand side is due to the degeneracy of the reactions which is also clear from the fact that χ is symmetric. In this specific case all the coefficients in equations (4.9a) and (4.9b) become unity. Equation (4.9a) therefore loses $C_{12}H_2$ and equation (4.9b) gains $C_{12}H_2$ ensuring that mass is conserved overall, since the reaction rate only depends on the the parent particles which are identical, as can be seen from the coagulation frequency which was given by equation (2.30).

In this equation, the mass density of the dust is taken to be the mass density of amorphous carbon $\rho = 2 \times 10^3\,\mathrm{kg/m^3}$ [65]. Using this mass density and the particle masses, the radii and volumes can be estimated.

A drawback of exponential binning is that the coefficients become increasingly more cumbersome for larger systems. We can also combine linear and exponential binning for example by having 10 linearly growing species ($C_{12i}H_{2i}$ for $i \in [1, 10]$) and 10 exponentially growing species ($C_{120*g^j}H_{20*g^j}$ for $j \in [1, 10]$) with growth factor g. The advantage of using a natural number as growth factor is that all the elements in the χ matrix are rational. This can easily be seen from equation (4.8) by realising that every volume in the model v is a multiple of v1. The idea of combining linearly and exponentially growing bins is an interesting way to attempt to cover a large volume range without giving up too much spatial resolution. Even though it was shown by equations (4.9) that chemical reactions can always be constructed as long as all elements of χ are rational it is not easy to do this in practise. If there are n species of which k linearly growing and l exponentially growing, it is trivial to prove that the formation of species $i > k$ is formed using species 1 and $i-1$ with a corresponding $\chi_{1,i-1,i} = \frac{1}{2^{i-k-1}k}$. Correspondingly, species i is also formed from a reaction between species 1 and species i the reaction of which can be determined using $\chi_{1,i,i} = 1 - \frac{\chi_{1,i-1,i}}{2}$.

[5] We will see in section 5.2 why $C_{12}H_2$ is chosen.

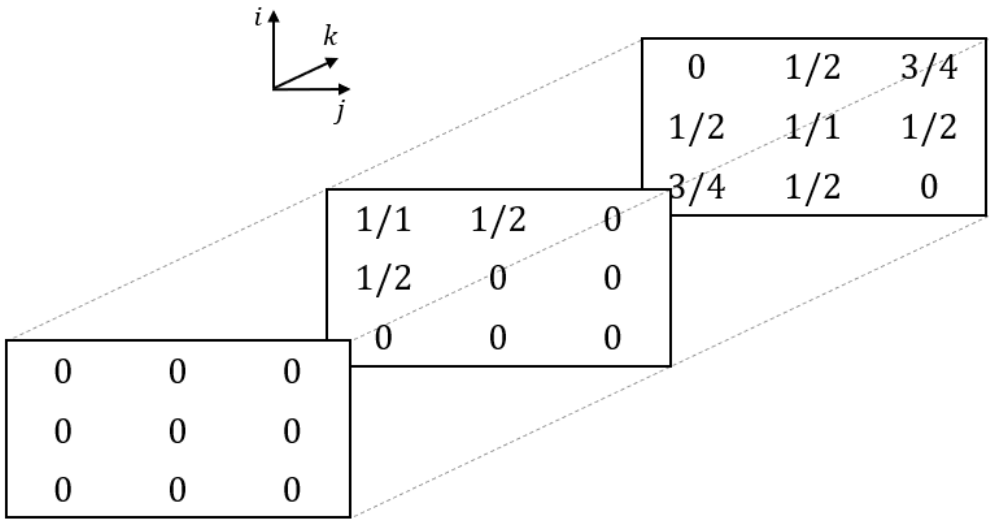

Figure 4.1: The full χ matrix with χ_{111} in the top left in front and χ_{333} at the bottom right at the back with χ_{ijk} defined as the fraction of the coagulated particle of the combination of particles i and j that ends up in bin k.

The fractions clearly become more and more numerically problematic for larger values of k and l. If for example $k = 20$ and $l = 10$, the largest particle is $C_{245760}H_{20480}$. It is not trivial to estimate the size of this particle but let us assume for the sake of argument that this is an existing dust particle. We can then calculate $\chi_{1,29,30} = \frac{1}{10240}$ and $\chi_{1,30,30} = \frac{20479}{20480}$ which are very close to zero and one such that the simulation becomes prone to numerical errors. This analysis can therefore not be extended indefinitely and some caution is warranted.

Charging of nanoparticles can be taken into account using the floating currents given by equation (2.26) and equation (2.27). If the parameters $\hat{T}_e$, T_i, n_e and n_i are constant, the expected charge can be calculated using equation (2.28) for all particles beforehand based on the particle size. Assuming that dust particles are approximately spherical, the radius required for equation (2.28) can be estimated using:

$$\frac{4}{3}\pi r^3 = m/\rho, \tag{4.10}$$

with r the radius, m the mass and ρ the mass density of dust estimated from the density of amorphous carbon which is $2 \times 10^3\,\mathrm{kg/m^{-3}}$ [65]. Particles with an expected charge: $-(2n-1)\,e/2 \leq ne \leq -(2n+1)\,e/2$ then carry a charge $-ne$ in the simulation. It should be noted however that the charge that these particles carry in reality is stochastic in nature. A more accurate way to model charging of nanoparticles is by taking into account the full distribution function of charges instead of just the expectation. Numerical studies on the charge distributions have been performed in silane plasmas by Santos et al. [66], based on a Gaussian charge distribution model developed by Matsoukas et al. [67].

When charging is taken into account by using equation (2.31) reactions between two negatively charged particles are skipped and an extra electron source is included to assure the conservation of charge where needed. In practise, there is a transition phase between gaseous and solid particles which is not well understood. For the purpose of this model, it is assumed that coagulation starts where reliable chemical data is no longer available which is at $C_{12}H_X$ species. It is implicitly assumed that these species are therefore dust and spherically shaped.

4.3 Extensions and limitations

4.3.1 1-Dimensional simulations

The time-discretisation and coagulation methods that have been explained in section 4.1 and section 4.2 are applicable to the one-dimensional case as well. The drift and diffusion terms from the drift-diffusion equation however do not vanish in this case. This means that spatial dependencies appear in the relevant equations and a spatial grid is required to solve these numerically. The chemical source term is now determined in each spatial node according to equation (4.5). Transport of species is simulated using diffusion coefficients and mobilities determined from the collision integrals given by equation (2.18). Transport of dust particles is discussed briefly in section 7.2.2.

4.3.2 Time scales

It was shown in section 4.1 that the time-step Δt should be chosen appropriately small in order so solve equation 4.2 stably. The time-step chosen in our model is equal for all processes and does therefore not the difference between the time-scales of various processes into account. It is generally assumed however that the nucleation phase takes place at the nanosecond timescale, whilst coagulation processes are generally far slower which means that they can be modelled in the microsecond timescale. The current PLASIMO infrastructure cannot use different time-scales for different processes so slow processes in the millisecond range could only be simulated by taking $\mathcal{O}(10^6)$ iterations which was the main limitation of the simulation.

4.3.3 Accuracy

The relative numerical accuracy for doubles in PLASIMO is $1/2^{53}$ which is approximately 16 orders of magnitude. The real accuracy used in the simulations however is given by the absolute and relative tolerance which are used by the solver LSOSA [68], which is an input parameter chosen to be 10^{-4}, the default value for the simulations. A brief accuracy study will be performed in section 5.5.

5 Results global model

Now we have seen the relevant physical equations and principles in section 2, the relevant chemistry in section 3 and the mathematical simulation tools in section 4, it is time to run some numerical simulations. For the sake of completeness, we will first briefly summarise the plasma conditions and parameters in section 5.1. We then continue with the results of the simulation of just the nucleation (plasma chemistry) phase in section 5.2, after which coagulation is added to the model using linear and exponential species sets in section 5.3. Finally, the charging of nanoparticles will also be taken into account in the simulations in section 5.4.

5.1 Initial conditions and model parameters

The plasma is generated in a cylindrical parallel plate reactor with a length and diameter of 3 cm. One electrode is capacitively coupled to a RF power supply at 13.56 MHz with an input power of 5W. The pressure in the vessel is fixed at 40 Pa, while the gas temperature is fixed to remain constant at 400 K. These conditions are similar to the conditions used by De Bleecker et al. [20] allowing for numerical comparisons.

The model starts with more than 99.999% acetylene at a density of $7 \times 10^{21}\,\mathrm{m}^{-3}$ and an electron and positive acetylene ion density of $10^{16}\mathrm{m}^{-3}$ to initiate the plasma chemistry. The initial electron temperature is set at 3 eV, which is typically found experimentally for these types of plasmas [54]. Acetylene flows into the plasma at a constant rate of 20 sccm.

5.2 Nucleation phase results

We have run the model and will now focus on the time evolution of the densities and electron temperature and compare the output values relevant for coagulation such as the electron temperature and density, as well as densities of the species containing 12 carbon atoms to literature. These values will consequently be used as the initial species for simulations of the coagulation phase. Furthermore, the density of gas molecules, negative ions and radicals are discussed since these are indicators of the reliability of the model. Some relevant output parameters are shown in figure 5.1. The outputs found from the global model are in good agreement with the results from literature. As shown in figure 5.2, the electron temperature is found to be between 2.5 eV and 3 eV which is in good agreement since the electron temperature is typically estimated to be in the 2 eV to 4 eV range. For example, De Bleecker et al. [20] found an electron temperature of approximately 2 eV in the bulk of the plasma in similar conditions [20], Liu et al. found a slightly higher electron temperature of approximately 4 eV in the presence of coagulation [31], and Jimenez et al. found values between 2 eV and 4 eV in the presence of argon at lower flow rates [69].

As can be seen in figure 5.1a, the densities of the molecular species are also in reasonable agreement with the results by De Bleecker et al. [20], with acetylene remaining abundant at a density of $2 \times 10^{21}\,\mathrm{m}^{-3}$ and hydrogen gas also reaching a comparable density. This implies that according to this simulation, hydrogen gas also becomes a relevant background species for diffusion and mobility coefficient calculations required for 1D simulations, which can be seen from Blanc's law given by equation (2.19). C_4H_2 also reaches a density higher than $10^{20}\mathrm{m}^{-3}$, whilst the densities of larger species remain several orders of magnitude lower. for example, the density of $C_{12}H_2$ in our model remains multiple orders of magnitude lower than the value found by De Bleecker et al. [20], who found a density of around $5 \times 10^{19}\,\mathrm{m}^{-3}$. This may be due to the fact that a longer simulation time is required to reach this value. Unfortunately, as was explained in section 4.3.2, it is very costly to run the model for longer times due to the small time-steps that are required to simulate the plasma chemistry accurately, such that it was not feasible to run the model until steady-state was reached. Potential techniques to speed up the simulation will be proposed in section 7.2.

As shown in figure 5.1b The negative ion densities are also in good agreement, with $C_{12}H^-$ reaching the highest density at approximately $10^{16}\mathrm{m}^{-3}$ and the densities of the other negative ions being around an order of magnitude lower. The biggest difference is the electron density which is found to be higher than $10^{16}\mathrm{m}^{-3}$ in our model, while De Bleecker et al. [20] found a value below $3 \times 10^{14}\,\mathrm{m}^{-3}$. This can potentially be explained from the fact that electrons are highly mobile and therefore less suitable for global models, where this spatial variance is not taken into account. The higher electron density can potentially be explained by the fact that electrons are leaving the discharge at a

higher velocity than the assumed Bohm velocity. However, the thermal velocity is expected to highly overestimate electron losses, since it does not take the sheath potential into account which pushes the electrons back into the plasma bulk. The one-dimensional implementation by De Bleecker et al. [20] did not have to assume a velocity since the formation of the sheaths and behaviour of the local electrons is simulated explicitly. The agreement with simulations by Liu et al. is better, since they found a value slightly above $10^{16}\mathrm{m}^{-3}$ in the presence of coagulation [31]. Furthermore, the electron density can be very sensitive to gain and loss mechanisms such as second electron emission and sputtering that have been neglected in this model [70] [71].

Finally, the radical densities are given in figure 5.1c and found to be in very good agreement with De Bleecker et al. [20], with C_2H_3 the most abundant with a density of approximately $1 \times 10^{18}\,\mathrm{m}^{-3}$. The H density found in our model is higher than what was found by De Bleecker et al. [20], which is probably due to the way in which hydrogen flowback is modelled. In our model, hydrogen lost to the wall flows back in the form of either H_2 or H depending on the number of hydrogen atoms lost to the wall. It is possible that De Bleecker et al. [20] modelled this using H_2 and $\frac{1}{2}H_2$ instead. The densities of C_2H, C_4H and $C_{12}H$ are found to be a few orders of magnitudes lower compared to C_2H_3, with the density of C_2H being higher than that of C_4H, which once again is higher than $C_{12}H$.

The results are remarkably accurate overall given that the model is significantly simplified leaving out all spatial dependencies. It is therefore not only interesting but also feasible to add coagulation to the global model.

The species present in the plasma chemistry we have seen so far might not directly take part in the coagulation phase and are growing further by polymerisation reactions instead. Details about these reactions are however unknown. Since the largest particles present in the model are the particles containing 12 carbon atoms, it seems reasonable to use those as precursor for the coagulation phase. The evolution of these species is shown in figure 5.1d. The positive ionic species $C_{12}H_6^+$ appears first, since it was shown by Knight et al. that positive ion condensation reactions are a relatively fast process [72]. The densities of positive ions and radicals fall after about one millisecond however as losses to the wall become significant at this time scale. It turns out that $C_{12}H_2$ is the most abundant particle in the nucleation phase so this species will be used as a precursor for coagulation.

5.3 Coagulation without charging of nanoparticles

The simulations including coagulation will be discussed using various cases starting with $C_{12}H_2$. The coagulation frequency is calculated using equation (2.30) and the radius of $C_{12}H_2$ is calculated using equation (4.10) and found to be approximately 0.3 nm. The radii for larger species scales with $V^{1/3}$ so the radius of $C_{1200}H_{200}$ is approximately 1.4 nm. Coagulation will be studied using three distinct cases:

Case 1: Coagulation for linear binning $C_{12}H_2$ up to $C_{1200}H_{200}$.

In the first case we will analyse coagulation for linear bins $C_{12i}H_{2i}$ for $i \in [1, 100]$. The initial density of the first $C_{12}H_2$ bin is set to $10^{18}\mathrm{m}^{-3}$ in agreement with figure 5.1d. All combinations of species $C_{12i}H_{2i}$ and $C_{12j}H_{2j}$ are taken into account for $i + j \leq 100$.

Case 2: Coagulation for linear binning $C_{12}H_2$ up to $C_{1200}H_{200}$ with a constant production of $C_{12}H_2$.

The first case describes growth from limited supply of initial $C_{12}H_2$. This is useful to get a basic understanding of the processes and time-scales at which coagulation takes place for uncharged species. In reality however, the plasma will provide a source of $C_{12}H_2$, which we can determine using the nucleation model in section 5.2. The effect of the production of $C_{12}H_2$ will be discussed.

Case 3: Coagulation for exponential binning species $C_{12}H_2$ up to $C_{1536}H_{256}$ with growth factor $g = 2$.

In case 1 and case 2, we have seen that coagulation can be modelled using a linear binning model. The 100 species used were near the limit of what was computationally feasible. 100 species cover a volume range of two orders of magnitude, which is an interesting starting point. As explained in section 2.6.2 however, coagulation takes place up to particles of several tens of nanometers in radius, which is about five orders of magnitude larger than $C_{12}H_2$. It

Figure 5.1: Key outputs of the global model of the plasma chemistry. (a) the densities of gas molecules, (b) shows the densities of negative ions and electrons and (c) shows the densities of radicals and (d) shows the densities of species containing 12 carbon atoms as a function of time.

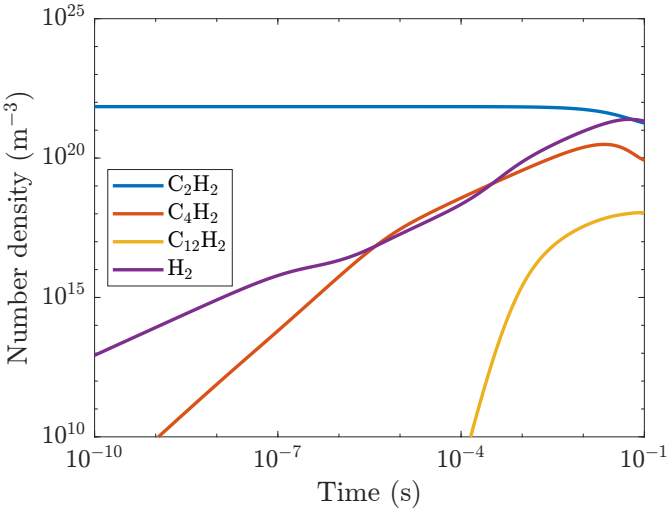

(a) Number densities of gas molecules as a function of time.

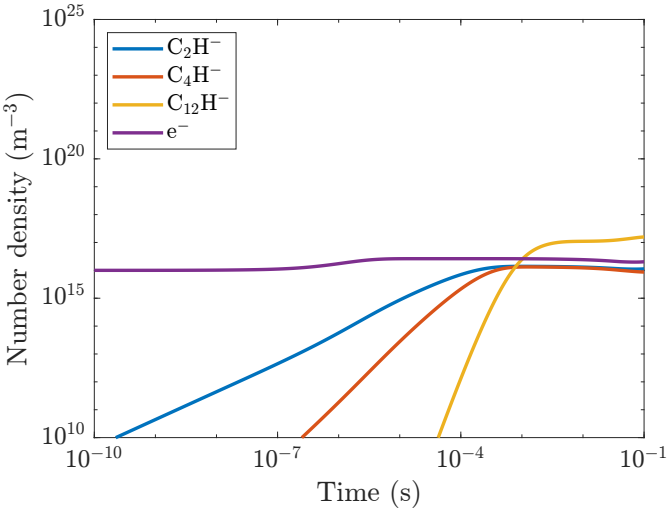

(b) Number densities of electrons and negative ions as a function of time.

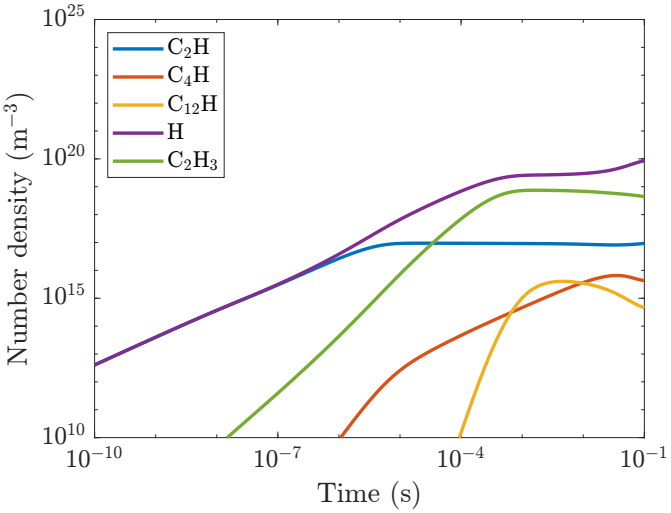

(c) Number densities of radicals as a function of time.

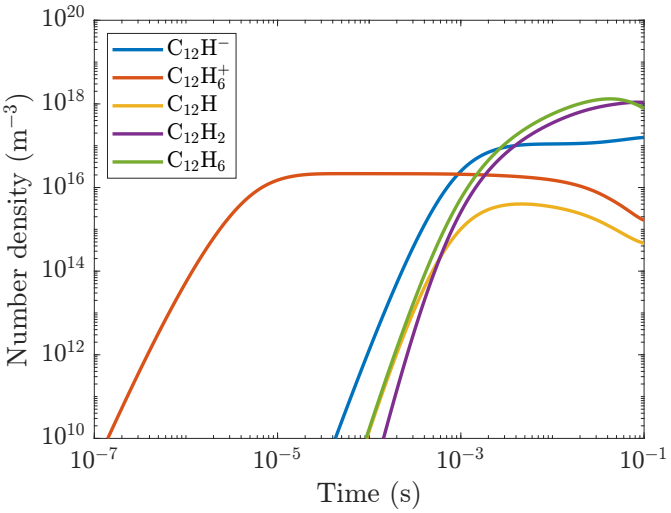

(d) The number densities of species containing 12 carbon atoms as a function of time.

would be interesting to model this entire volume range. This is not possible in a linear binning model, since the use of the required >> 100 species is not computationally viable in more complex models, especially when it is connected to the nucleation model, or when spatial dependencies are taken into account. This is why it is interesting to consider exponential binning, so that fewer particles are required to cover the desired volume range. The particles present in the model are: $C_{12g^{i-1}}H_{2g^{i-1}}$ for $i \in [1, 8]$ and $g = 2$, such that $C_{1536}H_{256}$ is the largest particle nearly identical to the largest particle in case 1 and case 2. It was demonstrated that the χ matrix given in equation (4.8) is required to conserve mass. Coagulation with exponential binning will be explored with a $C_{12}H_2$ production term analogous to case 2. We will now discuss the cases separately in sections 5.3.1, 5.3.2 and 5.3.3.

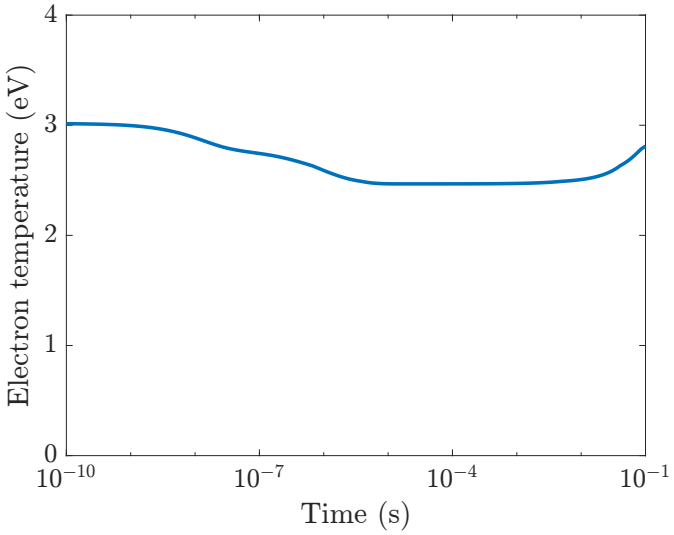

Figure 5.2: Electron temperature as a function of time.

5.3.1 Case 1: Coagulation for linear binning $C_{12}H_2$ up to $C_{1200}H_{200}$

In this section, we will look at the time evolution of coagulation starting with only $C_{12}H_2$, which can coagulate in time to create all the species $C_{12n}H_{2n}$ with $n \in [1, 100]$, integers between 1 and 100. Without the production of $C_{12}H_2$, all particles should eventually coagulate to $C_{1200}H_{200}$, since no processes that can dissociate particles are taken into account. Figure 5.3 shows how the densities of the species $C_{12}H_2$, $C_{120}H_{20}$ and $C_{1200}H_{200}$ evolve over time. Initially only the precursor $C_{12}H_2$ is present in this case[6]. The $C_{12}H_2$ density clearly decreases during the entire simulation and more than 99.9% of the initial $C_{12}H_2$ particles are lost after $t = 0.1\,\text{s}$. It is clear from figure 5.3 that coagulation happens at the millisecond time scale which is several orders of magnitude larger than the time scale at which nucleation occurs which is nanoseconds to microseconds, as was illustrated in figure 5.1. At $t = 0.1\,\text{ms}$, $C_{120}H_{20}$ starts forming and this growth phase takes until about $t = 10\,\text{ms}$, after which it peaks and decreases due to growth of even larger species. $C_{1200}H_{200}$ starts growing at approximately $t = 10\,\text{ms}$. As time passes most of the particles end up in $C_{1200}H_{200}$. If all the mass would end up in $C_{1200}H_{200}$, the final density should be two orders of magnitude lower than the initial $C_{12}H_2$ density because the volume has increased by the same amount. This is not yet the case however because the final density of $C_{1200}H_{200}$ is still below 10^{15}m^{-3}, whilst it would be 10^{16}m^{-3} if all the mass in the system was turned into $C_{1200}H_{200}$. This would never happen in this simulation however, since some mass will remain in species smaller than $C_{1200}H_{200}$ because growth stops in this model when all particles smaller than $C_{612}H_{102}$ (particle 51) have disappeared, since no more reactions satisfy $i + j \leq 100$ as explained in section 5.3. Finally, it has been verified that the total mass remains constant during the simulation since no production or destruction is taken into account.

5.3.2 Case 2: Coagulation for linearly growing particles $C_{12}H_2$ up to $C_{1200}H_{200}$ with production of $C_{12}H_2$

In a real plasma, we expect to have a source of $C_{12}H_2$ from the plasma chemistry, the strength of which depends on the plasma conditions. This implies that case 1, where there is just a basin of initial $C_{12}H_2$, is not very realistic. The net rate at which $C_{12}H_2$ is produced by the plasma can be estimated using the nucleation model and was calculated by adding the rates of reactions that produce $C_{12}H_2$ according to equation (4.6) and found to be $2.5 \times 10^{19}\,\text{m}^{-3}\text{s}^{-1}$. In this case, particles are pumped out of the plasma so that the total mass is conserved.

The density evolution of $C_{12}H_2$, $C_{120}H_{20}$ and $C_{1200}H_{200}$ is given in figure 5.4. In this case, steady state can occur,

[6]Note that $C_{12}H_2$ is only the precursor of the separate coagulation models while C_2H_2 is the actual precursor in the full model which contains the plasma chemistry as well as coagulation

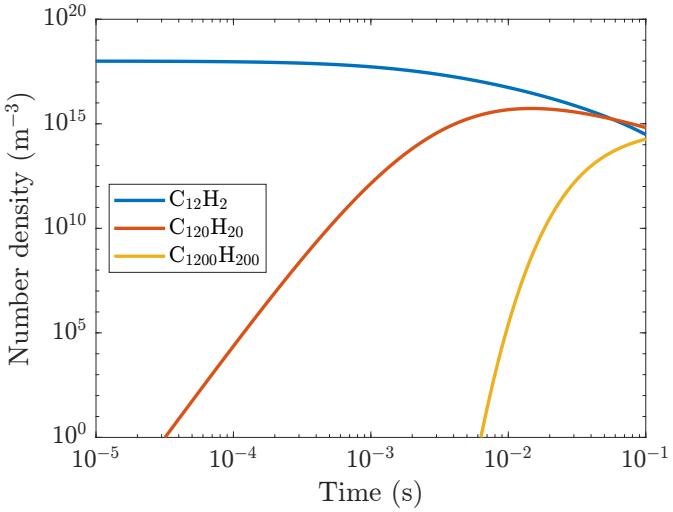

Figure 5.3: The time evolution of the densities of $C_{12}H_2$, $C_{120}H_{20}$ and $C_{1200}H_{200}$ in absence of a $C_{12}H_2$ source.

since there is a production and a loss term. It is clear that steady state is almost reached at $t = 100\,\text{ms}$ for $C_{12}H_2$ and $C_{120}H_{20}$, because the densities are nearly constant at this point in time. As expected, the inflow of $C_{12}H_2$ leads to higher densities of the smaller particles, while the densities of particles at the larger end of the particle spectrum decrease, since they are now lost due removal by means of pumping. Furthermore, it can be seen that the evolution of $C_{120}H_{20}$ is almost independent of the production term up to $t = 10\,\text{ms}$, which can be seen from comparing figures 5.3 and 5.4. This can be explained from the fact that this production term is so small, such that it has no impact at these time scales. The impact of the production term on the results is related to the integrated production which becomes significant after $t = 10\,\text{ms}$, where the results between figures 5.3 and 5.4 deviates.

The advantage of a linear species set is the high resolution and the fact that it gives knowledge about a lot of species. It is computationally very expensive however, even though it only covers a relatively small volume and size domain. It is therefore interesting to analyse how these results compare to an exponentially growing species set, which we will do in the next section.

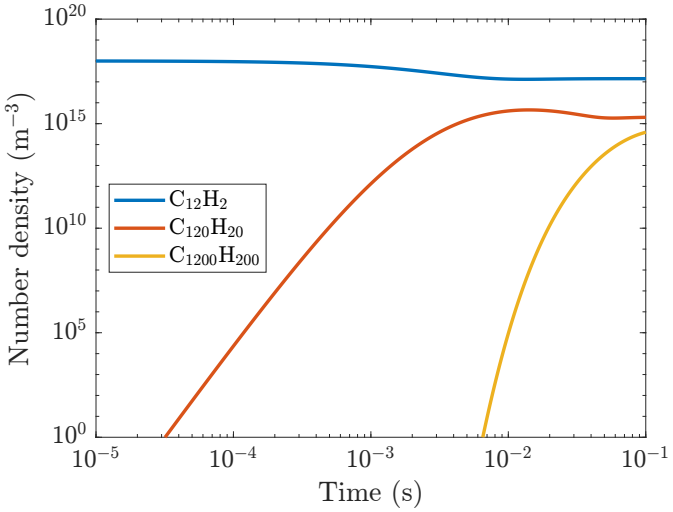

Figure 5.4: The time evolution of the densities of $C_{12}H_2$, $C_{120}H_{20}$ and $C_{1200}H_{200}$ with a $C_{12}H_2$ source.

5.3.3 Case 3: Coagulation for exponentially growing particle $C_{12}H_2$ up to $C_{1536}H_{256}$

In this case, we explore the possibility of simulating coagulation using a species set with exponentially growing species as well as production of $C_{12}H_2$ equivalent to case 2. The temporal density evolution of $C_{12}H_2$, $C_{96}H_{16}$ and $C_{1536}H_{256}$ are plotted in figure 5.5. The growth processes in the exponential set are clearly faster than the processes in the linear set. It should be stressed however that the two models cannot be compared directly, since the bins in the case exponential particle set case represent a wider volume range, since the same volume range is covered with 8 bins instead of 100.

The growth of species shows a similar trend in both models. The density of the smallest species $C_{12}H_2$ decreases about two orders of magnitude in 10 ms with exponential binning, while it decreases by a single order of magnitude by using linear binning. $C_{96}H_{16}$ has already reached a density of $10^9 m^{-3}$ at $t = 10^{-2}$ms in the exponential set, whilst this this density is reached at $t = 1$ ms for the related particle $C_{120}H_{20}$ using the linear particle set. We observe the same pattern for the other species.

The fact that according to the model, growth of $C_{1536}H_{256}$ from $C_{12}H_2$ happens faster than growth of $C_{12}H_2$ from C_2H_2 in the plasma chemistry, as was shown in figure 5.1d, is very remarkable. It seems like the model breaks down at $t \approx 100$ ms with a sudden crash by more than 5 orders of magnitude of the $C_{96}H_{16}$ density. Furthermore, it is easily shown that the total final mass of the system is more than the sum of the initial mass and the produced mass in this time period, which violates mass conservation. We will show this by calculating the total available $C_{12}H_2$ during the simulation:

$$n_{tot} = n_{initial} + PT = 10^{18} + 2.5 \times 10^{19} 0.1 = 3.5 \times 10^{19}\,\mathrm{m}^{-3}, \tag{5.1}$$

with P the $C_{12}H_2$ production which was discussed to be equal to $3.5 \times 10^{19}\,\mathrm{m}^{-3}\mathrm{s}^{-1}$ and T the simulation time. $C_{1536}H_{256}$ however is 128 times larger than $C_{12}H_2$ so its maximum density can be of the order $10^{17} m^{-3}$ which it clearly violates. This is probably caused by numerical problems that follow from the discretisation choice. PLASIMO only accepts species made out of an integer multiple of C and H such that the exponential set could only be implemented using integer growth factors. This means that the smallest meaningful possibility for the growth factor was $g = 2$. De Bleecker et al. use a volume growth factor of approximately 1.15 however, so it is plausible that the growth factor of two is simply too large [25]. The real growth process consists of an almost continuous volume space, so it is intuitive that the linear set containing 100 particles over the volume range is a far better approximation and produces more realistic results compared to the exponential binning with 8 particles. We will therefore only continue with linear binning from now on.

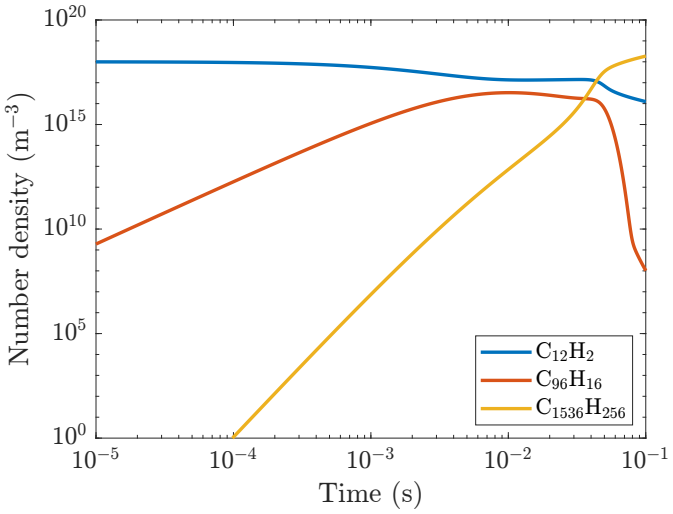

Figure 5.5: The time evolution of the densities of $C_{12}H_2$, $C_{96}H_{16}$ and $C_{1536}H_{256}$ with a $C_{12}H_2$ source.

5.3.4 Conclusions from case 1, case 2 and case 3

We have so far seen three different coagulation models starting with $C_{12}H_2$. We have seen in case 1 that a reservoir of $C_{12}H_2$ empties for 99.9% in 100 ms, if it is not replenished. If we wait long enough, all the species smaller than $C_{600}H_{100}$ would disappear. We have seen in case 2 that a steady state forms if $C_{12}H_2$ is replenished at a representative rate taken identical to the $C_{12}H_2$ production rate from the plasma chemistry discussed in section 5.2. In the steady state, the $C_{12}H_2$ density drops by an order of magnitude from the beginning value and $C_{120}H_{20}$ reaches a density higher than 10^{15} m^{-3}. $C_{1200}H_{200}$ does not reach a steady state value within 100 ms. In case 3 we explored the possibility of exponential binning which could theoretically be used to simulate a larger volume range, but this method has been rejected for the purposes of this thesis, since the growth factor cannot be chosen sufficiently small.

Figure 5.6 shows the particle size distribution at $t = 10$ ms and $t = 100$ ms as a function of the radius without production of $C_{12}H_2$ (case 1) and with production of $C_{12}H_2$ (case 2). First of all, there is a very large difference between the size distribution at $t = 10$ ms and $t = 100$ ms, since the density of the largest species such as $C_{1200}H_{200}$ grows by more than eight orders of magnitude in this time period. This proves that the typical timescale for coagulation is in the millisecond range. Furthermore, the production term has a far greater impact at $t = 100$ ms than at $t = 10$ ms which is understandable from the fact that what matters is the integrated mass of particles produced, which increases linearly with time. Finally, it should be noted that the particle size distribution shifts to the right, the largest particles become dominant in the plasma, if $C_{12}H_2$ is not replenished, whilst a steady state distribution forms where the smaller and larger particles are in equilibrium if $C_{12}H_2$ is replenished.

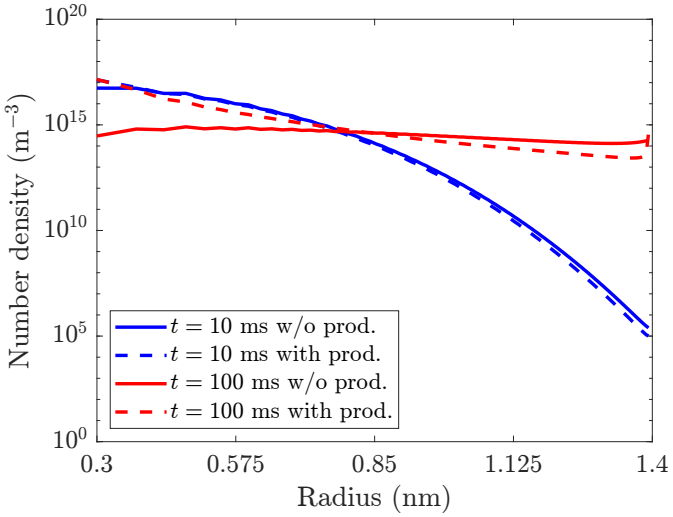

Figure 5.6: Particle size distribution after $t = 10$ ms (blue) and $t = 100$ ms (red) for species $C_{12i}H_{2i}$ with $i \in [1, 100]$ without production of $C_{12}H_2$ (case 1, solid lines) and with production of $C_{12}H_2$ (case 2, dashed lines).

5.3.5 Nucleation and coagulation simultaneously

The main challenge of simulating the full global model combining the nucleation and coagulation models is the different time scales involved with these processes. We have seen in section 5.2 that the time scale for the nucleation phase is in the order of nanoseconds or microseconds, whilst we saw in section 5.3.1 that the relevant time scale for coagulation is in the order of milliseconds. It is unfortunately not possible in the current PLASIMO infrastructure to choose different time scales for different processes, which means that we are required to run a simulation with millions of iterations, in order to capture both nucleation and coagulation in a single model. We will come back to this in section 7.2.

In this model we use a linear species set for coagulation consisting the species $C_{12i}H_{2i}$ for $i \in [1, 100]$. The key outputs analogous to the figure 5.1 of nucleation model in section 5.2 are given in appendix D.1. Since the results are nearly identical, the relative difference is given for the species with the largest relative difference defined as $\left|\frac{n_{nucl}-n_{coag}}{n_{coag}}\right|$ at $t = 100\,\text{ms}$ in figure 5.7. $C_{12}H_2$ has the largest relative difference of about 8, followed by $C_{12}H$ with a relative difference of about 60%. CH^+ has the third largest relative difference with a negligible less than 0.1%, which is clearly just noise. It makes sense that $C_{12}H_2$ is impacted the most by the coagulation phase, since it is the only species in the plasma chemistry that participates in coagulation. $C_{12}H$ is also significantly impacted since it is directly created from $C_{12}H_2$ by electron impact reaction 15 and involved with the creation of $C_{12}H_2$ by molecule-molecule reaction 10, both given in appendix A.2. Furthermore, we had already concluded from section 5.3.1 and section 5.3.2 that coagulation takes place at time scales larger than a millisecond, which can also be observed in figure 5.7, where drifts start to occur at $t = 1\,\text{ms}$.

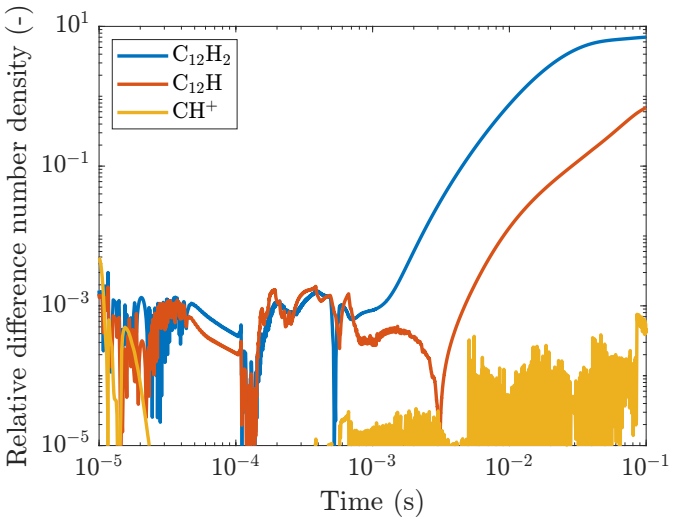

Figure 5.7: The relative difference of the number density between simulations with and without coagulation as a function of time, for the species with the largest difference at $t = 100\,\text{ms}$.

Figure 5.8 shows the species containing 12 carbon atoms analogous to figure 5.1d. It shows once again that the only density that deviates significantly from the simulation of only nucleation is that of $C_{12}H_2$ starting around 1 ms, the time-scale of coagulation as expected. It can also be observed by comparing figures 5.1d and 5.8 that the difference of the final $C_{12}H_2$ density is indeed about a factor 8. Furthermore, $C_{12}H_6$ and $C_{12}H^-$ have now a higher and similar density compared to $C_{12}H_2$, which implies that these species will also be important species for coagulation and they should be taken into account. Finally, figure 5.9a shows the densities of $C_{12}H_2$, $C_{120}H_{20}$ and $C_{1200}H_{200}$ as a function of time and figure 5.9b shows the particle size distribution at $t = 10\,\text{ms}$ and $T = 100\,\text{ms}$. The density of $C_{12}H_2$ shows very different behaviour in this case with nucleation compared the simulation without nucleation shown in figure 5.4 for obvious reasons, since the initial $C_{12}H_2$ density is zero in this case. At around $t = 10\,\text{ms}$ however, the behaviour is very similar. The same pattern is observed for $C_{120}H_{20}$ and $C_{1200}H_{200}$, where the behaviour is very similar in structure but slower which makes sense. These species are eventually made from $C_{12}H_2$. If $C_{12}H_2$ forms later, so will these larger species. The particle size distribution from figure 5.9b is very different compared to the case without nucleation shown by figure 5.6 at $t = 10\,\text{ms}$ but remarkably similar at $t = 100\,\text{ms}$, which can once again be explained with the same arguments as before.

As species get larger, they tend to charge negatively as was explained in section 2.6.2. The charging of these particles will be explored in the next section.

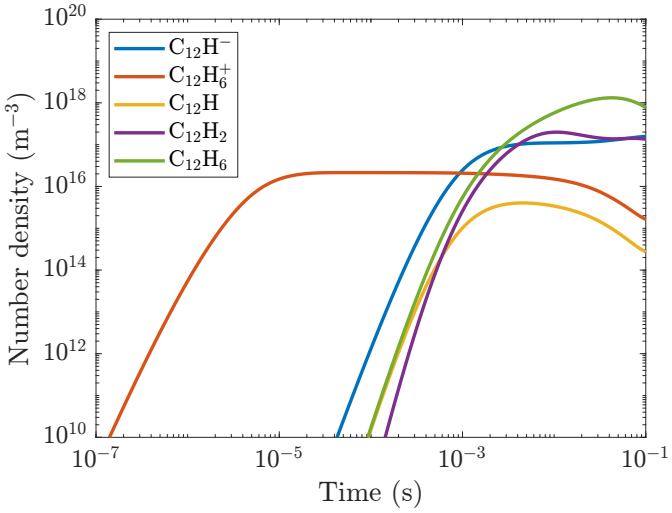

Figure 5.8: The densities of species containing 12 carbon atoms as a function of time.

Figure 5.9: Densities of $C_{12}H_2$, $C_{120}H_{20}$ and $C_{1200}H_{200}$ as a function of time and the particle size distribution at $t = 10\,\text{ms}$ and $t = 100\,\text{ms}$. the coagulation phase for the species $C_{12n}H_{2n}$ for $n \in [1, 100]$.

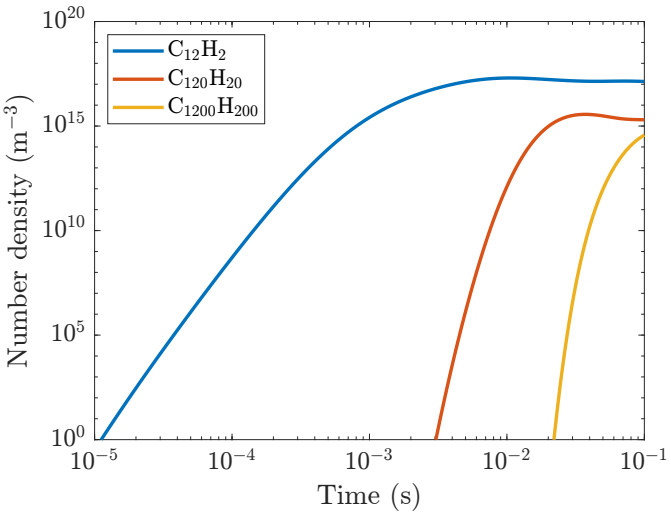

(a) Number densities of $C_{12}H_2$, $C_{120}H_{20}$ and $C_{1200}H_{200}$ as a function of time.

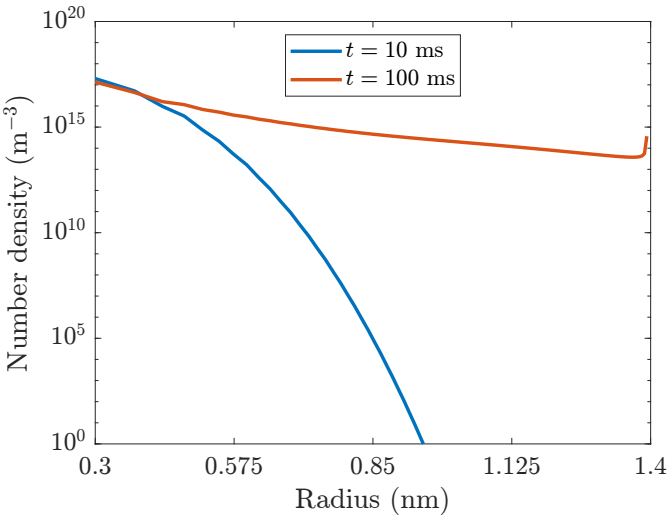

(b) Particle size distribution at $t = 10\,\text{ms}$ and $t = 100\,\text{ms}$.

5.4 Coagulation with charging of nanoparticles

In the simulations done so far, no charging of nanoparticles has been taken into account, even though we have seen in section 2.6.2 that, under typical plasma conditions, dust particles tend to charge negatively. As shown in figure 5.1 the electron and ion densities, as well as the electron temperature are almost constant in the nucleation model at $t = 1\,\text{ms}$. As long as that is the case, the floating electron and ion currents given by equation (2.26) and equation (2.27) can be set equal to calculate the floating potential. The particle charge is consequently found using equation (2.28):

The floating potential is found using $\hat{T}_e = 2.8\,\text{eV}$, $T_i = 400\,\text{K}$, $n_e = 2 \times 10^{16}\,\text{m}^{-3}$ and $n_{i+} = 3 \times 10^{16}\,\text{m}^{-3}$ as found section 5.3.5. Using these values, it is possible to define the reactions and particles taking account the charges before a simulation, which can consequently be used to simulate coagulation for a domain where the number of electrons lost in charges is a fraction of the total number of electrons. Using the floating current and equation (2.28), we find that a nanoparticle with a radius of 0.3 nm has on average one electron. Since the particle charge scales linearly with the radius, a nanoparticle with a radius of 0.6 nm has on average two electrons and so on. We have seen in section 5.3 that $C_{12}H_2$ has a radius of approximately 0.3 nm, but this particle will remain neutral in order to keep the plasma chemistry untouched. $C_{24}H_4^{(-)}$ and larger particles will therefore carry an expected charge of $-e$, $C_{108}H_{18}^{(-2)}$ and larger particles carry an expected charge of $-2e$, $C_{336}H_{56}^{(-3)}$ and larger particles carry and expected charge of $-3e$ and $C_{780}H_{130}^{(-4)}$ and larger particles carry an expected charge of $-4e$. The charge of these species is given in parentheses because it is an expected OML charge and not an ionic charge. it was explained in section 4.2 that charging is a stochastic process and these charges are therefore uncertain in nature. We assume for simplicity however that all nanoparticles carry their expected charge.

Since $C_{12}H_2$ is the only neutral species in this model, using the repulsion correction term of equation (2.27) implies that coagulation only happens using combinations involving $C_{12}H_2$ and another dust particle.

In section 5.4.1, coagulation will be modelled separately under the assumption that the charge has no significant effect on the interactions using equation (2.30), as well as under the assumption that two negatively charged particles will not be able to coagulate together using the extension described in equation (2.31). Nucleation and coagulation are simulated simultaneously taking into account the electrons lost to dust particles in section 5.4.2. It should be stressed however that this process can only be simulated as long as n_e and $\hat{T}_e$ remain approximately constant.

5.4.1 Coagulation with charging

In this section, we will repeat the simulations of the coagulation phase performed in section 5.3.1 taking charging into account. This means that we start once again with $C_{12}H_2$ with a density of 10^{18} m^{-3}, as well as an electron density of $2 \times 10^{16}\,\text{m}^{-3}$, neither of which have a source term.

Figure 5.10 shows the electron and $C_{24}H_4^{(-)}$ density as a function of time for the cases with and without the repulsive correction term given by equation (2.26). The electron density has already decreased by a factor of 2 at $t \approx 3 \times 10^{-2}\,\text{ms}$. At this point, the densities of electrons and $C_{24}H_4^{(-)}$ are approximately equal to half the initial electron density. This suggests that it is $C_{24}H_4^{(-)}$ that consumes the majority of the lost electrons. Since the formation of $C_{24}H_4^{(-)}$ is identical for the cases with and without the charging correction to the coagulation frequency, both models give the same result. The fact that the initial $C_{12}H_2$ density is more than an order of magnitude higher than the electron density explains that there will at some point be more dust particles than electrons. Considering that every dust particle consumes at least one electron, it is to be expected that the electron density will decrease sharply. This implies that the assumption that the electron density remains approximately constant is not valid, if there is no electron source.

In reality however, electrons are formed by the plasma. It is therefore interesting to see what happens if these coagulation with charging cases are connected to the nucleation model described in section 5.2. We will do this in the next section.

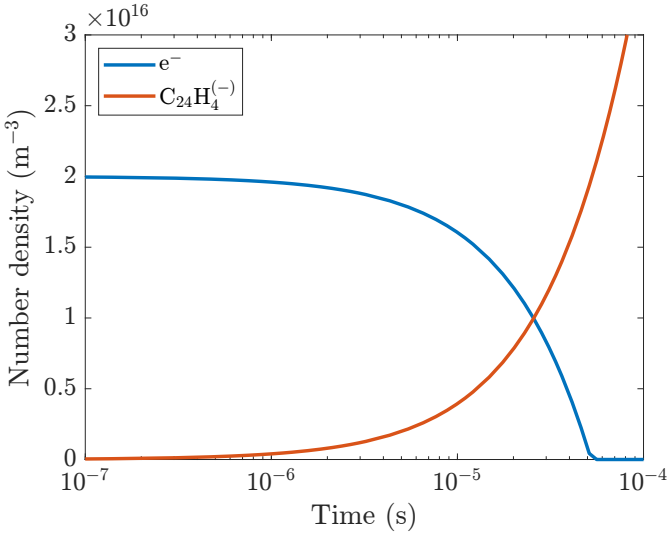

Figure 5.10: Densities of e^- and $C_{24}H_4^{(-)}$ as a function of time.

5.4.2 Nucleation and coagulation with repulsion

It is now time to combine the new coagulation models with the nucleation model. This is done by combining the nucleation model from section 5.2 with the coagulation model with charging from section 5.4.1, using the repulsion factor between two charged particles given by equation (2.31).

The particle size distribution is given by figure 5.11a and the relative electron densities are given by figure 5.11b. Two things can immediately be observed from the particle size distribution. The first is that coagulation takes place at relatively long timescales since most species start to grow between $t = 10\,\text{ms}$ and $t = 100\,\text{ms}$. Furthermore, the largest species up to $r = 1.4\,\text{nm}$ only grow within the first 100 ms if the repulsive force between these particles is neglected. The shape of the distribution at $t = 100\,\text{ms}$ where repulsion is ignored is very similar to the shape at $t = 100\,\text{ms}$ with $C_{12}H_2$ production where the charging of nanoparticles was ignored in figure 5.6. This follows logically from the fact that the coagulation frequencies are identical if the repulsive force is neglected and that the $C_{12}H_2$ production term in figure 5.6 was chosen to be similar to the real calculated formation rate in the plasma.

It has been explained before that the charging model is based on the assumption that the electron density is relatively constant. We have already seen in figure 5.1 that the electron density becomes constant if coagulation is not taken into account. Figure 5.11b shows the relative difference in the electron density as a function of time for three cases: charging with the repulsive force (1), charging without the repulsive force (2) and no charging (3). The blue line gives the relative difference: $\left|\frac{n_{e,1}-n_{e,2}}{n_{e,1}}\right|$ (comparison 1), the red line gives the relative difference: $\left|\frac{n_{e,1}-n_{e,3}}{n_{e,1}}\right|$ (comparison 2) and the yellow line gives the relative difference: $\left|\frac{n_{e,2}-n_{e,3}}{n_{e,2}}\right|$ (comparison 3). The relative difference remains below 0.1% for all three comparisons, which means that the electron density is hardly impacted by charging of nanoparticles in these simulations. Until $t \approx 1\,\text{ms}$, all three relative differences follow a random noise path and remain below 10^{-5}. The two relative differences between the cases with charging and without coagulation (comparison 2 and comparison 3) start to increase after $t = 1\,\text{ms}$, which is the moment where $C_{24}H_2^{(-)}$ starts to form so that electrons are consumed similarly for the charging cases, and not consumed for the case without charging. At $t \approx 10\,\text{ms}$, the cases where coagulation is taken into account start to diverge, since larger species than $C_{24}H_4^{(-)}$ are formed and the repulsive term becomes relevant. In the case without the repulsive force, reactions between dust particles carrying a charge $-e$ return electrons to the plasma. An example of such a reaction is:

$$C_{24}H_4^{(-)} + C_{24}H_4^{(-)} \rightarrow C_{48}H_8^{(-)} + e^-. \tag{5.2}$$

At $t \approx 30\,\text{ms}$, a significant percentage of the electrons consumed by $C_{24}H_4^{(-)}$ are returned to the plasma, such that the relative difference drops back to the case where charging is not taken into account. This process would likely reverse once more once a significant number of dust particles carrying a charge $-2e$ start to form. We have seen in section 5.4 that the smallest particle carrying a charge of $-2e$ is $C_{336}H_{56}^{(2-)}$ which has a radius of approximately 0.9 nm. It can be seen in figure 5.11a that the density of this species remains more than two orders of magnitude below those of the smallest species carrying a charge of $-e$ which is why charging of particles to $-2e$ is not observed yet in the relative difference.

Figure 5.11: The size distribution of dust particles at $t = 10\,\text{ms}$ and $t = 100\,\text{ms}$ for the species $C_{12n}H_{2n}$ with and without repulsion, as well as the relative difference in electron density for the cases without coagulation, with coagulation without repulsion and with coagulation with repulsion.

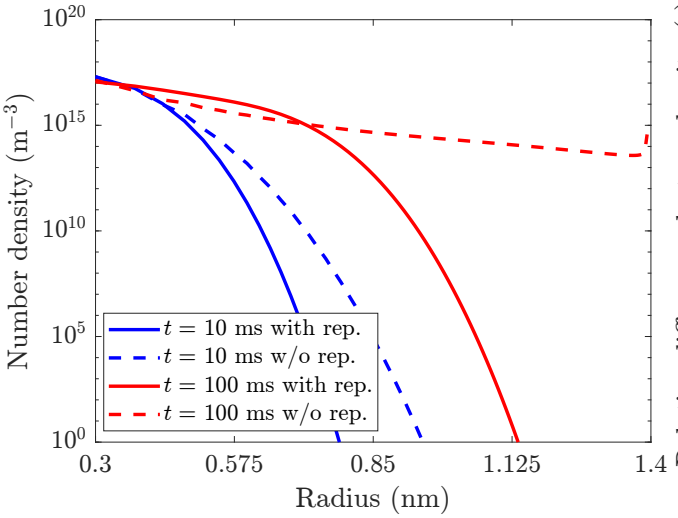

(a) The size distribution of dust particles at $t = 10\,\text{ms}$ and $t = 100\,\text{ms}$ for the species $C_{12n}H_{2n}$. Repulsion has been indicated by 'rep.'.

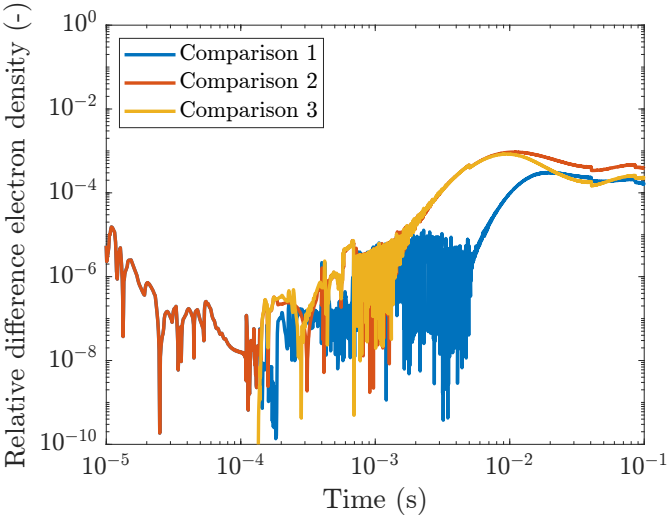

(b) The relative difference in electron density for the cases without coagulation, with coagulation without repulsion and with coagulation with repulsion.

Figure 5.11b shows that the impact of charging of nanoparticles on the electron density is less than 0.1%. We can therefore conclude that the assumption that the electron density remains approximately constant is correct. The electron temperature is only impacted via the change of the electron density. Since the electron density remains approximately constant, so does the electron temperature. Furthermore, ions do not play a part in coagulation in our simulations and the gas temperature is fixed. This means that the assumption that n_e, n_{i+}, T_e and T_i remain approximately constant is valid.

5.5 Accuracy

The simulations performed in the global model are completely deterministic, so if a simulation is repeated with the same initial conditions and simulation parameters, the output will be identical. In this section we will explore what happens to the output if we vary the tolerance and the initial conditions of the simulations. We will compare the results of the first 10 ms of nucleation simulation in section 5.2 with the same simulation with absolute and relative tolerances set at 10^{-5} instead of 10^{-4} and with the same simulation with the initial electron and $C_2H_2^+$ densities set at 10^{15}m^{-3} instead of 10^{16}m^{-3}.

5.5.1 Impact of a lower solver tolerance

It was stated in section 4.3.3 that the absolute and relative tolerance used in the global model simulations was 10^{-4}. In this section we will observe what happens to the electron and $C_2H_2^+$ densities if we use a smaller tolerance of 10^{-5}. The relative difference given by: $\left|\frac{n_1-n_2}{n_1}\right|$, with n_1 the density with a tolerance of 10^{-4} and n_2 the density with a tolerance of 10^{-5} is given by figure 5.12. We can draw two important conclusions from the figure: the relative density difference of both species remains below 0.1% and the relative density difference shows a noisy path in time without drift. This absence of drift is important since it implies that numerical errors do not accumulate over time. The absence of drift allows us to make the presumption that the numerical errors remain in the order of 10^{-3} or smaller even for longer simulation times.

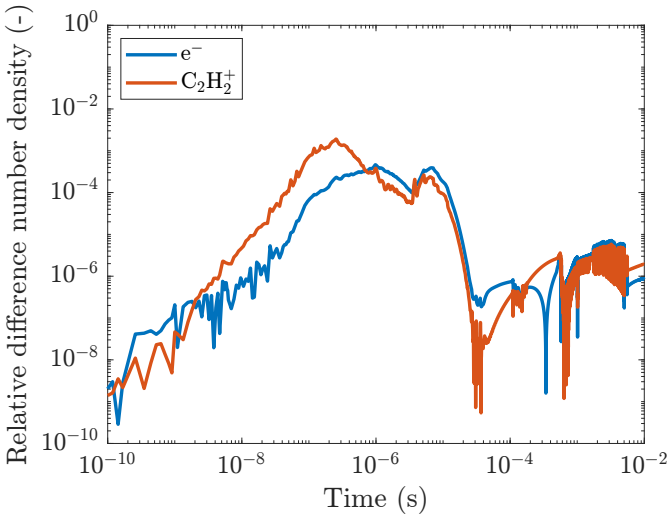

Figure 5.12: Relative density difference using a tolerance of 10^{-4} and a tolerance of 10^{-5} for electrons and $C_2H_2^+$ in time.

5.5.2 Impact of different initial conditions

In this section, we explore the impact of the initial densities on the results of the simulation. This was done by using the relative differences in time calculated using $\left|\frac{n_1-n_2}{n_1}\right|$, with n_1 the density path identical to what was found in section 5.2 using initial electron and $C_2H_2^+$ densities of $10^{16}m^{-3}$, while n_2 describes a density path with an initial electron and $C_2H_2^+$ density of $10^{15}m^{-3}$ instead. Figure 5.13 shows these relative density difference as a function of time. The relative density difference is 90% initially, since the new densities are only 10% of the old densities. In time however, the relative density differences decrease to 10^{-3} where they stabilise for both electrons and $C_2H_2^+$. This implies that the results of the simulations are not strongly dependent on the initial conditions.

5.5.3 Accuracy tests conclusions

In this section, we have tested the impact of varying the solver tolerance and initial densities of the simulations in the global model. We have seen that a lower tolerance does not lead to significant deviations in the results, since the relative density differences remain below 0.1%. This means that the used tolerance of 10^{-4} was appropriate.

We have also seen that the simulated densities converge to the same value, for different initial densities. This implies that the model outcomes do not strongly dependent on the initial conditions. These observations should give genuine credibility to the simulations.

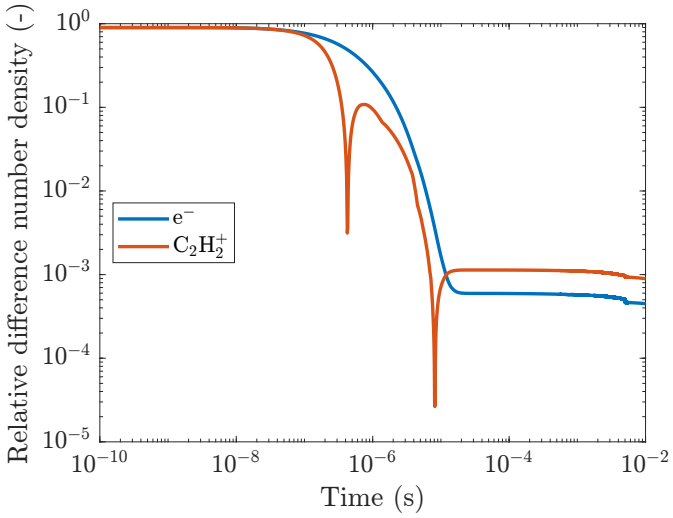

Figure 5.13: Relative density difference using a initial densities of $10^{16}\mathrm{m}^{-3}$ and $10^{15}\mathrm{m}^{-3}$ for electrons and $C_2H_2^+$ in time.

6 Results 1D drift-diffusion simulation

The 1D drift-diffusion simulation that we will discuss in this section simulates a plasma with similar initial conditions and model parameters as was discussed in section 5.1. The difference with the global model is that the continuity equation (2.5) will be solved on a spatial grid. Transport will be taken into account since spatial derivatives no longer vanish. Diffusion coefficients are calculated using collision integrals given by equation (2.18). Mobilities are consequently calculated using the Einstein equation (2.13) for charged particles. The EEDF will be solved in space by BOLSIG+. Furthermore, the wall reactions are simulated more realistically by using a similar sticking model but by using the real local flux densities towards the walls.

In this section we will discuss how the plasma chemistry changes if spatial effects are taken into account, by comparing the results to those of the nucleation phase discussed in section 5.2. We will use this to predict how spatial dependencies could influence coagulation and whether it is important to take these spatial dependencies into account.

6.1 Plasma chemistry

Figure 6.1 shows the spatially averaged neutral species, negative species, radicals and species containing 12 carbon atoms analogous to figure 5.1. The 1D simulation has an end time of $t = 5\,\text{ms}$, since longer simulations up to 100 ms, analogous to the global model were not computationally viable. The electron temperature is given in figure 6.2 has a data-point every microsecond, while the species densities from figure 5.1 have variable spacing between data-points depending on the time-step of the simulation. The periodic behaviour that is observed in the electron temperature can be explained by the effect of the RF-electrode on the electron temperature is now spatially resolved. The average temperature however, quickly moves towards about 2.3 eV, which is comparable to the electron temperature found in the global model of about 2.5 eV at time $0.1\,\text{ms} < t < 5\,\text{ms}$. The neutral molecules C_4H_2, $C_{12}H_2$ and H_2 show similar behaviour to the results from the global model given in figure 5.1. C_4H_2 for example reaches a number density of 10^{10}m^{-3} at $t \approx 10^{-9}\text{s}$ both in the global and 1D simulation. $C_{12}H_2$ however already reaches a density of 10^{15}m^{-3} at $t = 1\,\text{ms}$ in the global model, while it only reaches a density of only 10^{11}m^{-3} in the 1D model at the same point in time. A final key observation is that the electron density reaches a value of 10^{15}m^{-3} in the 1D model, which is more than an order of magnitude smaller in the global model. This could change the coagulation dynamics significantly since this strongly depends on the electron density as discussed in section 2.6.2.

Figure 6.1d shows the number density of the species containing 12 carbon atoms as a function of time, analogous to figure 5.1d from the global model. $C_{12}H_6^+$ is the fastest to form, already reaching a density of about 10^{10}m^{-3} at $t = 1 \times 10^{-7}\,\text{s}$ similar to the global model. The other species containing 12 carbon atoms however form slower than was suggested by the global model. These species have densities of about 10^{10}m^{-3} at $t = 1\,\text{ms}$, at which point they already had densities surpassing 10^{15}m^{-3} in the global model. This suggests that the coagulation phase might start later than the global model showed. From the species containing 12 carbon atoms in the 1D model, it would make more sense to start with $C_{12}H_6^+$ as the initial species for coagulation. Figure 6.1d does not tell the whole story however, since it does not show what happens at larger timescales. $C_{12}H_6^+$ also had the highest number density in the global model initially, but the other species containing 12 carbon atoms eventually caught up there. It is hard to predict whether we would see the same pattern in the 1D model, without running longer simulations.

The results of the global model show similar trends to the results of the 1D model for most important species. It should however be stressed that the global model remains an approximation and almost all real observables in the plasma such as the densities and temperature will be spatially dependent. This fact is shown in figures 6.3, 6.4 and 6.5, which show the number density of electrons, $C_2H_2^+$ and $C_{12}H_2$ as a function of space and time and the distribution in space at $t = 5\,\text{ms}$. The ten microseconds shown in these figures are the final 10 microseconds before $t = 5\,\text{ms}$. It is clear that there is a strong spatial (vertical) dependency in each of the species densities. Furthermore, we observe that electrons and $C_{12}H_2$ have the highest number density around the middle of the discharge, while the positive $C_2H_2^+$ has the highest number density outside the centre of the discharge. This can be explained by the positive plasma potential with respect to the plasma edge as was explained by section 2.2.2. Finally, the charged electrons and $C_2H_2^+$ particles show a weak spatial dependence, since they can feel the oscillating applied electric field, while this spatial dependence is negligible for the neutral $C_{12}H_2$ particles.

Figure 6.1: Key outputs of the 1D of the plasma chemistry. (a) Shows the electron temperature, (b) the densities of some gas species, (c) shows the densities of some negative ions and electrons and (d) shows the densities of some radicals as a function of time.

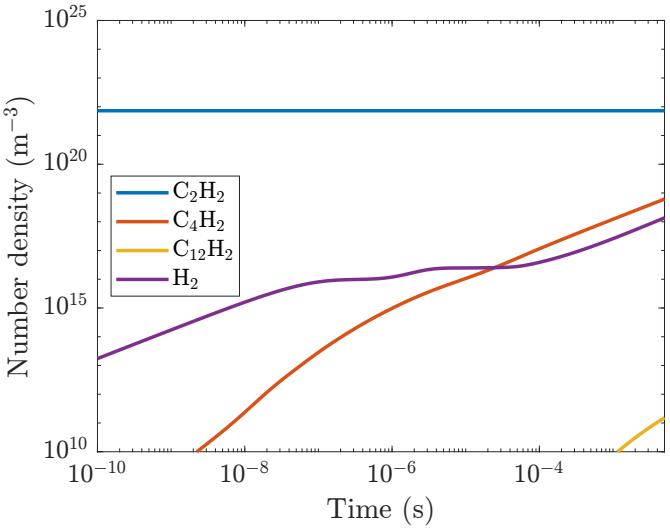

(a) Space averaged number densities for gas species as a function of time.

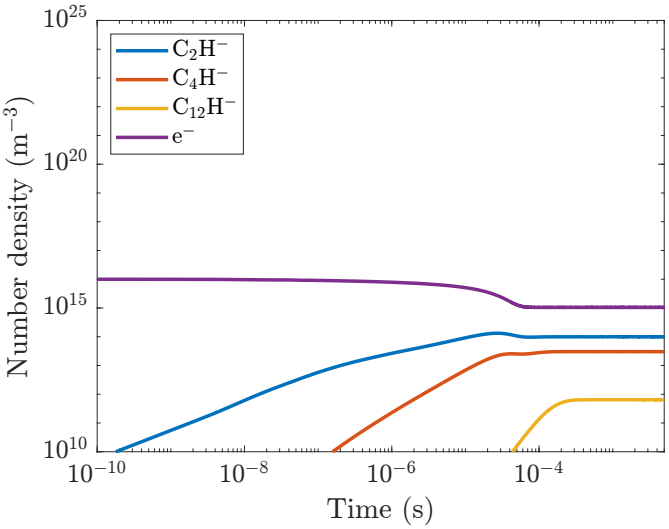

(b) Space averaged number densities for negative ions as a function of time.

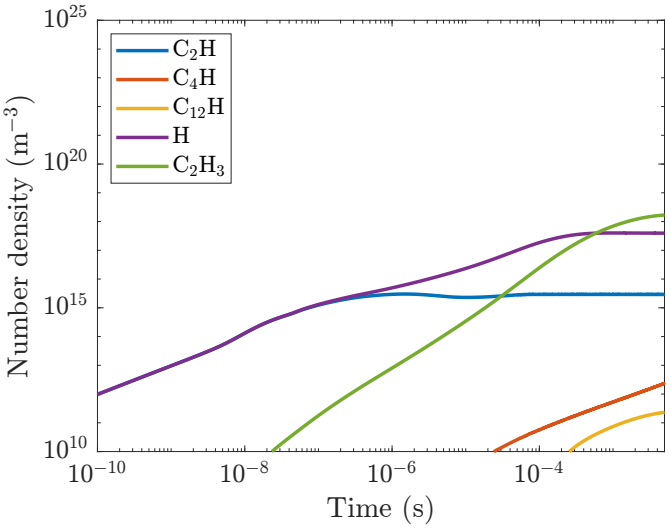

(c) Space averaged number densities for radicals as a function of time.

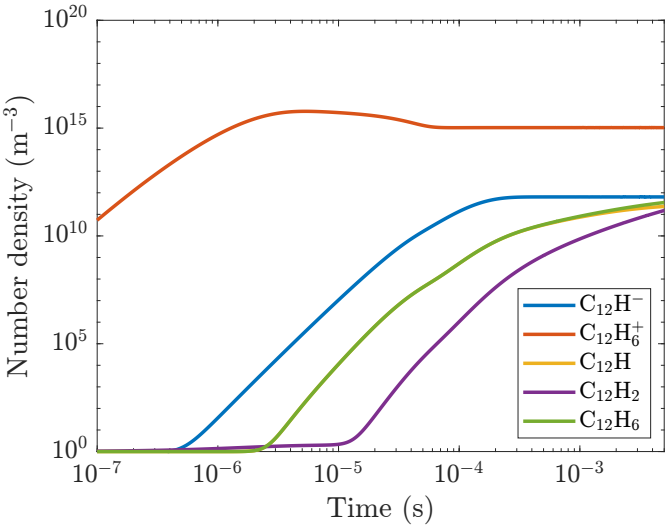

(d) Space averaged number densities for species containing 12 carbon atoms as a function of time.

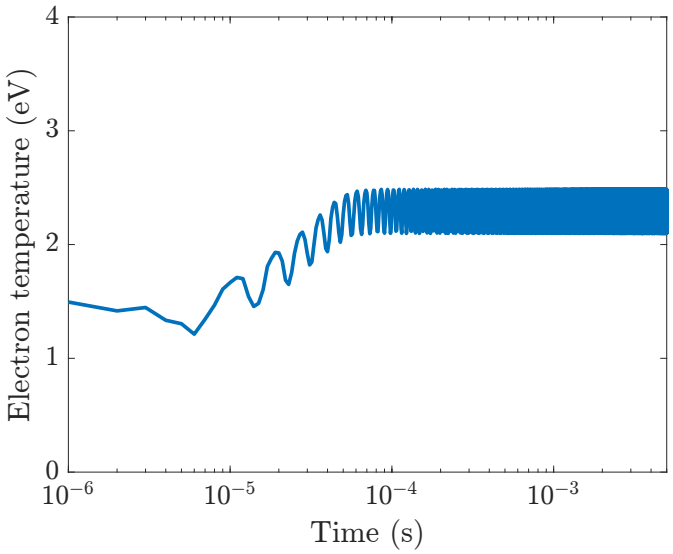

Figure 6.2: Space averaged electron temperature as a function of time.

Figure 6.3: Electron distribution in space and time.

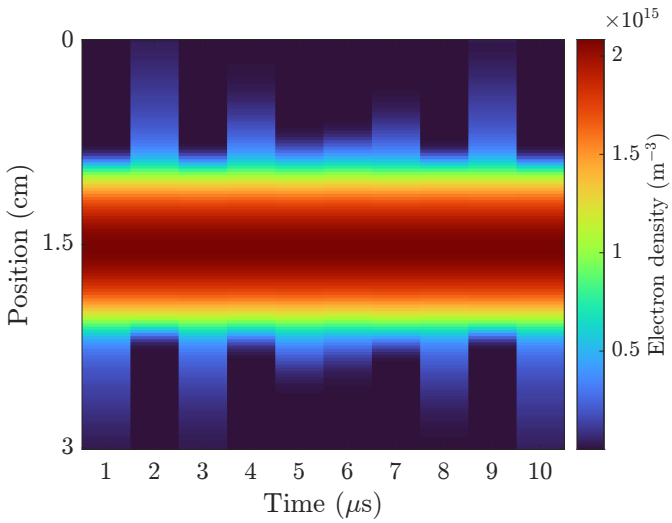

(a) The density of electrons as a function of space and time. Note that the vertical axis does not scale linearly with the position but with the grid point density so it is squeezed towards the centre.

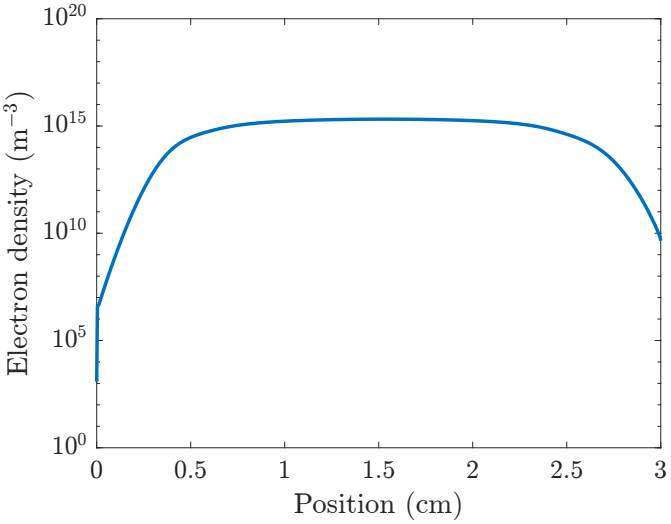

(b) Electron density as a function of space at a fixed point in time at $t = 5\,\mathrm{ms}$.

Figure 6.4: The density of $C_2H_2^+$ as a function of space and time.

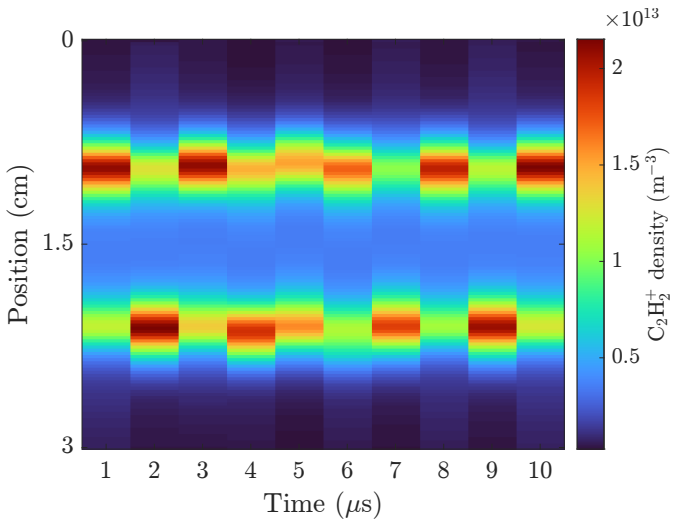

(a) The density of $C_2H_2^+$ as a function of space and time. Note that the vertical axis does not scale linearly with the position but with the grid point density so it is squeezed towards the centre.

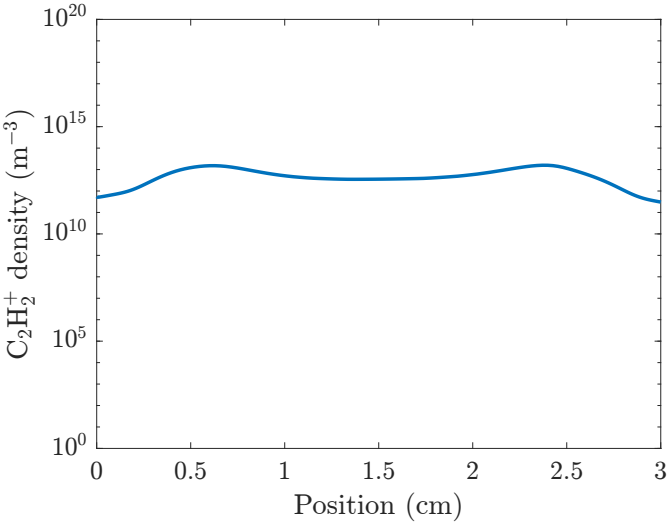

(b) The density of $C_2H_2^+$ as a function of space at a fixed point in time at $t = 5\,\text{ms}$.

Figure 6.5: The density of $C_{12}H_2$ as a function of space and time.

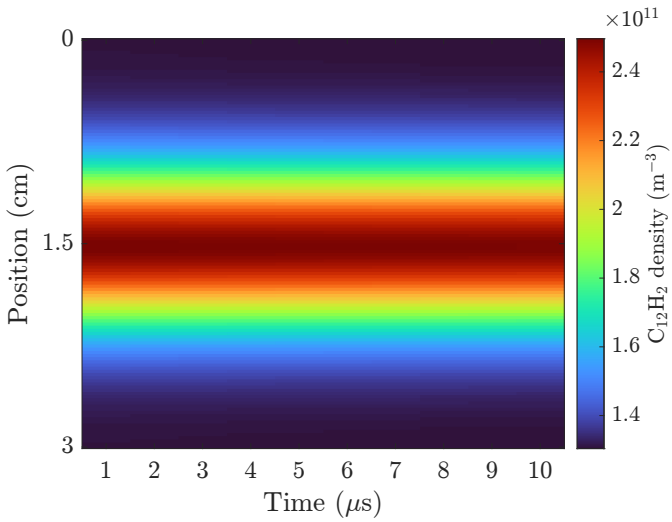

(a) The density of $C_{12}H_2$ as a function of space and time. Note that the vertical axis does not scale linearly with the position but with the grid point density so it is squeezed towards the centre.

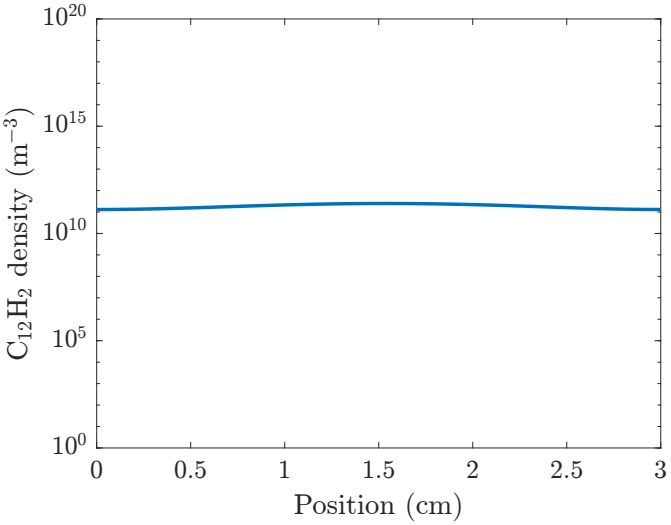

(b) The density of $C_{12}H_2$ as a function of space at a fixed point in time at $t = 5\,\text{ms}$.

7 Conclusions and outlook

7.1 Conclusions

In this thesis, we have examined the possibility of simulating the nucleation and coagulation phases of dust growth in low-pressure RF acetylene plasmas in PLASIMO. This was done by using a global model as well as a one-dimensional model. It was shown that the results of the plasma chemistry simulations are comparable to those found in literature for similar conditions.

Global model

We have seen that it is possible to simulate the nucleation phase of an acetylene plasma by means of a global model. The global model of the nucleation phase produced results that were comparable to a similar model by De Bleecker et al. [20]. For example, the density of hydrogen gas and C_4H_2 show values in the same order of magnitude and the electron temperature was almost identical compared to the findings by De Bleecker et al. The simulated electron density, however, was about an order of magnitude larger. We can therefore conclude that a global model can match the results of a one-dimensional model relatively well, but it is not a perfect match. It was not feasible to compare the largest species in the model such as $C_{12}H_2$, since steady state could not be reached for these species.

We have shown that it is possible to simulate the coagulation phase using an innovative approach, in which the species for coagulation were defined explicitly, which was a PLASIMO requirement. All species have to be specified exactly in advance of a simulation, which means that a fixed discretisation of the dust size space had to be assumed. The change in density of these discretised sizes was found using the general dynamic equation and a hard-sphere collision frequency, which could be extended using a charge dependent term in order to take the charging of nanoparticles into account. Integer multiples and exponentially growing multiples of $C_{12}H_2$ were tested, since $C_{12}H_2$ reached the highest density of the species containing 12 carbon atoms during the nucleation phase. It was shown that if only $C_{12}H_2$ is used for coagulation, $C_{12}H_6$ becomes the dominant species containing 12 carbon atoms implying that this species is also relevant for starting coagulation. Furthermore, we observed that using an exponentially growing species set does not lead to a stable simulation, since the minimum growth factor was 2, which turned out to be too large.

We have shown that coagulation could be feasibly simulated in PLASIMO for species up to 1.4 nm in radius. In reality, the coagulation phase takes place until particles are several tens of nanometers in radius. Simulating this range was not feasible using linear binning, while exponential binning could not solve this either, since the requirement to use an integer growth factor leads to numerically unstable simulations. A technique to simulate the coagulation phase for larger particles will be proposed in section 7.2.

The expected charge of a nanoparticle depends only on the size and the plasma parameters n_e, T_e, n_{i+} and T_i. Charging of nanoparticles due to electron absorption could therefore be taken into account at time-scales at which these relevant plasma parameters did not show significant relative deviations. This was done under the assumption that all nanoparticles carry their expected charge, neglecting the stochastic charging behaviour. It turned out that these relevant plasma parameters were stable up to the simulated $t = 100$ ms so the charging model can be used to simulate coagulation in this way.

Furthermore, we have seen that processes in the nucleation phase take place at the nanosecond time-scale, whilst coagulation takes place at the millisecond time scale. PLASIMO does not currently have an option to simulate various processes at different time-scales. The time range that could be simulated was therefore limited.

Finally, we have shown in section 5.5 that the results of the simulations are nearly independent of the solver tolerance and the initial conditions, which means that the simulations is reliable and robust.

One-dimensional model

Some basic one-dimensional simulations were done which showed that the global model produces realistic results for the relevant plasma parameters and densities. This was done by comparing the density of $C_{12}H_2$ and electrons, as well as some background species such as H_2 and C_4H_2. We have seen that the electron density in the 1D model is significantly lower than what was found in the global model. Since the electron density is an important parameter

for coagulation, it is important to look into this difference. The fact that charged species have a very strong position dependence, which is neglected in the global model, might cause this difference. Negative species have a large density peak in the middle of the plasma, whilst positive species mainly exist near the plasma boundaries. The large spatial dependence of charged particles should preferably be taken into account for the coagulation phase since it produces predominantly negatively charged species.

7.2 Outlook

We have seen that the current model can be used to simulate the nucleation and coagulation phases of dust growth in low pressure RF acetylene plasmas. The volume range that can currently be simulated, however, is more than an order of magnitude too small to simulate the full volume range required, which is up to species with several tens of nanometers in radius. Furthermore, some of the assumptions that were made in the simulation may be relaxed to produce more realistic results. In this section, we will first discuss general extensions and improvements to the model that affect both the nucleation and coagulation phases. We then continue with possible methods of simulating accretion and finally, we propose various extensions to the PLASIMO package required to build these models in the future.

7.2.1 Nucleation phase extensions and improvements

The nucleation model that was used in this thesis relies on many assumptions about the plasma parameters. In this section, we will discuss two assumptions that are not required in principle, and we will discuss how to implement the model without these assumptions. The assumptions that we are going to discuss are that the gas temperature is constant and that vibrational excitations can be neglected.

Constant gas temperature

The assumption that the gas temperature is constant is very common in low-pressure RF plasma models in acetylene. The assumption that $T = 400\,\mathrm{K}$ is the most common in literature [20] [31] [32] [33]. The reaction rate coefficients of ion-molecule and molecule-molecule reactions are in general temperature dependent. Temperature dependent reaction rate coefficients are in general unknown for molecule-molecule reactions, although the temperature dependent reaction rate coefficients are known for the majority of ion-molecule reactions in the model [73] [74] [75]. Instead of fixing the gas temperature, the change of the gas temperature can consequently be calculated from the change in formation enthalpies of the involved species, which are given in appendix B, using conservation of energy [35].

Vibrationally excited states

Vibrational excitations due to electron impact reactions can influence the EEDF, the shape of which is important for the plasma chemistry, since ionisation reaction rates depend on the energy of the electrons. Vibrational excitations of hydrogen gas have been studied extensively for the energy range $0.5\,\mathrm{eV} < E < 10\,\mathrm{eV}$, which is the appropriate energy range for our plasma conditions by Ehrhardt et al. [76]. Furthermore, the vibrational excitations of acetylene have been studied by Tawara et al. [77]. Vibrational excitations of other gas species are not expected to have a significant impact on the plasma since the densities of the other species remain an order of magnitude lower than the densities of acetylene and hydrogen gas as was shown in figure 5.1.

7.2.2 Coagulation

In this thesis, coagulation has been simulated using a discretisation of the volume range in terms of a species set containing integer multiples of an initial coagulation species $C_{12}H_2$. Using 100 species allowed us to model species up to a radius of 1.4 nm, which is insufficient to model the full coagulation phase up to dust particles with a radius of several tens of nanometers in radius. Modelling species up to a radius that is 10 times as large, requires 1000 times more species. Doing this seems computationally unreasonable however, which means that other techniques should be explored. Furthermore, the floating charge of dust particles which is in principle a function of the plasma parameters had to be fixed in advance of the simulation. Simulating coagulation in this way is by definition not self-consistent since the assumption that the electron density is constant cannot be true for the coagulation process which consumes electrons. In this section we will propose solutions in order to be able to model a larger volume

range, as well as how to deal with charging of nanoparticles. Finally, we will present the ingredients required to simulate coagulation in a 1D model.

Simulating a larger volume range

One option is to use larger species as precursor for coagulation. It might for example be possible to combine the chemical reaction rates from appendix A.2 and the coagulation frequency given by equation (2.30) to extend the chemistry to larger species, $C_{24}H_4$ or $C_{48}H_8$ for example, which can consequently be used as the precursor for coagulation instead of $C_{12}H_2$. Although reaction schemes for such large species are as far as we know unknown, Jimenez et al. have measured ions up $C_{24}H_x^y$ which could be used as a starting point to construct the polymerisation reactions for these species [69]. In this way, coagulation can be modelled up to a factor of 2 or 4 times the volume which was reached in this thesis for similar computational cost, which is helpful but still insufficient to model the required volume range.

A second option is to distinguish nucleation and coagulation processes and simulate them using different time scales (Δt in equation (4.2)). The typical time-step that was required in our simulations to model the coagulation phase was $\Delta t \approx 10^{-10}$s, while we have seen that coagulation happens at the millisecond time-scale so that a time step $\Delta t \approx 10^{-6}$s is presumably sufficiently small. The implementation of such a model would mean that a coagulation step has to be taken for every 10,000 nucleation steps, reducing the computational costs significantly. This can be understood from the fact that the number of coagulation reactions scales with the number of coagulation particles squared, if the repulsive force between particles is neglected and all combinations are taken into account. Our model consisted of 100 coagulation species, so the number of coagulation reactions was approximately $\frac{1}{4}(100)^2 = 2500$, where the division by a factor 4 is explained from the degeneracy of reactions ($\frac{1}{2}$) and the requirement that the combination of the species should also be in the set ($\frac{1}{2}$) so $i + j \leq 100$. Since the number of coagulation reactions is more than an order of magnitude larger than the number of nucleation reactions, taking a coagulation step for every 10,000 nucleation steps should significantly speed up the simulation.

Simulating the charging of nanoparticles

In this thesis, charging of nanoparticles was taken into account by specifying the expected charge of nanoparticles as a function the the radius and the plasma parameters n_e, n_i, T_e and T_i which were all assumed to be constant. This assumption has worked out well in this thesis, since charging is not significant for particles up to a radius of 1.4 nm. As larger species get included in the model, a significant number of electrons is lost due to charging which, by itself, changes the floating charges corresponding to the fixed particle sizes. This can be solved by implementing a functionality in PLASIMO that calculates the expected floating charge of a nanoparticle based on the relevant plasma parameters. It will consequently update the electron density based on the electrons consumed by the nanoparticles in order to conserve charge. A follow-up step would subsequently be to calculate the actual charge distribution determined by [67].

Simulating coagulation in 1D

We have seen in section 6 how the nucleation phase can be simulated in one dimension and that there are spatial dependencies in the plasma that cannot simply be neglected as is done by the global model. These dependencies are the largest for charged particles since they can feel the applied RF field. Since the nanoparticles formed by coagulation are in general negatively charged, it makes sense to simulate them taking into account spatial dependencies as well.

As discussed in chapter 4, every species is modelled using its own drift-diffusion equation (equation (2.12)). Fortunately, it is possible to write the momentum balance for dust particles in a similar 'drift-diffusion' like form, which means a term containing the electric field and a term containing the density gradient so that dust particles can be simulated analogously to the drift-diffusion equation of the gas particles. As shown by Akdim et al., this can be done for near steady-state by setting the neutral drag force in equilibrium with all other forces and by defining a momentum loss frequency, a mobility coefficient and a diffusion coefficient [45]. Spatial dependencies can be written in drift-diffusion form for both gas and dust species. Accordingly, we have all the ingredients to build a model of dust growth in plasmas at our disposal.

7.2.3 Accretion

We have seen that the dust growth cycle consists of three distinct phases: nucleation, coagulation and accretion. In this thesis, we have presented techniques to simulate the nucleation and coagulation phases. We have also seen that the expected charge becomes more negative for larger nanoparticles, which preludes the accretion phase. The accretion phase only comes into play if the techniques to model a larger volume range proposed in section 7.2.2 combined with other innovative methods allow for the simulation of species up to several tens of nanometers in radius and beyond.

Prakash et al. have proposed an extension to the general dynamic equation taking into account the physics at the surface of nanoparticles [48]. This is done mathematically using a condensation/ evaporation term which describes the growing and shrinking of nanoparticles due to the condensation and evaporation of monomers on the surface. The ion drag force and gravity also become relevant for dust particles in the hundreds of nanometer range are taken into account by using the drift-diffusion equation for nanoparticles given by Akdim et al. [24] [45] [78].

7.2.4 Recommendations for PLASIMO

In this section we will propose a few additions to PLASIMO in order to improve future dust growth simulations. We will focus on three different aspects: charging, data logging and time scales.

Charging

We have seen in this thesis that the charging of nanoparticles plays an important role in the coagulation phase. We have also seen that it is currently required to establish the charge corresponding to a specific nanoparticle in advance of a simulation, even though this particular charge is a function of the plasma parameters itself. This turned out not to be an issue yet for the simulations in this thesis, since the dust that was grown was insufficient to change the charging parameters n_e, T_e, n_i and T_i significantly, so the initially chosen charges remained valid during the simulations. This however is not true in general, since we have shown that the electron density is expected to decrease during the coagulation phase.

It is by definition impossible to determine the corresponding charges in advance of the simulation self-consistently. The electron density is assumed constant while electrons are being consumed. A self-consistent implementation is to not specify the charges beforehand, but by making this a model parameter instead. At every coagulation time step, the required charges corresponding to the particles present in the model are calculated and updated. Charge conservation is achieved by adjusting the electron density correspondingly.

Data storage

The one-dimensional drift-diffusion module in PLASIMO has a build-in logging setting, which can be used to specify at what moment in time output data should be logged. This is very useful since simulations up to the millisecond or even second range require millions or even billions of iterations. We are generally not interested in nanosecond time resolution after several microsecond have passed, so logging every iteration at a simulation time larger than a few microseconds is a waste of computation time.

Global models do not currently have the option to only write output data at specific times. This was one of the main limitations for running the simulation until longer time-scales, since this required writing multiple (tens) of gigabytes of data, which is hard to process and analyse. The implementation of data-logging settings analogous to what has been implemented in the one-dimensional drift-diffusion model would solve this issue.

Time scales

We have seen in section 5.2 and 5.3.1 that nucleation takes place at the nanosecond time-scale whilst coagulation takes place at the millisecond time-scale. Global model simulations in PLASIMO run currenty according to a single time-scale, which is applied to all processes. This is an unproductive use of computational power, since the slower coagulation processes are simulated using sub-nanosecond time-steps, where microsecond time-steps would suffice. We have already shown in section 7.2.2 that the simulations can be sped up significantly by using two time-scales.

The proposed solution can be applied in PLASIMO by introducing a two-timestep simulation, where fast processes are still simulated according to a maximum stable time-step, while the time-step for the slower coagulation processes is chosen to be larger. This separation of time-scales is easiest applied between the coagulation and nucleation processes in the model, which are currently only connected via $C_{12}H_2$ and electrons. This means that instabilities due to the different time-scales are expected to be inconsequential.

8 Acknowledgements

I would like to thank all the people that have contributed to the project. First of all, I want to thank my supervisors Job Beckers and Tim Donders, for the valuable discussions, support and fun year.

This project would not have been possible without the PLASIMO staff, with special thanks to Jesper Janssen and Jan van Dijk for answering all my PLASIMO related questions and implementing a new feature in PLASIMO for my project.

Ideas tend to arise during coffee breaks, so I would like to thank Ab Schrader, Anne van Gils, Chris Schoutrop, Daan Boer, Guido Klaassen, Jovana Petković, Judith van Huijstee, Lotte van de Rakt, Pieter Sanders, Rick Budé, Saman Hasani, Sim Bouwmans, Tijin Saji and Tim Staps.

I would not have been able to do this project without the love and support of my girlfriend Gabriela, my parents, my brother and my friends Antoine, Emma, Lars and Simone. Thank you so much!

Appendix

A Species and reactions

A.1 Species

Table 1: Species present in the nucleation phase.

Charged species
e^-
$C_2H_2^+$
C_2H^+
C_2^+
C_2H^-
C_4H^-
C_6H^-
C_8H^-
$C_{10}H^-$
$C_{12}H^-$
H_2^+
$C_4H_2^+$
$C_6H_2^+$
$C_6H_4^+$
$C_8H_6^+$
$C_8H_4^+$
$C_{10}H_6^+$
$C_{12}H_6^+$
CH^+
C^+
H^+

Neutral species	Polarisability m^{-3} [20] [79]
C_2H_2	4×10^{-30}
H_2	8×10^{-31}
H	7×10^{-31}
C_2H	4×10^{-30}
C_4H	5×10^{-30}
C_6H	7×10^{-30} est.
C_8H	8×10^{-30} est.
$C_{10}H$	9×10^{-30} est.
$C_{12}H$	1×10^{-29} est.
C_4H_2	7×10^{-30} est.
C_6H_2	1×10^{-29} est.
C_8H_2	1×10^{-29} est.
$C_{10}H_2$	1×10^{-29} est.
$C_{12}H_2$	1×10^{-29} est.
CH	2×10^{-30}
CH_2	2×10^{-30}
C_2H_3	4×10^{-30}
C_4H_3	5×10^{-30}
C_6H_3	6×10^{-30} est
$C_{12}H_6$	1×10^{-29} est.

A.2 reactions

Table 2: Electron impact reactions and the corresponding threshold energy for the reactions used in the plasma chemistry. Estimations using extrapolation and interpolation have been indicated by: 'est'. Table based on [20].

Reaction number	Reaction	Threshold energy (eV)	Reference
1	$C_2H_2 + e^- \rightarrow C_2H_2^+ + 2\,e^-$	11.4	[60]
2	$C_2H_2 + e^- \rightarrow C_2H^+ + H + 2e^-$	16.5	[60]
3	$C_2H_2 + e^- \rightarrow C_2^+ + H_2 + 2e^-$	17.5	[60]
4	$C_2H_2 + e^- \rightarrow CH^+ + CH + 2e^-$	20.6	[60]
5	$C_2H_2 + e^- \rightarrow C^+ + CH_2 + 2e^-$	20.3	[60]
6	$C_2H_2 + e^- \rightarrow H^+ + C_2H + 2e^-$	18.4	[60]
7	$C_2H_2 + e^- \rightarrow C_2H + H + e^-$	7.5	[60]
8	$C_2H_2 + e^- \rightarrow C_2H^- + H$	1.66	[61]
9	$H_2 + e^- \rightarrow H^+ + 2e^-$	15.4	[80]
10	$H_2 + e^- \rightarrow H + H + e^-$	8.9	[81]
11	$C_4H_2 + e^- \rightarrow C_4H + H + e^-$	7.5	[60] est.
12	$C_6H_2 + e^- \rightarrow C_6H + H + e^-$	7.5	[60] est.
13	$C_8H_2 + e^- \rightarrow C_8H + H + e^-$	7.5	[60] est.
14	$C_{10}H_2 + e^- \rightarrow C_{10}H + H + e^-$	7.5	[60] est.
15	$C_{12}H_2 + e^- \rightarrow C_{12}H + H + e^-$	7.5	[60] est.
16	$C_4H_2 + e^- \rightarrow C_4H_2^+ + 2e^-$	11.4	[60] est.
17	$C_6H_2 + e^- \rightarrow C_4H_2^+ + 2e^-$	11.4	[60] est.

Table 3: Ion-molecule reactions and the corresponding rate constant for the reactions used in the plasma chemistry. Table based on [20].

Reaction number	Reaction	Rate constant (m^3s^{-1})	Comment
1	$C_2H^- + C_2H_2 \rightarrow C_4H^- + H_2$	1×10^{-18}	est.
2	$C_4H^- + C_2H_2 \rightarrow C_6H^- + H_2$	1×10^{-18}	est.
3	$C_{2n}H^- + C_2H_2 \rightarrow C_{2n+2}H^- + H_2$	1×10^{-18}	n=3,4,5 est.
4	$H^+ + C_2H_2 \rightarrow C_2H_2^+ + H_2$	5.3×10^{-15}	
5	$C_2H^+ + H_2 \rightarrow C_2H_2^+ + H_2$	1.7×10^{-15}	
6	$C_2H^+ + C_2H_2 \rightarrow C_4H_2^+ + H$	1.2×10^{-15}	
7	$C_2H_2^+ + C_2H_2 \rightarrow C_4H_2^+ + H_2$	1.2×10^{-15}	
8	$C_4H_2^+ + C_2H_2 \rightarrow C_6H_4^+$	1.4×10^{-16}	
9	$C_6H_2^+ + C_2H_2 \rightarrow C_8H_4^+$	1×10^{-17}	
10	$C_6H_4^+ + C_2H_2 \rightarrow C_8H_6^+$	1×10^{-16}	est.
11	$C_8H_4^+ + C_2H_2 \rightarrow C_{10}H_6^+$	1×10^{-16}	est.
12	$C_8H_6^+ + C_2H_2 \rightarrow C_{10}H_6^+ + H_2$	1×10^{-16}	est.
13	$C_{10}H_6^+ + C_2H_2 \rightarrow C_{12}H_6^+ + H_2$	1×10^{-16}	est.
14	$C_{2n}H^- + H_2^+ \rightarrow C_{2n}H + H + H$	1.7×10^{-13}	n=1,2,3,4,5,6 calc.
15	$C_{2n}H^- + C_{2n}H_m^+ \rightarrow C_{2n}H + C_{2n}H_m$	4×10^{-14}	n=1,2,3,4,5,6 calc.

Table 4: Molecule-molecule reactions and the corresponding rate constant for the reactions used in the plasma chemistry. Table based on [20].

Reaction number	Reaction	Rate constant ($m^3 s^{-1}$)	Comment	reference
1	$C_2H + H_2 \rightarrow C_2H_2 + H$	4.9×10^{-19}		[73]
2	$C_2H + H \rightarrow C_2H_2$	4.1×10^{-16}		[74]
3	$C_2H + C_2H_2 \rightarrow C_4H_2 + H$	5.7×10^{-17}		[73]
4	$C_2H + C_4H_2 \rightarrow C_6H_2 + H$	6.6×10^{-17}		[73]
5	$C_2H + C_{2n}H_2 \rightarrow C_{2n+2}H_2 + H$	5.0×10^{-17}	n=3,4,5	[53]
6	$H + C_2H_2 \rightarrow C_2H_3$	3.5×10^{-19}		[75]
7	$H + C_4H_2 \rightarrow C_4H_3$	1.2×10^{-19}		[74]
8	$H + C_6H_2 \rightarrow C_6H_3$	1.6×10^{-18}		[74]
9	$H + C_{2n}H \rightarrow C_{2n}H_2$	4.1×10^{-16}	n=2,3,4,5,6	[74]
10	$C_{2n}H + H_2 \rightarrow C_{2n}H_2 + H$	4.9×10^{-19}	n=2,3,4,5,6	[73]
11	$H + C_2H_3 \rightarrow H_2 + H_2H_2$	6.6×10^{-17}		[75]
12	$H + C_4H_3 \rightarrow H_2 + C_4H_2$	2.4×10^{-17}		[74]
13	$H + C_6H_3 \rightarrow H_2 + C_6H_2$	6.6×10^{-17}	est. reaction 11	[75]
14	$C_4H + C_2H_2 \rightarrow C_6H_2 + H$	6.6×10^{-17}		[73]
15	$C_{2n}H + C_2H_2 \rightarrow C_{2n+2}H_2 + H$	6.6×10^{-17}	est. reaction 14, n=3,4,5	[73]
16	$CH + H_2 \rightarrow CH_2 + H$	1.0×10^{-18}		[74]
17	$CH_2 + H \rightarrow CH + H_2$	2.7×10^{-16}		[75]
18	$CH_2 + CH_2 \rightarrow C_2H_2 + H_2$	5.3×10^{-17}		[74]
19	$C_2H + C_2H_3 \rightarrow C_2H_2 + C_2H_2$	5.0×10^{-17}		[82]
20	$CH_2 + CH \rightarrow C_2H_2 + H$	6.6×10^{-17}		[74]
21	$C_2H_2 + C_2H \rightarrow C_4H_3$	2.2×10^{-18}		[74]
22	$C_4H_2 + C_2H \rightarrow C_6H_3$	2.2×10^{-18}	est. reaction 21	[74]
23	$C_2H_3 + CH \rightarrow C_2H_2 + CH_2$	8.3×10^{-17}		[82]
24	$C_4H_3 + H \rightarrow C_2H_2 + C_2H_2$	1.1×10^{-16}		[74]
25	$C_6H_3 + H \rightarrow C_4H_2 + C_2H_2$	8.1×10^{-17}		[74]

B Heat of formation

Table 5: Heat of formation for gas species [83] [84]. Estimations using extrapolation or interpolation have been indicated by 'est'.

Species	Formation heat (eV)
C_2H_2	0
H_2	0
H	2.3
C_2H	5.9
C_4H	8.1
C_6H	10.3
C_8H	12.7
$C_{10}H$	14.9
$C_{12}H$	17.2
C_4H_2	4.8
C_6H_2	7.2
C_8H_2	9.3
$C_{10}H_2$	11.5
$C_{12}H_2$	13.8
CH	6.2
CH_2	4.1
C_2H_3	3.1
C_4H_3	5.7 est.
C_6H_3	7.5
$C_{12}H_6$	5.7 est.

Species	Formation heat (eV)
$C_2H_2^+$	13.8
C_2H^+	12
C_2^+	20.5
C_2H^-	2.9
C_4H^-	5 est.
C_6H^-	7 est.
C_8H^-	9 est.
$C_{10}H^-$	11 est.
$C_{12}H^-$	13 est.
H_2^+	15.4
$C_4H_2^+$	15.0
$C_6H_2^+$	17 est.
$C_6H_4^+$	14.6
$C_8H_6^+$	16.6 est.
$C_8H_4^+$	16.6 est.
$C_{10}H_6^+$	18.6 est.
$C_{12}H_6^+$	20.6 est.
CH^+	16.9
C^+	18.8
H_2^+	15.5
H^+	15.9

C Sticking coefficients

Table 6: Sticking coefficients for radicals.

Species	Sticking coefficient [20]
C_2H_3, C_4H_3, C_6H_3	0.35 [85]
CH, CH_2	0.025 [86]
C_2H, C_4H, C_6H, C_8H, $C_{10}H$, $C_{12}H$	0.9 [85]

D Plots of plasma chemistry

D.1 nucleation and coagulation without charging

Figure D.1: Key outputs of the global model of the plasma chemistry. (a) Shows the electron temperature, (b) the densities of some gas species, (c) shows the densities of some negative ions and (d) shows the densities of some radicals as a function of time.

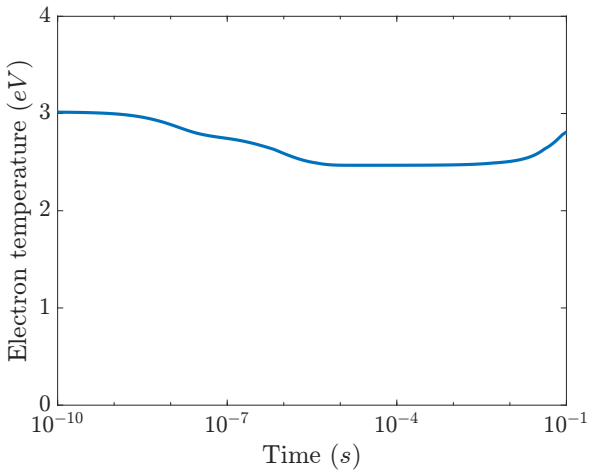

Figure D.2: Electron temperature as a function of time.

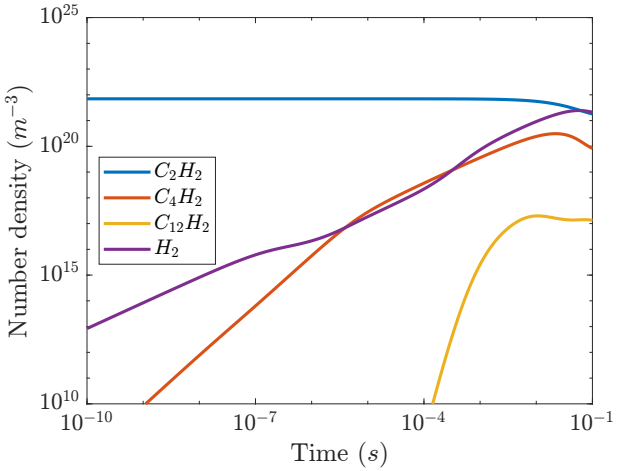

Figure D.3: Particle densities for gas species as a function of time.

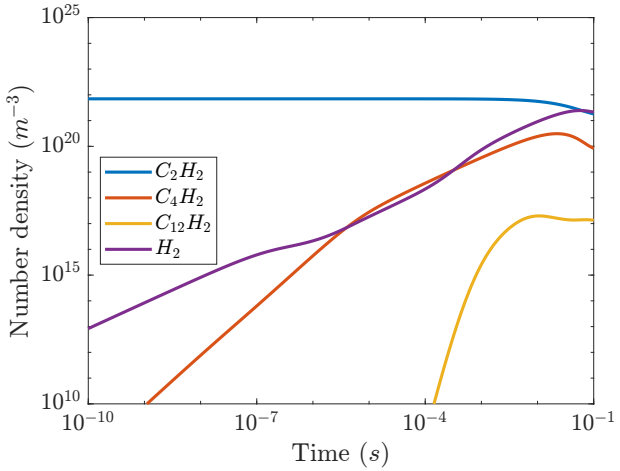

Figure D.4: Particle densities for negative ions as a function of time.

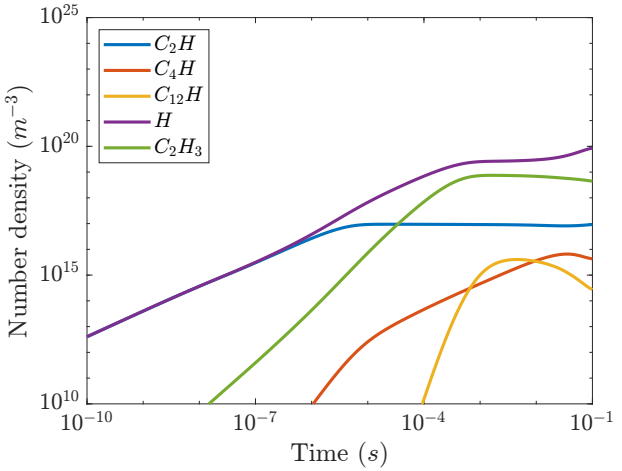

Figure D.5: Particle densities for radicals as a function of time.

E Matlab scripts

E.1 Create reaction list

```
%% Set up parameters
fileID = fopen('Reaction_list','wt');
factor = 2;
nr_linear_species = 10;%Choose desired number
nr_factor_species = 0;%Choose desired number
radius1 = 0.3e-9;
Volume1 = 4/3*pi*radius1^3;
V_multiples = [(1:nr_linear_species) (nr_linear_species)*factor.^(1:nr_factor_species)];
V = (Volume1 .* V_multiples);
r_multiples = V_multiples.^(1/3);
charge = round(r_multiples);
sections = size(V,2);
chi = zeros(sections,sections,sections);
Beta = zeros(sections);
kB = 1.38e-23;
rho = 2000;
Tgas = 400;
Beta_constant = (3/(4*pi))^(1/6)*(6*kB*Tgas/rho)^(1/2);
Carbon = 12 .* V_multiples;
Hydrogen = 2 .* V_multiples;
Particles = strings(sections,1);
for i = 1 : sections
    Particle_name = ['C',num2str(Carbon(i)),'H',num2str(Hydrogen(i))];
    Particles(i) = Particle_name;
end
threshold = 0.001;

%% Build chi and Beta matrices
for i = 1:sections
    for j = 1:sections
        for k = 1:sections
            if k~=1 && k~=sections
                if V(k) <= V(i) + V(j) && V(i)+V(j) <= V(k+1)
                    chi(i,j,k) = vpa((V(k+1) - (V(i)+V(j))))/vpa((V(k+1)-V(k)));
                elseif V(k-1) <= V(i) + V(j) && V(i) + V(j) <= V(k)
                    chi(i,j,k) = vpa((V(i)+V(j) - V(k-1)))/vpa((V(k)-V(k-1)));
                end
            end
            if k == 1
                if V(k) <= V(i) + V(j) && V(i)+V(j) <= V(k+1)
                    chi(i,j,k) = (V(k+1) - (V(i)+V(j)))/(V(k+1)-V(k));
                elseif V(i) + V(j) <= V(k)
                    chi(i,j,k) = (V(i)+V(j))/(V(k));
                end
            end
            if k == sections
                Vextra = V(k)*factor;
                if V(k) <= V(i) + V(j) && V(i)+V(j) <= Vextra
                    chi(i,j,k) = (Vextra - (V(i)+V(j)))/(Vextra-V(k));
                elseif V(k-1) <= V(i) + V(j) && V(i) + V(j) <= V(k)
                    chi(i,j,k) = (V(i)+V(j) - V(k-1))/(V(k)-V(k-1));
                end
            end
        end
    end
end

for i = 1:sections
    for j = 1 : sections
        Beta(i,j) = Beta_constant*(1/V(i)+1/V(j))^(1/2)*(V(i)^(1/3)+V(j)^(1/3))^2;
    end
end

%% Build specieslist
for i = 1 : sections
    fprintf(fileID,'Species{\n');
    fprintf(fileID,'\tState{\n');
    fprintf(fileID,'\t\tType \t Atom\n');
    fprintf(fileID,strcat('\t\tName \t', Particles(i), '\n'));
    fprintf(fileID,strcat('\t\tTexName \t', Particles(i), '\n'));
    fprintf(fileID,'\t\tWeight \t 1\n');
    fprintf(fileID,'\t\tEnergy \t 1*eV\n');
    fprintf(fileID,'\t}\n');
    fprintf(fileID,strcat('\tName \t', Particles(i), '\n'));
    fprintf(fileID,'\tRadius \t 1*Ang \n');
    fprintf(fileID,'}\n');
end

%% Build initial values
    fprintf(fileID,'InitialValues{\n');
    fprintf(fileID,'\tDensities{\n');
    fprintf(fileID,strcat('\t\tSpecies\t',Particles(1),'\t1e18*m^-3\n'));
for i = 2 : sections
    fprintf(fileID,strcat('\t\tSpecies\t',Particles(i),'\t0*m^-3\n'));
end
    fprintf(fileID,'\t}\n');
    fprintf(fileID,'\tType\tValues\n');
    fprintf(fileID,'}\n');

%% Build reactions for ExtraSourceList
Reaction = strings(10,1);
a = 1;
for i = 1 : sections
    for j = 1 : sections-i %delete -i if exponential binning
        for k = 1 : sections
```

```
96              if not(chi(i,j,k) > 0-threshold && chi(i,j,k) < 0+threshold) && j >= i
97                  if chi(i,j,k) > 1-threshold && chi(i,j,k) < 1+threshold
98                      if charge(i)+charge(j)==charge(k)
99                          Message = ['\tName reaction',num2str(i),'_',num2str(j),'_',num2str(k),'\n'];
100                         Reaction(a) = Message;
101                         fprintf(fileID,'Process{\n');
102                         fprintf(fileID,'\tRateCoefficient{\n');
103                         fprintf(fileID,'\t\tType Custom\n');
104                         fprintf(fileID,strcat('\t\tFunction \t',num2str(Beta(i,j)),'*m^3/s\n\t}\n'));
105                         fprintf(fileID,Message);
106                         fprintf(fileID,strcat('\tFormat\t ','"',Particles(i), '\t+\t', Particles(j),'\t -> \t',Particles(k
                                ),'"','\n'));
107     %                     fprintf(fileID,'\t_EnergyEH\t0*ev \n');
108     %                     fprintf(fileID,'\tApplyDB no\n');
109                         fprintf(fileID,'}\n');
110                         a = a + 1;
111                     elseif charge(i) + charge(j) > charge(k)
112                         new_electrons = charge(i) + charge(j) - charge(k);
113                         add_electrons = "";
114                         for l = 1 : new_electrons
115                             add_electrons =  add_electrons + " + e";
116                         end
117                         Message = ['\tName reaction',num2str(i),'_',num2str(j),'_',num2str(k),'\n'];
118                         Reaction(a) = Message;
119                         fprintf(fileID,'Process{\n');
120                         fprintf(fileID,'\tRateCoefficient{\n');
121                         fprintf(fileID,'\t\tType Custom\n');
122                         fprintf(fileID,strcat('\t\tFunction \t',num2str(Beta(i,j)),'*m^3/s\n\t}\n'));
123                         fprintf(fileID,Message);
124                         fprintf(fileID,strcat('\tFormat\t ','"',Particles(i), '\t+\t', Particles(j),'\t -> \t',Particles(k
                                ),add_electrons,'" \n' ));
125     %                     fprintf(fileID,'\t_EnergyEH\t0*ev \n');
126     %                     fprintf(fileID,'\tApplyDB no\n');
127                         fprintf(fileID,'}\n');
128                         a = a + 1;
129                     else
130                         loss_electrons = charge(k) - charge(i) - charge(j);
131                         subtract_electrons = "";
132                         for l = 1 : loss_electrons
133                             subtract_electrons =  subtract_electrons + " + e";
134                         end
135                         Message = ['\tName reaction',num2str(i),'_',num2str(j),'_',num2str(k),'\n'];
136                         Reaction(a) = Message;
137                         fprintf(fileID,'Process{\n');
138                         fprintf(fileID,'\tRateCoefficient{\n');
139                         fprintf(fileID,'\t\tType Custom\n');
140                         fprintf(fileID,strcat('\t\tFunction \t',num2str(Beta(i,j)),'*m^3/s\n\t}\n'));
141                         fprintf(fileID,Message);
142                         fprintf(fileID,strcat('\tFormat\t ','"',Particles(i), '\t+\t', Particles(j),subtract_electrons,'\t
                                -> \t',Particles(k),'" \n' ));
143                         fprintf(fileID,strcat('\tRateLHS\t ','"',Particles(i), '\t+\t', Particles(j), '" \n' ));
144     %                     fprintf(fileID,'\t_EnergyEH\t0*ev \n');
145     %                     fprintf(fileID,'\tApplyDB no\n');
146                         fprintf(fileID,'}\n');
147                         a = a + 1;
148                     end
149                 else
150                     q = char(39);
151 %                   [nom,denom] = numden(sym(chi(i,j,k)*2));
152                     [nom,denom] = rat(chi(i,j,k));
153                     nom = double(nom);
154                     denom = double(denom);
155                     Message = ['\tName reaction',num2str(i),'_',num2str(j),'_',num2str(k),'\n'];
156                     Reaction(a) = Message;
157                     fprintf(fileID,'Process{\n');
158                     fprintf(fileID,'\tRateCoefficient{\n');
159                     fprintf(fileID,'\t\tType Custom\n');
160                     if denom == 1 && nom == 1
161                         fprintf(fileID,strcat('\t\tFunction \t',num2str(Beta(i,j)),'*m^3/s\n\t}\n'));
162                     else
163                         fprintf(fileID,strcat('\t\tFunction \t',num2str(Beta(i,j)/denom),'*m^3/s\n\t}\n'));
164                     end
165                     fprintf(fileID,Message);
166                     fprintf(fileID,strcat('\tFormat\t ','"',num2str(denom/2)," ",Particles(i), '\t+\t',num2str(denom/2),"
                            ", Particles(j),'\t -> \t',num2str(nom)," ",Particles(k),'"','\n'));
167                     fprintf(fileID,strcat('\tRateLHS "1"," ",Particles(i),' + 1'," ",Particles(j),'"\n'));
168
169 % % % %                       fprintf(fileID,'\t_EnergyEH\t0*ev \n');
170 % % % %                       fprintf(fileID,'\tApplyDB no\n');
171                     fprintf(fileID,'}\n');
172                     a = a + 1;
173                 end
174             end
175         end
176     end
177 end
```

References

[1] A. Melzer *et al.*, *Physics of dusty plasmas*. Springer, 2019.

[2] D. A. Gurnett and A. Bhattacharjee, *Introduction to plasma physics: with space and laboratory applications*. Cambridge university press, 2005.

[3] M. A. Lieberman and A. J. Lichtenberg, *Principles of Plasma Discharges and Material Processing*. Wiley, 2005.

[4] W. Crookes, "On radiant matter a lecture delivered to the british association for the advancement of science, at sheffield," *Friday, August*, vol. 22, p. 1879, 1879.

[5] I. Langmuir, "Oscillations in ionized gases," *Proceedings of the National Academy of Sciences*, vol. 14, no. 8, pp. 627–637, 1928.

[6] A. Egeland and A. Brekke, "The northern light: From mystery to modern space science," *Endeavour*, vol. 8, no. 4, pp. 188–193, 1984.

[7] C. G. Lee, K. J. Kanarik, and R. A. Gottscho, "The grand challenges of plasma etching: a manufacturing perspective," *Journal of Physics D: Applied Physics*, vol. 47, no. 27, p. 273001, 2014.

[8] G. D. Holman, "Scientific considerations for future spectroscopic measurements from space of activity on the sun," *Journal of Geophysical Research: Space Physics*, vol. 121, no. 12, pp. 11–667, 2016.

[9] S. Nijdam, J. Teunissen, and U. Ebert, "The physics of streamer discharge phenomena," *Plasma Sources Science and Technology*, vol. 29, no. 10, p. 103001, 2020.

[10] H. Cheng, X. Liu, X. Lu, and D. Liu, "Numerical study on propagation mechanism and bio-medicine applications of plasma jet," *High Voltage*, vol. 1, no. 2, pp. 62–73, 2016.

[11] K. Yi, D. Liu, X. Chen, J. Yang, D. Wei, Y. Liu, and D. Wei, "Plasma-enhanced chemical vapor deposition of two-dimensional materials for applications," *Accounts of Chemical Research*, vol. 54, no. 4, pp. 1011–1022, 2021.

[12] S. Panneerselvam and S. Choi, "Nanoinformatics: emerging databases and available tools," *International journal of molecular sciences*, vol. 15, no. 5, pp. 7158–7182, 2014.

[13] M. Bloemen, "Immunomagnetic separation of bacteria by iron oxide nanoparticles," 2015.

[14] D. Taylor, "Silica exposure health effects & risks," Aug 2017.

[15] G. S. Selwyn, "Optical characterization of particle traps," *Plasma Sources Science and Technology*, vol. 3, no. 3, p. 340, 1994.

[16] M. van de Kerkhof, E. Galutschek, A. Yakunin, S. Cats, and C. Cloin, "Particulate and molecular contamination control in euv-induced h2-plasma in euv lithographic scanner," in *Systems Contamination: Prediction, Control, and Performance 2020*, vol. 11489, pp. 79–95, SPIE, 2020.

[17] M. A. van de Kerkhof, "Euv-induced plasma, electrostatics and particle contamination control," 2021.

[18] A. Fridman, L. Boufendi, T. Hbid, B. Potapkin, and A. Bouchoule, "Dusty plasma formation: Physics and critical phenomena. theoretical approach," *Journal of Applied Physics*, vol. 79, no. 3, pp. 1303–1314, 1996.

[19] C. Deschenaux, A. Affolter, D. Magni, C. Hollenstein, and P. Fayet, "Investigations of ch4, c2h2 and c2h4 dusty rf plasmas by means of ftir absorption spectroscopy and mass spectrometry," *Journal of Physics D: Applied Physics*, vol. 32, no. 15, p. 1876, 1999.

[20] K. De Bleecker, A. Bogaerts, and W. Goedheer, "Detailed modeling of hydrocarbon nanoparticle nucleation in acetylene discharges," *Physical Review E*, vol. 73, no. 2, p. 026405, 2006.

[21] J. Benedikt, A. Consoli, M. Schulze, and A. Von Keudell, "Time-resolved molecular beam mass spectrometry of the initial stage of particle formation in an ar/he/c2h2 plasma," *The Journal of Physical Chemistry A*, vol. 111, no. 42, pp. 10453–10459, 2007.

[22] F. Van De Wetering, J. Beckers, and G. Kroesen, "Anion dynamics in the first 10 milliseconds of an argon–acetylene radio-frequency plasma," *Journal of Physics D: Applied Physics*, vol. 45, no. 48, p. 485205, 2012.

[23] L. Boufendi and A. Bouchoule, "Industrial developments of scientific insights in dusty plasmas," *Plasma Sources Science and Technology*, vol. 11, no. 3A, p. A211, 2002.

[24] F. Van de Wetering, R. Brooimans, S. Nijdam, J. Beckers, and G. Kroesen, "Fast and interrupted expansion in cyclic void growth in dusty plasma," *Journal of Physics D: Applied Physics*, vol. 48, no. 3, p. 035204, 2015.

[25] K. De Bleecker, A. Bogaerts, and W. Goedheer, "Modelling of nanoparticle coagulation and transport dynamics in dusty silane discharges," *New Journal of Physics*, vol. 8, no. 9, p. 178, 2006.

[26] D. J. Griffiths, "Introduction to electrodynamics," 2005.

[27] R. D. White, R. Robson, S. Dujko, P. Nicoletopoulos, and B. Li, "Recent advances in the application of boltzmann equation and fluid equation methods to charged particle transport in non-equilibrium plasmas," *Journal of Physics D: Applied Physics*, vol. 42, no. 19, p. 194001, 2009.

[28] B. Cappella and G. Dietler, "Force-distance curves by atomic force microscopy," *Surface science reports*, vol. 34, no. 1-3, pp. 1–104, 1999.

[29] G. Hagelaar and L. C. Pitchford, "Solving the boltzmann equation to obtain electron transport coefficients and rate coefficients for fluid models," *Plasma Sources Science and Technology*, vol. 14, no. 4, p. 722, 2005.

[30] L. Huxley and R. Crompton, "The drift and diffusion of electrons in gases," 1974.

[31] X.-M. Liu, Q.-N. Li, and X. Xu, "Simulation of nanoparticle coagulation in radio-frequency capacitively coupled c2h2 discharges," *Chinese Physics B*, vol. 23, no. 8, p. 085202, 2014.

[32] A. Akhoundi and G. Foroutan, "The effects of gas dilution on the nanoparticles nucleation in a low pressure capacitively coupled acetylene discharge," *Physics of Plasmas*, vol. 24, no. 5, p. 053516, 2017.

[33] M. Jiménez-Redondo, I. Tanarro, R. J. Peláez, L. Díaz-Pérez, and V. J. Herrero, "Ionic polymerization in cold plasmas of acetylene with ar and he," *The Journal of Physical Chemistry A*, vol. 123, no. 38, pp. 8135–8147, 2019.

[34] J.-L. Raimbault and P. Chabert, "Edge-to-center plasma density ratio in high density plasma sources," *Plasma Sources Science and Technology*, vol. 18, no. 1, p. 014017, 2008.

[35] A. Hurlbatt, A. R. Gibson, S. Schröter, J. Bredin, A. P. S. Foote, P. Grondein, D. O'Connell, and T. Gans, "Concepts, capabilities, and limitations of global models: a review," *Plasma Processes and Polymers*, vol. 14, no. 1-2, p. 1600138, 2017.

[36] H. Ellis, R. Pai, E. McDaniel, E. Mason, and L. Viehland, "Transport properties of gaseous ions over a wide energy range," *Atomic Data and Nuclear Data Tables*, vol. 17, no. 3, pp. 177–210, 1976.

[37] J. F. J. Janssen, *Equilibrium and transport in molecular plasmas*. PhD thesis, 2016.

[38] A. Laricchiuta, G. Colonna, D. Bruno, R. Celiberto, C. Gorse, F. Pirani, and M. Capitelli, "Classical transport collision integrals for a lennard-jones like phenomenological model potential," *Chemical Physics Letters*, vol. 445, no. 4-6, pp. 133–139, 2007.

[39] G. Franz, *Low pressure plasmas and microstructuring technology*. Springer Science & Business Media, 2009.

[40] E. W. McDaniel and E. A. Mason, "Mobility and diffusion of ions in gases," 1973.

[41] S. Ashida, C. Lee, and M. Lieberman, "Spatially averaged (global) model of time modulated high density argon plasmas," *Journal of Vacuum Science & Technology A: Vacuum, Surfaces, and Films*, vol. 13, no. 5, pp. 2498–2507, 1995.

[42] T. Donders, T. Staps, and J. Beckers, "Characterization of cyclic dust growth in a low-pressure, radio-frequency driven argon-hexamethyldisiloxane plasma," *Journal of Physics D: Applied Physics*, vol. 55, no. 39, p. 395203, 2022.

[43] K. Ostrikov, "Colloquium: Reactive plasmas as a versatile nanofabrication tool," *Reviews of modern physics*, vol. 77, no. 2, p. 489, 2005.

[44] C. Hollenstein, A. Howling, C. Courteille, D. Magni, S. Scholz, G. Kroesen, N. Simons, W. De Zeeuw, and W. Schwarzenbach, "Silicon oxide particle formation in rf plasmas investigated by infrared absorption spectroscopy and mass spectrometry," *Journal of Physics D: Applied Physics*, vol. 31, no. 1, p. 74, 1998.

[45] M. Akdim and W. Goedheer, "Modeling of dust in a silane/hydrogen plasma," *Journal of applied physics*, vol. 94, no. 1, pp. 104–109, 2003.

[46] H. M. Mott-Smith and I. Langmuir, "The theory of collectors in gaseous discharges," *Physical review*, vol. 28, no. 4, p. 727, 1926.

[47] S. K. Friedlander *et al.*, *Smoke, dust, and haze*, vol. 198. Oxford university press New York, 2000.

[48] A. Prakash, A. Bapat, and M. Zachariah, "A simple numerical algorithm and software for solution of nucleation, surface growth, and coagulation problems," *Aerosol Science & Technology*, vol. 37, no. 11, pp. 892–898, 2003.

[49] P. Agarwal and S. L. Girshick, "Sectional modeling of nanoparticle size and charge distributions in dusty plasmas," *Plasma Sources Science and Technology*, vol. 21, no. 5, p. 055023, 2012.

[50] S. Hong, J. Berndt, and J. Winter, "Growth precursors and dynamics of dust particle formation in the ar/ch4 and ar/c2h2 plasmas," *Plasma Sources Science and Technology*, vol. 12, no. 1, p. 46, 2002.

[51] M. Mao, J. Benedikt, A. Consoli, and A. Bogaerts, "New pathways for nanoparticle formation in acetylene dusty plasmas: a modelling investigation and comparison with experiments," *Journal of Physics D: Applied Physics*, vol. 41, no. 22, p. 225201, 2008.

[52] I. Denysenko, E. von Wahl, S. Labidi, M. Mikikian, H. Kersten, T. Gibert, E. Kovačević, and N. Azarenkov, "Modeling of argon–acetylene dusty plasma," *Plasma Physics and Controlled Fusion*, vol. 61, no. 1, p. 014014, 2018.

[53] J. R. Doyle, "Chemical kinetics in low pressure acetylene radio frequency glow discharges," *Journal of applied physics*, vol. 82, no. 10, pp. 4763–4771, 1997.

[54] S. Stoykov, C. Eggs, and U. Kortshagen, "Plasma chemistry and growth of nanosized particles in a c2h2 rf discharge," *Journal of Physics D: Applied Physics*, vol. 34, no. 14, p. 2160, 2001.

[55] M. Vasile and G. Smolinsky, "The chemistry of radiofrequency discharges: Acetylene and mixtures of acetylene with helium, argon and xenon," *International Journal of Mass Spectrometry and Ion Physics*, vol. 24, no. 1, pp. 11–23, 1977.

[56] D. Herrebout, A. Bogaerts, R. Gijbels, W. J. Goedheer, and A. Vanhulsel, "A one-dimensional fluid model for an acetylene rf discharge: A study of the plasma chemistry," *IEEE transactions on plasma science*, vol. 31, no. 4, pp. 659–664, 2003.

[57] K. De Bleecker, A. Bogaerts, and W. Goedheer, "Aromatic ring generation as a dust precursor in acetylene discharges," *Applied physics letters*, vol. 88, no. 15, p. 151501, 2006.

[58] A. Burcat and B. Ruscic, "Third millenium ideal gas and condensed phase thermochemical database for combustion (with update from active thermochemical tables).," tech. rep., Argonne National Lab.(ANL), Argonne, IL (United States), 2005.

[59] A. Burcat and B. Ruscic, *Third millennium ideal gas and condensed phase thermochemical database for combustion.* Technion-Israel Institute of Technology Haifa, Israel, 2001.

[60] R. Janev and D. Reiter, "Collision processes of c 2, 3 h y and c 2, 3 h y+ hydrocarbons with electrons and protons," *Physics of Plasmas*, vol. 11, no. 2, pp. 780–829, 2004.

[61] J. Rutkowsky, H. Drost, and H. Spangenberg, "Investigation of the inelastic interaction of slow monoenergetic electrons with simple hydrocarbon molecules. 1," *Annalen der Physik (Leipzig)*, vol. 37, no. 4, pp. 259–270, 1980.

[62] W. Graef, "Zero-dimensional models for plasma chemistry," 2012.

[63] E. Carbone, W. Graef, G. Hagelaar, D. Boer, M. M. Hopkins, J. C. Stephens, B. T. Yee, S. Pancheshnyi, J. van Dijk, and L. Pitchford, "Data needs for modeling low-temperature non-equilibrium plasmas: the lxcat project, history, perspectives and a tutorial," *Atoms*, vol. 9, no. 1, p. 16, 2021.

[64] S. Warthesen and S. Girshick, "Numerical simulation of the spatiotemporal evolution of a nanoparticle–plasma system," *Plasma Chemistry and Plasma Processing*, vol. 27, no. 3, pp. 292–310, 2007.

[65] W. M. Haynes, D. R. Lide, and T. J. Bruno, *CRC handbook of chemistry and physics*. CRC press, 2016.

[66] B. Santos and F. Vidal, "Influence of multipolar electrostatic and van der waals forces on the coagulation of silicon nanoparticles in low-temperature argon-silane plasmas," *Plasma Sources Science and Technology*, vol. 29, no. 11, p. 115004, 2020.

[67] T. Matsoukas and M. Russell, "Particle charging in low-pressure plasmas," *Journal of Applied Physics*, vol. 77, no. 9, pp. 4285–4292, 1995.

[68] D. Kahaner, E. Ng, W. Schiesser, and S. Thompson, "Experiments with an ordinary differential equation solver in the parallel solution of method of lines problems on a shared-memory parallel computer," *Journal of Computational and Applied Mathematics*, vol. 38, no. 1-3, pp. 231–253, 1991.

[69] M. Jiménez-Redondo, I. Tanarro, and V. J. Herrero, "Time evolution of neutral and charged species in ar/c2h2 capacitively-coupled rf discharges," *Plasma Sources Science and Technology*, vol. 31, no. 6, p. 065003, 2022.

[70] C. Opal, W. Peterson, and E. Beaty, "Measurements of secondary-electron spectra produced by electron impact ionization of a number of simple gases," *The Journal of Chemical Physics*, vol. 55, no. 8, pp. 4100–4106, 1971.

[71] J. Benedikt, "Plasma-chemical reactions: low pressure acetylene plasmas," *Journal of Physics D: Applied Physics*, vol. 43, no. 4, p. 043001, 2010.

[72] J. Knight, C. Freeman, M. McEwan, V. Anicich, and W. Huntress, "A flow tube study of ion-molecule reactions of acetylene," *Journal of Physical Chemistry*, vol. 91, no. 14, pp. 3898–3902, 1987.

[73] M. Frenklach and J. Warnatz, "Detailed modeling of pah profiles in a sooting low-pressure acetylene flame," *Combustion science and technology*, vol. 51, no. 4-6, pp. 265–283, 1987.

[74] H. Wang and M. Frenklach, "A detailed kinetic modeling study of aromatics formation in laminar premixed acetylene and ethylene flames," *Combustion and flame*, vol. 110, no. 1-2, pp. 173–221, 1997.

[75] M. Masi, C. Cavallotti, and S. Carra, "Different approaches for methane plasmas modeling," *Chemical engineering science*, vol. 53, no. 22, pp. 3875–3886, 1998.

[76] H. Ehrhardt, L. Langhans, F. Linder, and H. Taylor, "Resonance scattering of slow electrons from h *sub*2 and co: Angular distributions.," tech. rep., Univ., Freiburg i. B., 1968.

[77] H. Tawara, "Cross sections and related data for electron collisions with hydrogen molecules and molecular ions," *Journal of Physical and Chemical Reference Data*, 1990.

[78] M. S. Barnes, J. H. Keller, J. C. Forster, J. A. O'Neill, and D. K. Coultas, "Transport of dust particles in glow-discharge plasmas," *Physical review letters*, vol. 68, no. 3, p. 313, 1992.

[79] National institute of standards and technology, "Computation chemistry comparison benchmark database." `https://cccbdb.nist.gov/introx.asp`, 2022. Accessed: 2022-09-20.

[80] H. Tawara and T. Kato, "Total and partial ionization cross sections of atoms and ions by electron impact," *Atomic Data and Nuclear Data Tables*, vol. 36, no. 2, pp. 167–353, 1987.

[81] A. Engelhardt and A. Phelps, "Elastic and inelastic collision cross sections in hydrogen and deuterium from transport coefficients," *Physical Review*, vol. 131, no. 5, p. 2115, 1963.

[82] J. A. Miller and C. T. Bowman, "Mechanism and modeling of nitrogen chemistry in combustion," *Progress in energy and combustion science*, vol. 15, no. 4, pp. 287–338, 1989.

[83] R. K. Janev and D. Reiter, *Collision processes of hydrocarbon species in hydrogen plasmas: II. The ethane and propane families*. Forschungszentrum, Zentralbibliothek, 2002.

[84] "Prof. burcat's thermodynamic data."

[85] A. Von Keudell, C. Hopf, T. Schwarz-Selinger, and W. Jacob, "Surface loss probabilities of hydrocarbon radicals on amorphous hydrogenated carbon film surfaces: Consequences for the formation of re-deposited layers in fusion experiments," *Nuclear Fusion*, vol. 39, no. 10, p. 1451, 1999.

[86] H. Kojima, H. Toyoda, and H. Sugai, "Observation of ch2 radical and comparison with ch3 radical in a rf methane discharge," *Applied physics letters*, vol. 55, no. 13, pp. 1292–1294, 1989.